TEMPERATURE DISTRIBUTION IN AN IMPINGING GAS JET FROM INTERFEROMETRIC MEASUREMENTS

by

Amanda L. Dowd

(A Thesis submitted for the degree of Ph.D.)

Department of Engineering,
University of Leicester.

July 1981

TEMPERATURE DISTRIBUTION IN AN IMPINGING GAS JET FROM INTERFEROMETRIC MEASUREMENTS

by Amanda L. Dowd

Abstract

A hot gas jet was produced by an Argon plasma torch and was played on a water cooled rotating cylinder mounted 30 mm above the nozzle of the torch. The power and gas flow rate to the torch were varied. A Mach-Zehnder interferometer was used to form the interference fringe shift patterns. A version of the Abel Transformation was used to derive radial temperature distribution results from collimated measurements of fringe shift along parallel chords at points along the axis of the jet.

The axial temperatures of the jet were found to be between 800 K and 8000 K. No results were possible in the area of the jet close to the cool surface due to turbulence in the fringe pattern. Relationships between input conditions to the torch and the temperatures in the jet were sought but no conclusions could be drawn due to the severe limitations found in the analysis.

In the range of power, 1.3 to 3 kW, and flow rate, 1.4 to 4.3 l/min, supplied to the torch, the number of fringe shifts observed in the interferograms was small, usually less than 2.5, making the fitting of fringe shift curves to the experimental data points uncertain. Tests undertaken fitting different shaped curves to a sample set of data caused 50 - 100% variations in the resulting radial temperature distribution.

Slight variations in the radius of the jet measured from the interferograms caused large changes in on-axis temperature, though the distribution towards the outer edge of the jet was unaffected. A similar phenomenon was observed by changing the number of iteration points used in the numerical analysis.

Areas for further work are identified and discussed in the thesis.

ACKNOWLEDGEMENTS

The author wishes to dedicate this work to the late Dr. R.W. Maxwell, in grateful thanks for the help and encouragement he offered as a Supervisor during the course of this work.

She would also like to extend her thanks to Dr. G.L. Booth for his valuable advice during the preparation of this thesis, and to other members of the Leicester University Engineering Department.

Thanks also go to Jane Waterfield for typing this thesis and husband Chris Dowd for his support throughout.

TEMPERATURE DISTRIBUTION IN AN IMPINGING GAS JET FROM INTERFEROMETRIC MEASUREMENTS

TABLE OF CONTENTS Page No.

Page No.

LIST OF FIGURES

CHAPTER I INTRODUCTION

1.1 FIELD OF INTEREST

At the time this work was started there was an interest in the Department in high temperature transfer processes. The aim was an elucidation of the heat and mass transfer processes taking place when a hot gas jet, with a source temperature of greater than 15000 K impinges on a cold surface.

Such gas jets can be obtained using a torch of the Gerdien type, described in more detail in a later chapter. The gas of interest flows through an electric arc enclosed within the torch, is heated thereby to a high temperature and then issues into the atmosphere through an orifice. Dependent on the gas flow rate and the electrical input to the torch, a wide range of gas temperatures can be obtained up to 20000 K (1). At a sufficiently high temperature the gas dissociates and becomes ionised, and is usually referred to as a plasma. For argon, the gas studied in this work, there is no appreciable self ionisation below 8000 K, as shown in Fig. 2, calculated using Saha's equation, in Appendix AIII.

Work so far in the Department has measured properties of free and impinging plasma jets, such as Transport Properties in High Temperature Gases by D Dobbs (2) and Temperature Measurements in an Argon Plasma Jet by Ruddy (3); part of a programme to develop measurement techniques of those properties of the jet which can be compared with parallel theoretical studies of jet behaviour. Both works placed emphasis on jets with substantial ionisation. In the work reported here attention has shifted to study the lower temperature jets where there is no ionisation, in the region 1000 K to 8000 K.

Of obvious interest is the temperature distribution within the jet when it impinges on a cooled surface. If temperature profiles close to the surface can be determined, then, used in conjunction with thermal conductivity data, local heat transfer coefficients can be obtained. Similarly, radial temperature across the jet away from the surface, and hence axial temperature along the jet can lead to information regarding heat and mass transfers between the jet and its surrounding air.

1.2 METHODS OF MEASURING TEMPERATURES IN HOT GAS JETS

For measurement of gas temperatures the use of thermocouples immediately springs to mind. There are, however, two major disadvantages:

(a) Most normal thermocouple pairs rapidly melt at the temperatures involved.

(b) Insertion of thermocouple wires into the jet disturbs the jet and affects the flow distribution.

Of non intrusive techniques optical methods, in particular interferometry, are possible (4,5,6). In the interferometric method, the object of interest, the hot gas jet in this case, is placed in one of two otherwise similar optical paths. Light from a single source is split between the two paths and after traversing them is recombined. A pattern of straight line interference fringes is seen at the point of recombination of the two beams. As the refractive index of the hot gas differs from the surrounding medium, the optical path length in that path changes across the jet. A shift in the fringe pattern at the point of recombination of the two beams results.

This shift in the fringe pattern is related to the variation of the integrated value of refractive index along the line of sight. Since the gas jet from the Gerdien torch is assumed to have axial symmetry this line of sight information can be transformed to a radial variation by means of some numerical method, such as the well known Abel Transformation as used in other work (7,8,9), or that developed by Harker (10). Refractive index is related to density by the Gladstone-Dale relationship (11)

$$(n - 1) \propto \rho$$

Assuming the jet behaves as an ideal gas and the jet is at atmospheric pressure, the radial refractive index variation transforms to temperature variation, using

$$(n - 1) \propto 1/T$$

1.3 REVIEW OF PREVIOUS WORK

Interferometry is a well established technique in the study of high and low temperature plasmas and plasma jets (16). It is used for measuring refractive index related properties such as electron density (12) and temperature.

A Czernichowski, in his paper Interferometric Determination of Temperature in a Laminar Jet of Argon or Neon Plasma (9) used an Abel Transformation to gain radial temperature data on a plasma jet. He found an average axial temperature of 5000 K for an argon plasma jet with a gas flow rate of 18 l/min and a power supplied to the torch of 3.75 kW, though he was surprised at this value which he would have expected to be nearer 10000 K judging by the luminance of the plasma.

An unpublished work by J. Sturrock was carried out in the Leicester University Engineering Department in 1972 (13), and covered a similar topic to that of Czernichowski. Sturrock, however, measured axial temperatures in the region of 15500 K, though there is no data on argon flow rates and power to the torch.

Both these works were based on laminar argon plasma jets. The area of interest in this work, although using a similar experimental set up, is that of much lower temperatures. As the gas flow rate is lower, in the order of 1 to 3 l/min as opposed to 18 l/min, the ionised gas recombines within the torch nozzle, and unionised hot gas issues from the torch.

A further difference between the work described in this report and the previous two references is that this work deals with an impinging jet. Much work has been done on impinging jets (14,15). M Ruddy (3) used spectroscopy to study an impinging plasma jet produced by the same torch used in this work, though again at much higher temperatures. However, no references could be found that covered the use of interferometry as a tool for temperature measurements in low temperature impinging gas jets.

1.4 SPECIFIC OBJECTIVES

The specific objectives of this work can be summarised as follows:

1.4.1 Experiments

Interferograms would be photographically recorded for different conditions of the gas jet. The plasma torch, which provided the jet, would be driven by various powers and the Argon would be fed through the torch at different flow rates.

Thermocouple measurements would be taken of the temperature of the jet to obtain very rough calibration readings.

1.4.2 Calculation

The fringe shift data from the interferograms would be processed by computer to provide radial and axial temperature distributions for different physical conditions. The resulting data would be studied for any interesting trends.

A sample set of data would be submitted to various tests as an investigation of the effect on the results of the values of the physical constants assigned to the ambient conditions. Similarly the sensitivity of the interferogram fringe shift data would be investigated.

1.5 THESIS OUTLINE

The arrangement of this thesis broadly follows the brief description of the work given in sections 1.1 and 1.2.

The second chapter will contain theoretical considerations of using interferometry for temperature measurement. The relationship of refractive index to temperature will be covered, with the theory of interferometry.

The third chapter will cover the experimental part of the study. A description of the experimental apparatus will be followed by the procedure for the optical alignment of the system and the method of recording the resulting interferograms.

The fourth chapter will describe the derivation of temperature distribution from the fringe shift data. This will cover the numerical processing methods, the computer program and the interpretation of the photographs of the interferograms. Errors introduced by changing conditions will be investigated using sample data.

Chapter five will deal with the temperature distributions obtained. Both radial and axial profiles will be shown.

Chapter six will cover the discussion of results and the conclusions drawn. The temperature distributions and the different sources of inaccuracies arising in the data will be discussed. The contributions and limitations of the present work will be covered, together with directions for channelling further work.

CHAPTER II THEORETICAL CONSIDERATIONS FOR TEMPERATURE MEASUREMENT BY INTERFEROMETRY

2.1 INTRODUCTION

This chapter describes how variations in refractive index with temperature are related to interference fringe shift patterns, and how temperature is related to refractive index of a gas. The theory of interferometry is discussed, with especial reference to the Mach-Zender Interferometer, which is used in this work.

2.2 THE REFRACTIVE INDEX OF A GAS, AND ITS RELATIONSHIP TO THE TEMPERATURE OF THE GAS

Newton showed that when a parallel beam of white light passes through a prism, the emerging light is spread out into a spectrum. This phenomenon is called dispersion and implies that light of different wavelengths travels at different speeds through the medium under study. Such a medium is called a dispersive medium, and the only truly non-dispersive medium is vacuum (17).

The refractive index of a medium is defined as the ratio of the speed of light in that medium to the speed of light in a vacuum. Thus the refractive index of a dispersive medium varies with the wavelength of the incident light. Cauchy proposed an empirical formula to express refractive index in terms of wavelength:

$$(n - 1) = A + B/\lambda^2 + C/\lambda^4 + \ldots.. \qquad 2.1$$

For most gases, the refractive index is fairly well represented by the first three terms of the equation.

The constants in the equation can be obtained from tables (18). For example, for dry air, at $15^{\circ}C$ and 760 mm of Hg,

$$A = 2726.43 \times 10^{-7}$$

$$B = 122.88 \times 10^{3}\ nm^{2}$$

$$C = 355.5 \times 10^{10}\ nm^{4}$$

when the wavelength is in nanometers. When $\lambda = 632.8$ nm, the wavelength of a He-Ne laser, the refractive index of dry air at $15^{\circ}C$ and 760 mm of Hg is

$$(n - 1) = 0.0002759 \qquad 2.2$$

Similarly, the refractive index of Argon is 0.000281.

It is possible to prove, from electromagnetic theory, that, at low pressures, the refractive index of a gas is proportional to its density (17). This result had also been confirmed experimentally by Gladstone and Dale (11).

The Lorentz-Lorenz equation (11) also relates refractive index to density, in

$$(n^2 - 1)/(n^2 + 2) \propto \rho \qquad 2.3$$

where ρ is the density of the gas with refractive index $(n - 1)$. For Argon, the value of n is of the order 1.0003, in which case equation 2.3 can reduce to

$$(n - 1).(2/3) \propto \rho \qquad 2.4$$

$$(n - 1) \propto \rho$$

As the pressure of the gas in the work under study is essentially atmospheric, and as such can be considered constant, the change in density of the gas can be assumed to be caused by a change in temperature. Hence, from the gas laws,

$$\rho_1/\rho_2 = T_2/T_1 \qquad 2.5$$

where T is the absolute temperature. It can therefore be assumed that

$$(n - 1) \propto 1/T \qquad 2.6$$

That is, the refractive index of a gas is inversely proportional to its temperature.

This assumption breaks down when the gas can no longer be considered a dielectric. That is when the gas becomes ionised and hence an electrical conductor. In the case of argon, the gas under consideration, however, it can be shown, using Saha's equation (19), that there is no appreciable ionisation below approximately 8000 K, as plotted in Fig. 2. Initial thermocouple readings indicated that the gas jet under study was at much lower temperatures than this. It was therefore considered adequate to use the relationship in equation 2.6 to relate refractive index to temperature in this work, thus

$$T_2 = \frac{(n - 1)_1 \, T_1}{(n - 1)_2} \qquad 2.7$$

where $(n - 1)_1$ is the refractive index of the gas calculated, using Cauchy's formula, equation 2.1, at temperature T_1, and $(n - 1)_2$ is the refractive index measured experimentally at the unknown temperature T_2.

A curve of refractive index against temperature for atmospheric argon is shown in Fig. 1, calculated from equation 2.7.

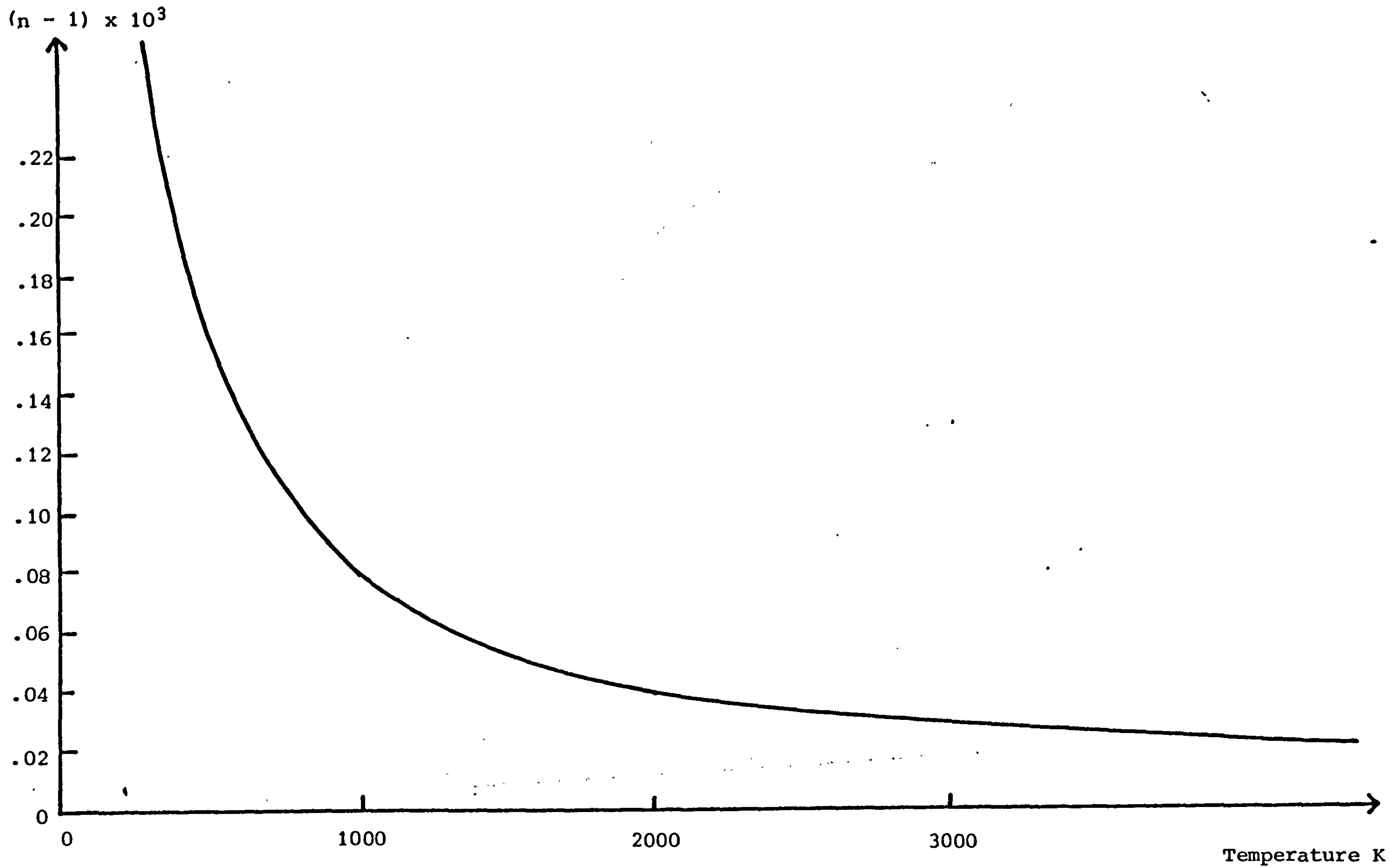

Fig. 1. Refractive Index against Temperature for atmospheric Argon.

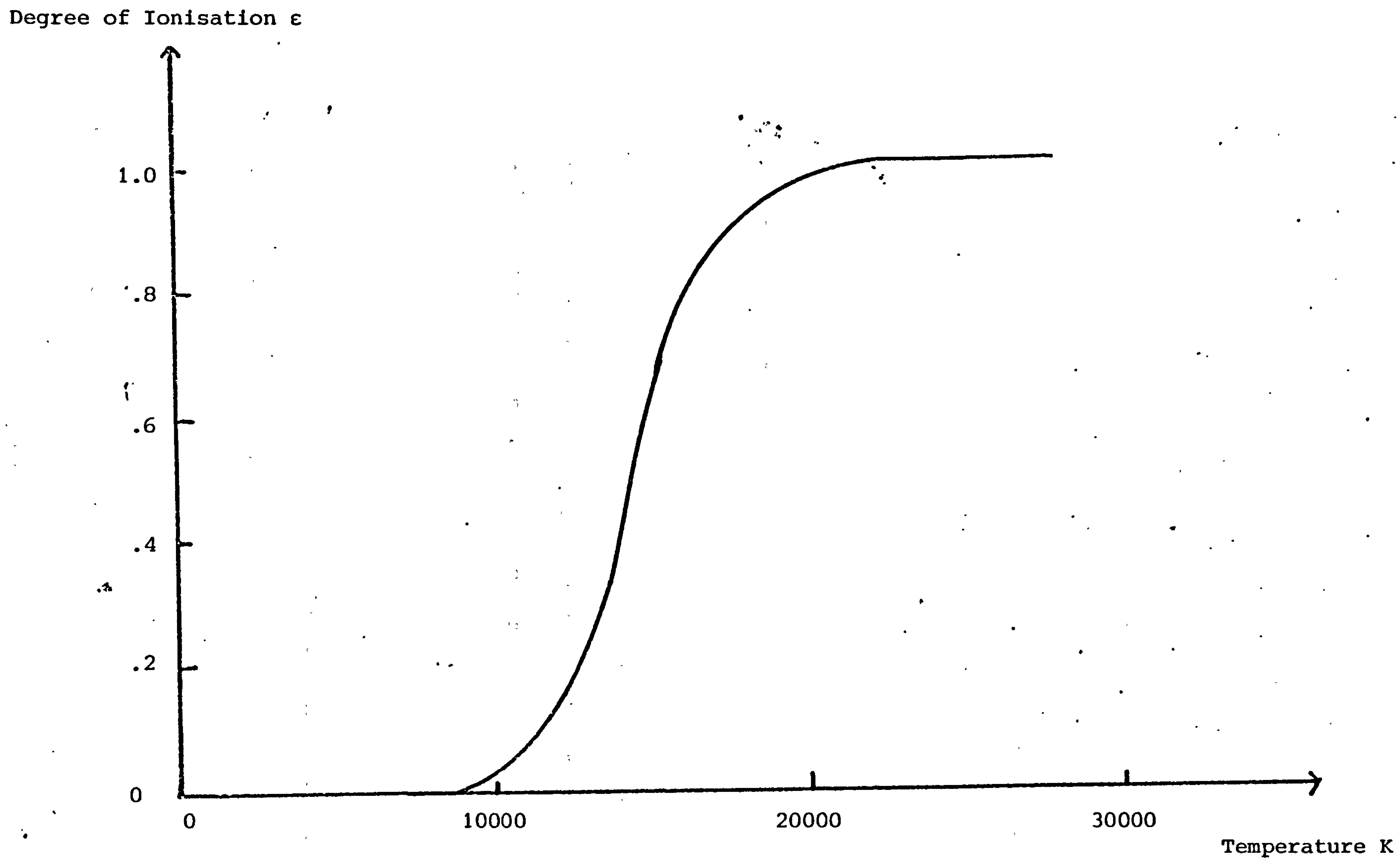

Fig. 2. Degree of Ionisation against Temperature for singly ionised atmospheric Argon.

2.3 THE THEORY OF INTERFEROMETRY

2.3.1 The Formation of Interference Fringes

The formation of optical interference fringes results from the principle of superposition of electromagnetic fields, light being such a field. Considering two plane waves of light, one travelling in the positive z direction and the other at an angle θ to the z axis, with maximum amplitudes a_1 and a_2, as shown in Fig. 3, then the complex amplitudes of the waves, ignoring the time factor, $\exp 2\pi i\nu t$, of the wave equation on the assumption that the waves are monochromatic and hence of the same frequency, are given by (20)

$$U_1 = a_1 \exp\left(\frac{-2\pi}{\lambda}\right) iz$$

$$U_2 = a_2 \exp\left(\frac{-2\pi i}{\lambda}(y\sin\theta + z\cos\theta)\right) \qquad 2.8$$

From the principle of superposition, the resultant light amplitude, when the two beams cross, is obtained from the sum of the amplitudes of the two beams, and the resulting complex amplitude is given by

$$U = U_1 + U_2 \qquad 2.9$$

The instantaneous light power, or intensity, of a liaht beam is proportional to the square of the amplitude of that beam. The observed intensity of the above example is

$$I = UU^* = |U_1|^2 + |U_2|^2 + U_1U_2^* + U_1^*U_2$$

$$= |U_1|^2 + |U_2|^2 + 2\mathrm{Re}U_1U_2^* \qquad 2.10$$

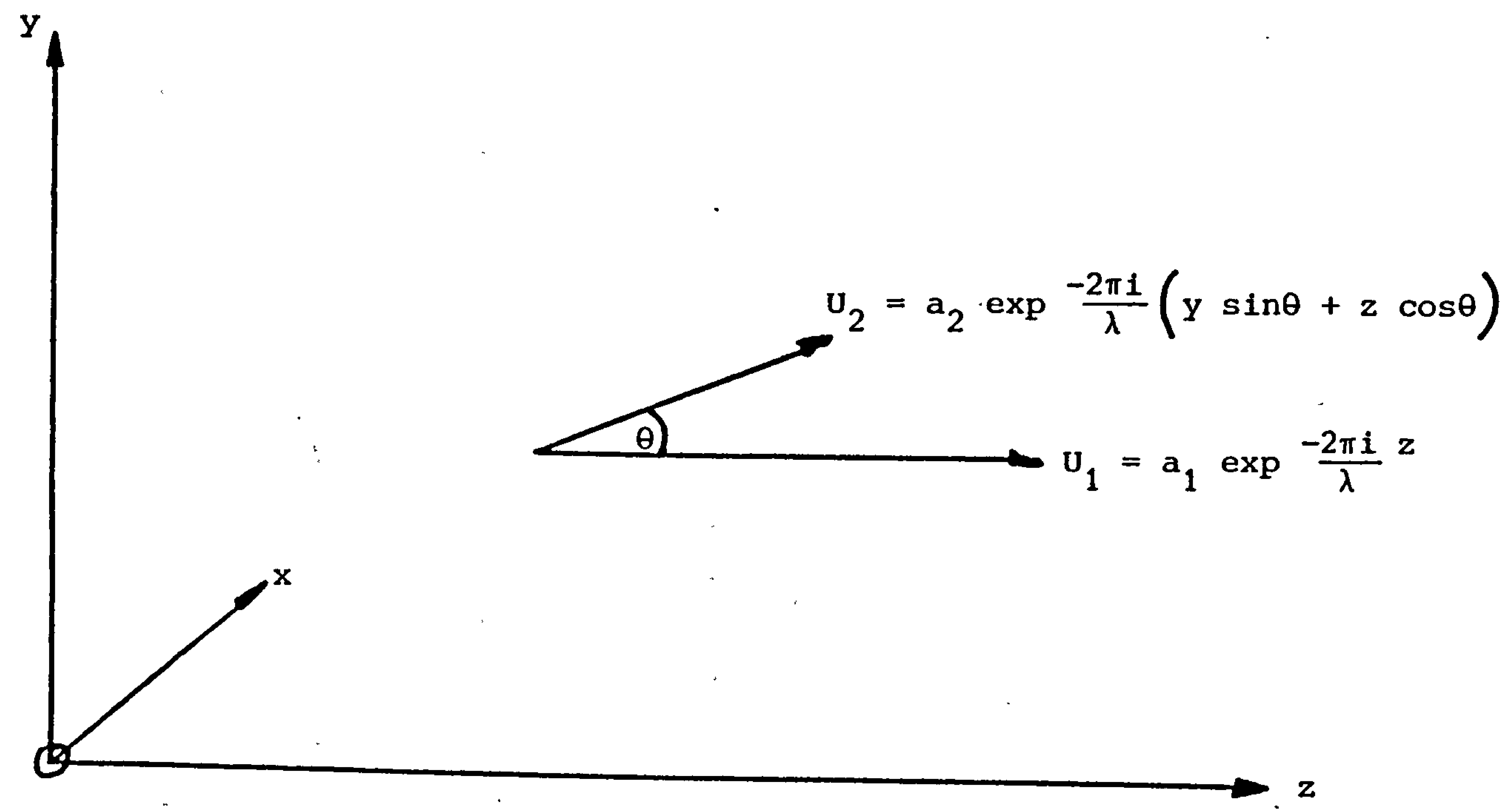

Fig. 3. Interference of two plane waves of light.

where Re indicates that the real part of the expression which follows is to be taken, and * indicates the complex conjugate.

Thus, from equations 2.8 and 2.10, the intensity of two intersecting beams is

$$I(y) = a_1^2 + a_2^2 + 2a_1a_2\cos\left(\frac{2\pi y}{\lambda}\sin\theta\right) \qquad 2.11$$

As $y \sin\theta$ varies, the intensity varies, giving a bright fringe whenever $y \sin\theta$ is equal to an integer number of wavelengths, and a dark fringe when it is equal to $(N + \frac{1}{2})\lambda$. If the amplitudes of the two beams are equal, the dark fringes are completely black.

These interference fringes are usually caused by light which travels between a source and a point by two different routes. The beams therefore arrive with different phases due to the different optical paths traversed. This phase difference is related to the optical path differences by the equation

$$\text{phase difference} = (2\pi/\lambda).\ \text{optical path difference} \qquad 2.12$$

and a complete fringe shift indicates a phase change of 2π.

Instruments which measure this phase difference, and hence change in optical path length, from interference fringes are called interferometers.

2.3.2 The Interferometer

The interferometer is an instrument which uses the described optical interference phenomena to measure refractive index, or change in refractive index in one of its beams of light by studying the change in optical path length as indicated by interference fringe patterns.

Most interferometers use two beam interferometry, the basis of which is the splitting of a coherent, usually monochromatic (to eliminate the time dependent factor in the wave equation), beam of light into two beams. These beams then travel via two different optical paths to be reunited at some point, where interference fringes are formed.

The intensity at the point of recombination is governed by the phase difference between the two beams, which, in turn, from equation 2.12 is governed by the optical path difference.

There are two methods of splitting a beam of light (17): division of wavefront, where the light goes through two apertures side by side; and division of amplitude, where the light is split at one or more reflecting surfaces.

Divison of wavefront is used in various types of interferometer, such as Fresnel's mirrors and Lloyd's mirror used to measure the wavelength of the incident light, the Rayleigh interferometer, used to measure optical path difference to test optical elements, and the Michelson stellar interferometer, used to measure the angular distance between astronomical objects. Interference patterns set up by this type of interferometer can easily be seen by the Young's double slit experiment, as shown in Fig. 4.

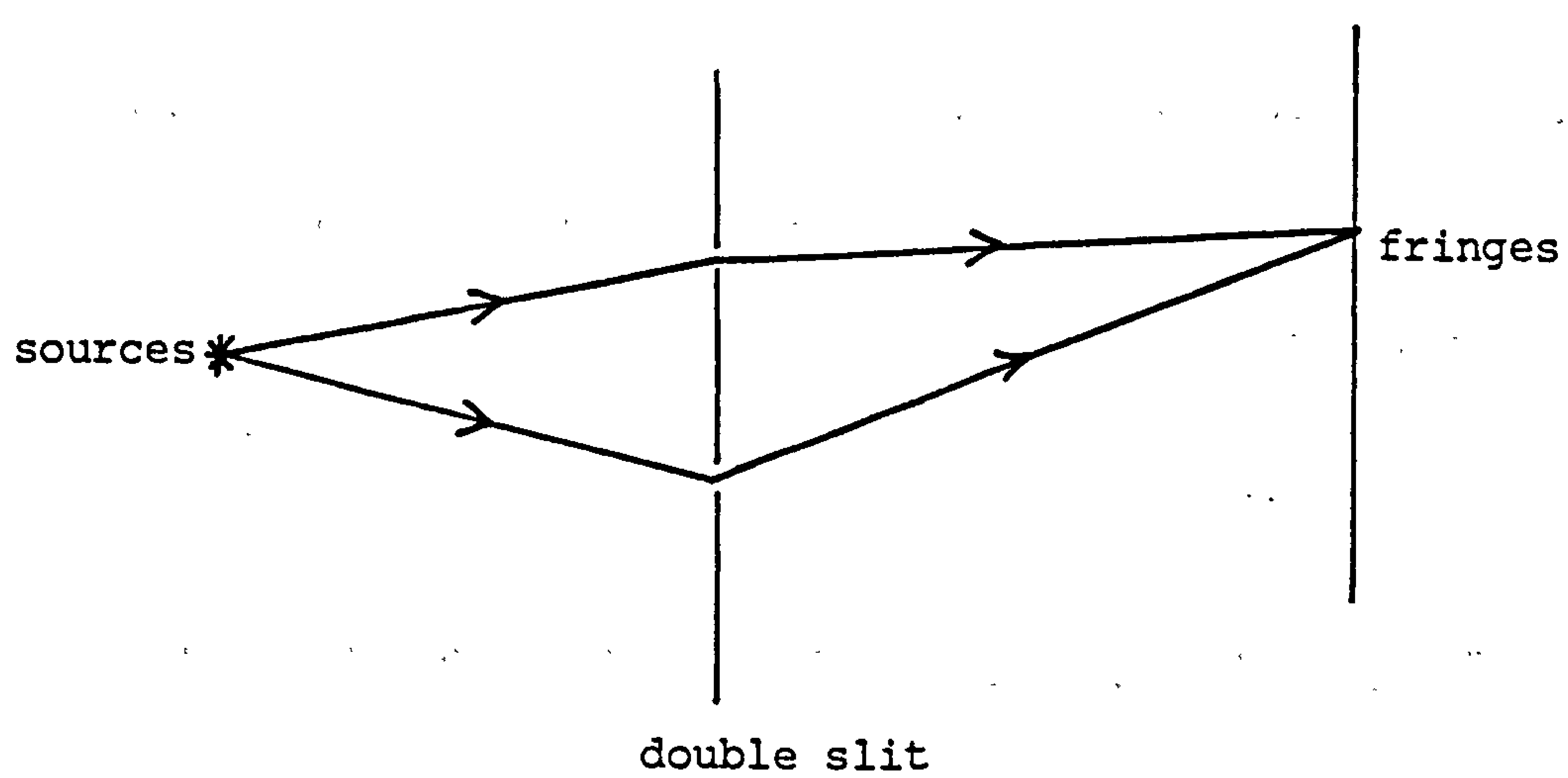

Fig. 4. Young's Experiment.

Interference patterns set up by a division of amplitude interferometer are seen when a plane parallel plate of transparent material is illuminated by a point source of monochromatic light. As can be seen in Fig. 5 because some of the light is reflected off the top surface and some is reflected off the bottom surface, a difference in optical path lengths occurs and fringes are formed.

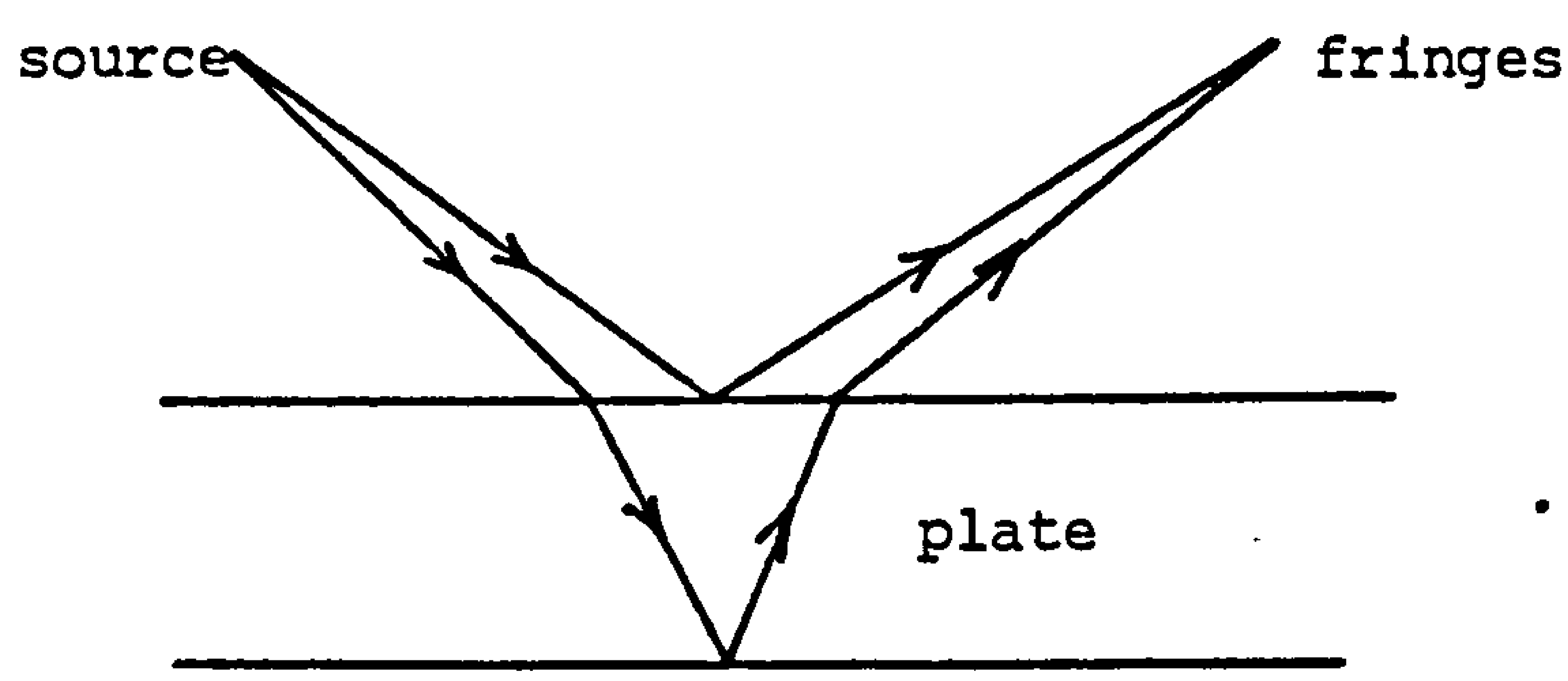

Fig. 5. A plane parallel plate illuminated by a point source.

Division of amplitude is used in various interferometers, e.g. Michelson, Twyman-Green, Jamin. These are all used for checking optical instruments for aberration, measuring the flatness of reflecting surfaces and measuring the change in refractive index from some reference.

Another division of amplitude interferometer is the Mach-Zehnder (21,22). This is often used to measure variations in refractive index, and hence other related properties in fluid and gas flow situations, and was used in the work reported.

2.3.3 <u>The Mach-Zehnder Interferometer and its Formation of Fringes</u>

A schematic layout of a Mach-Zehnder interferometer is shown in

Fig. 6. The Mach-Zehnder has an advantage over other division of amplitude interferometers in that virtual fringes can be localised in the area under study and hence maximise fringe contrast.

Light from a source placed in the focal plane of a well corrected lens, L_1, is divided at the semi-reflecting surface, A_1, of a plane parallel glass plate, B_1, into two beams. These, after reflection at plane mirrors, M_1 and M_2, are recombined at the semi-reflecting surface A_2, of a second identical plane parallel plate, B_2. They emerge and are focussed by a well corrected converging lens L_2. The four reflecting surfaces are arranged initially parallel, with their centres at the corners of a parallelogram.

Assuming there is a point source of monochromatic light illuminating the system and there are no disturbances in either beam, plane wavefronts W_1 and W_2 are formed. If W_1' is the virtual wavefront between M_2 and B_2 corresponding to W_1, then at a point P on W_2, the virtual phase difference between the two emergent beams, δ, is

$$\delta = 2\pi(n - 1)h/\lambda \qquad 2.13$$

where h is PN, the normal distance of W_1' from P and the geometrical path difference, (n - 1) is the refractive index between M_2 and B_2, and λ is the wavelength of the illuminating light. This is equivalent to equation 2.12, as optical path length = (n - 1)h.

When W_1' and W_2 are mutually inclined, straight line fringes are formed. By rotating M_2 and B_2 the plane of intersection of the two wavefronts can be rotated and hence the orientation of the fringes, which are parallel to the plane of intersection, can be positioned in the best direction for ease of analysis. In this case fringes were positioned horizontally, as this

Fig. 6. Mach-Zehnder Interferometer, showing formation of fringes.

gave an easily defined undisturbed fringe field on either side of the shifted fringes.

If the indices of refraction in the paths of the two beams of the interferometer are $(n_1 - 1)$ and $(n_2 - 1)$ and the two geometrical path lengths are l_1 and l_2, then the places where the fringe maxima occur are satisfied by the equation

$$(n_1 - 1)l_1 - (n_2 - 1)l_2 = N\lambda \qquad 2.14$$

where N is an integer.

A change in refractivity of the medium through which one beam passes changes the optical path length of that beam, and hence the position at which the above condition is fulfilled. As a result, a shift appears in the fringe system, which can be expressed as (4)

$$s = L\Delta(n - 1)/\lambda \qquad 2.15$$

where s is the fringe shift in the number of fringes, L is the length of the object in the light path, $\Delta(n - 1)$ is the change in the refractive index between the reference beam and the object in the light path, and λ is the wavelength of the light.

In the medium under study, an impinging hot gas jet, the refractive index is not constant, but varies radially in the jet as the temperature varies. Thus the refractive index at points across the beam passing through the jet is an integral of the radial refractive indices of the jet.

This leads to an equation relating fringe shift to refractive index

$$s_y\lambda = \int_{-x_0}^{x_0} \Delta(n - 1)_r \, dx$$

$$= \int_{-x_0}^{x_0} (n - 1)_{air} - (n - 1)(r)_{jet} \, dx \qquad 2.16$$

where $s_y\lambda$ is the fringe shift multiplied by the wavelength, and hence, from equation 2.12 and 2.15, the optical path length through the object, at position y from the axis of the jet. $(n - 1)_{air}$ is the refractive index of the air and $(n - 1)(r)_{jet}$ is the refractive index of the jet at radius r. The geometrical conventions are shown in Fig. 21.

The solution of this equation for $(n - 1)(r)$ is covered in Chapter 4. Once $(n - 1)(r)$ has been obtained, the radial temperature of the jet can be calculated, using equation 2.6

$$T_2 = \frac{(n - 1)_1 T_1}{(n - 1)_2}$$

CHAPTER III EXPERIMENTAL INVESTIGATION OF TEMPERATURE PROFILES

3.1 INTRODUCTION

This chapter describes the experimental apparatus which was used to provide the impinging hot gas jet under investigation, and the equipment used to form interference fringes focussed onto photographic film. The setting up of the apparatus and the recording of the interferograms is also described.

3.2 DESCRIPTION OF THE EXPERIMENTAL APPARATUS

3.2.1 The gas jet and cool surface

To provide gas jets with temperatures of between 300 K and 8000 K a plasma torch of the Gerdien type, supplied by British Rail for previous workers (2,3) was used. This torch is shown schematically in Fig. 7. Argon passes between a thoriated tungsten cathode and a copper anode which are water cooled. The gas is heated by an arc struck between these two electrodes. After passing through the arc, the gas flows through a short nozzle in the anode and out to the atmosphere.

The condition of the ensuing jet is dependent on the electrical supply to the arc and the gas flow rate. A Gerdien torch is normally operated at high electrical power inputs and argon flow rates. Under these conditions the gas is strongly heated to temperatures well above 8000 K when it becomes ionised. This plasma is blown through the nozzle and emerges as a highly intense radiating source. However, at low argon flow rates and low electrical power although the gas is ionised by the arc, recombination takes place within the nozzle. The emerging jet is in the main a hot unionised stream although under some conditions a small luminous cone a few milli-

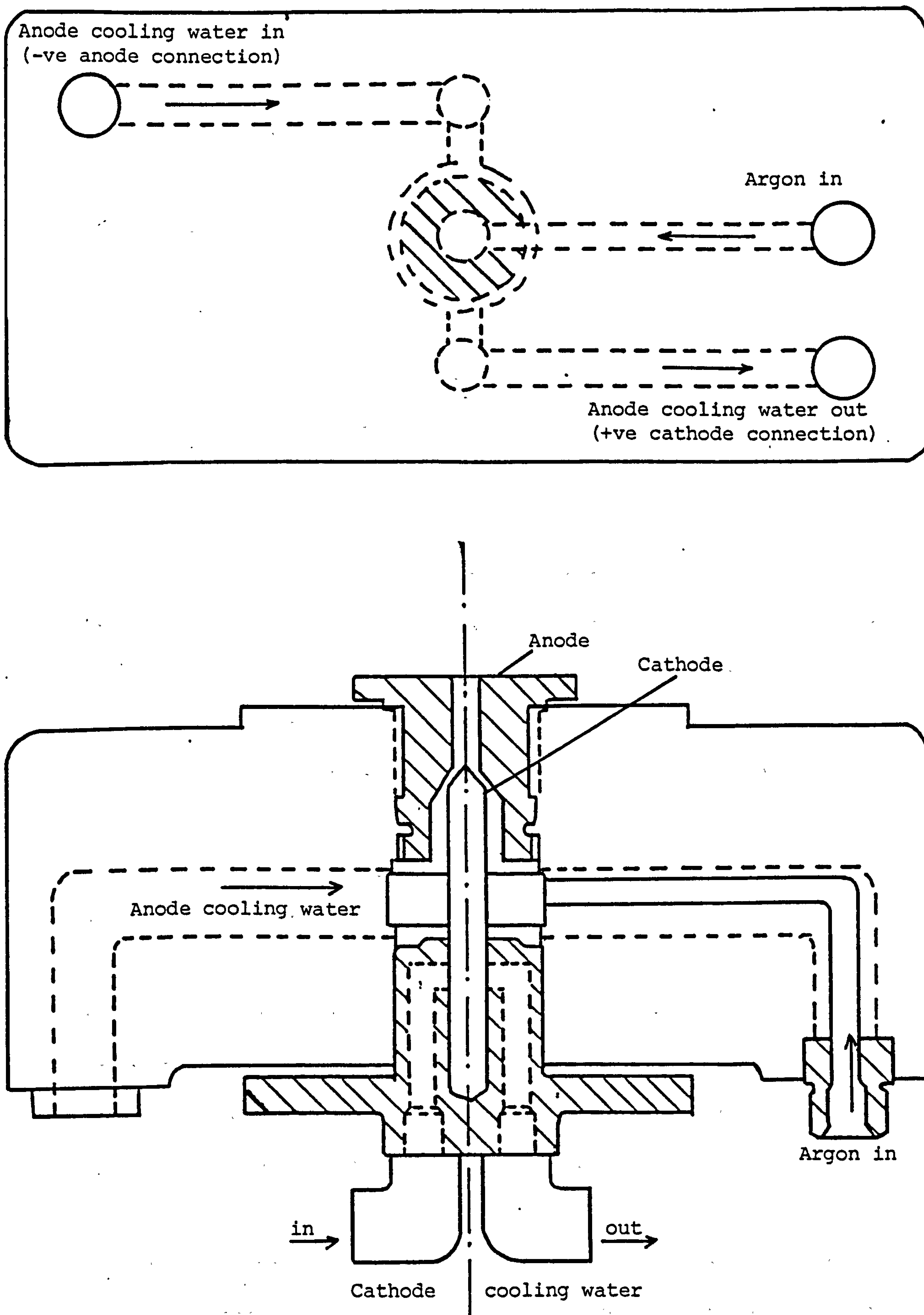

Fig. 7. Plasma Torch.

metres long forms at the exit. This indicates the recombination process is completed just outside the torch.

The gas flow rate to the torch was metered on a size 7 metric rotameter, the calibration curves for which are shown in Fig. 8 and calculated in Appendix AIV. The cooling water flow rate was measured on a size 10 metric rotameter, which was directly calibrated.

The power supply to the torch was provided by a welding transformer supplied by the British Oxygen Company, and has been described in detail by Maxwell and Ruddy (23). It was a stabilised arc furnace rectifier unit, with three phase 440 volt output, rectified and stepped down to three 150 volt open circuit DC terminals. The arc in the torch head was initiated by a high frequency spark, which was switched off once the torch was struck and a DC current was being transmitted. The current into the torch was measured by a meter on the power supply, and the DC voltage drop across the torch was measured by a digital volt meter across the torch terminals.

A block diagram of the plasma torch supply system is shown in Fig. 9 and a photograph of the rectifier unit in Fig. 10.

The jet was played over a cool surface. This was provided by a water cooled copper cylinder, 40 mm in diameter, rotated at approximately 33 rpm by a simple DC motor and belt drive. The cylinder was mounted so the cool surface was 30 mm above the nozzle of the torch.

The torch and rotating cylinder were mounted on a free-standing pedestal, shown in the photograph in Fig. 11, which could be moved to position the jet in the measurement beam of the interferometer.

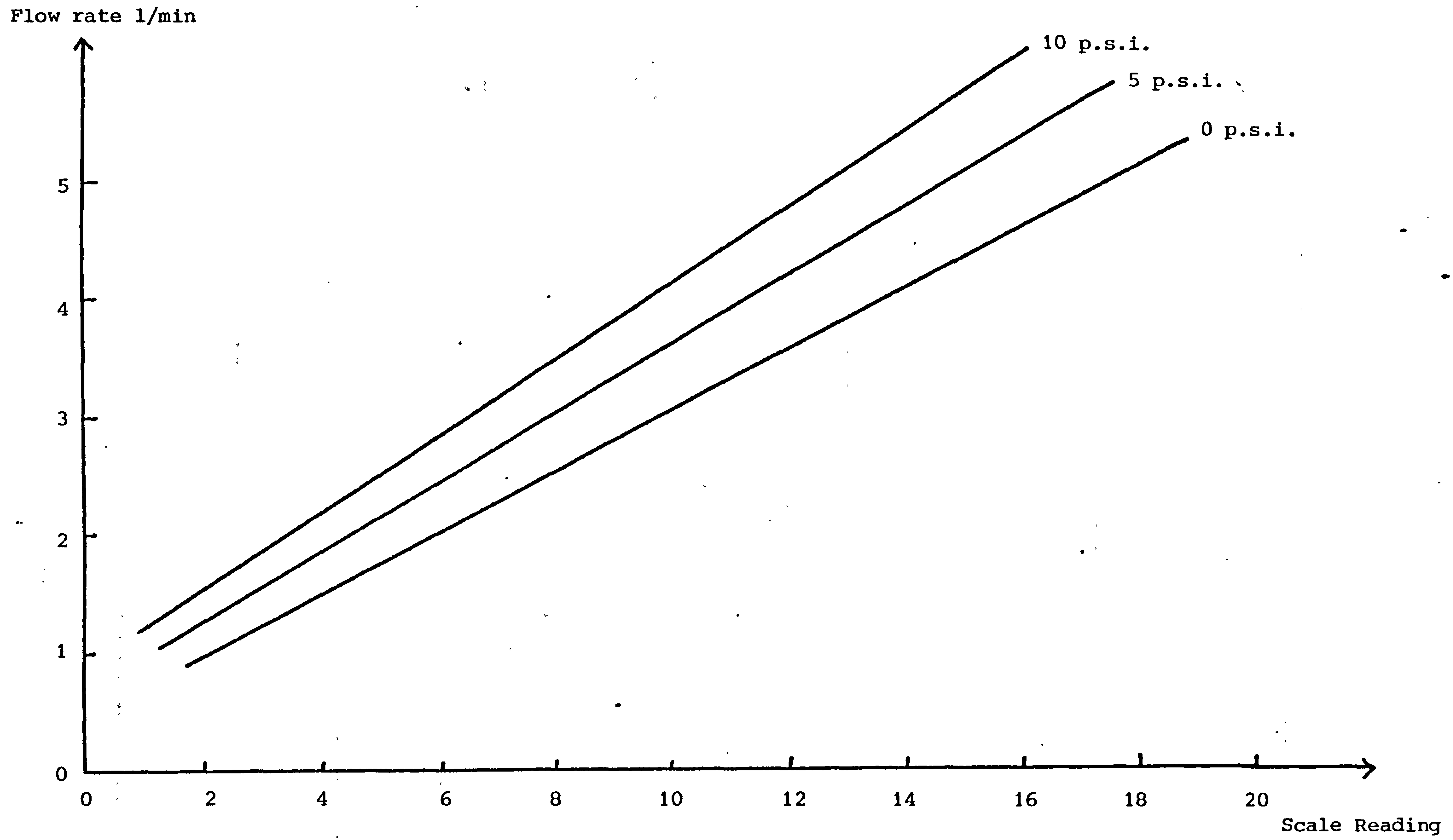

Fig. 8. Calibration Curves for Size 7 Metric Rotameter.

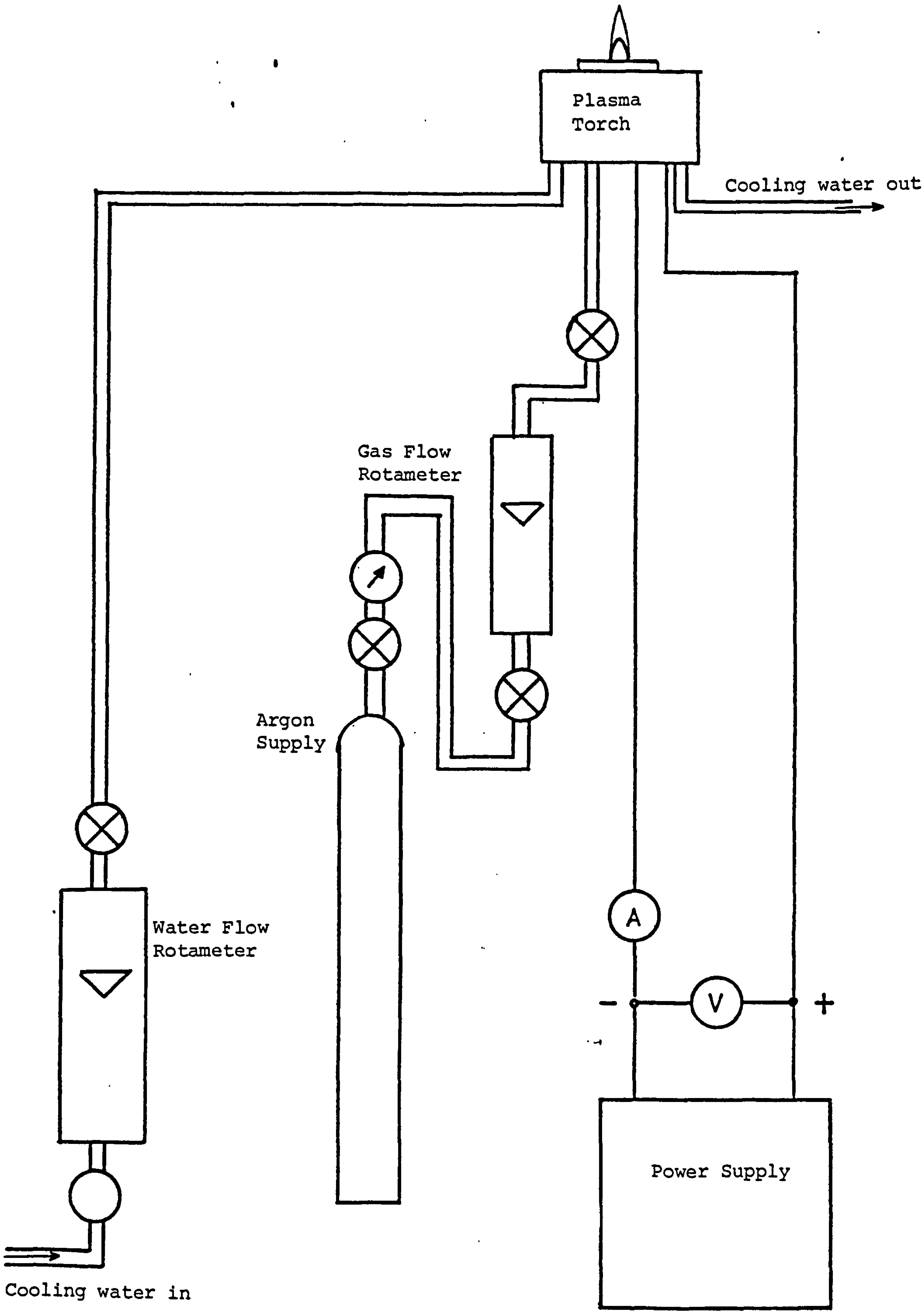

Fig. 9. Plasma Torch Supply System.

Fig. 10. Power Supply.

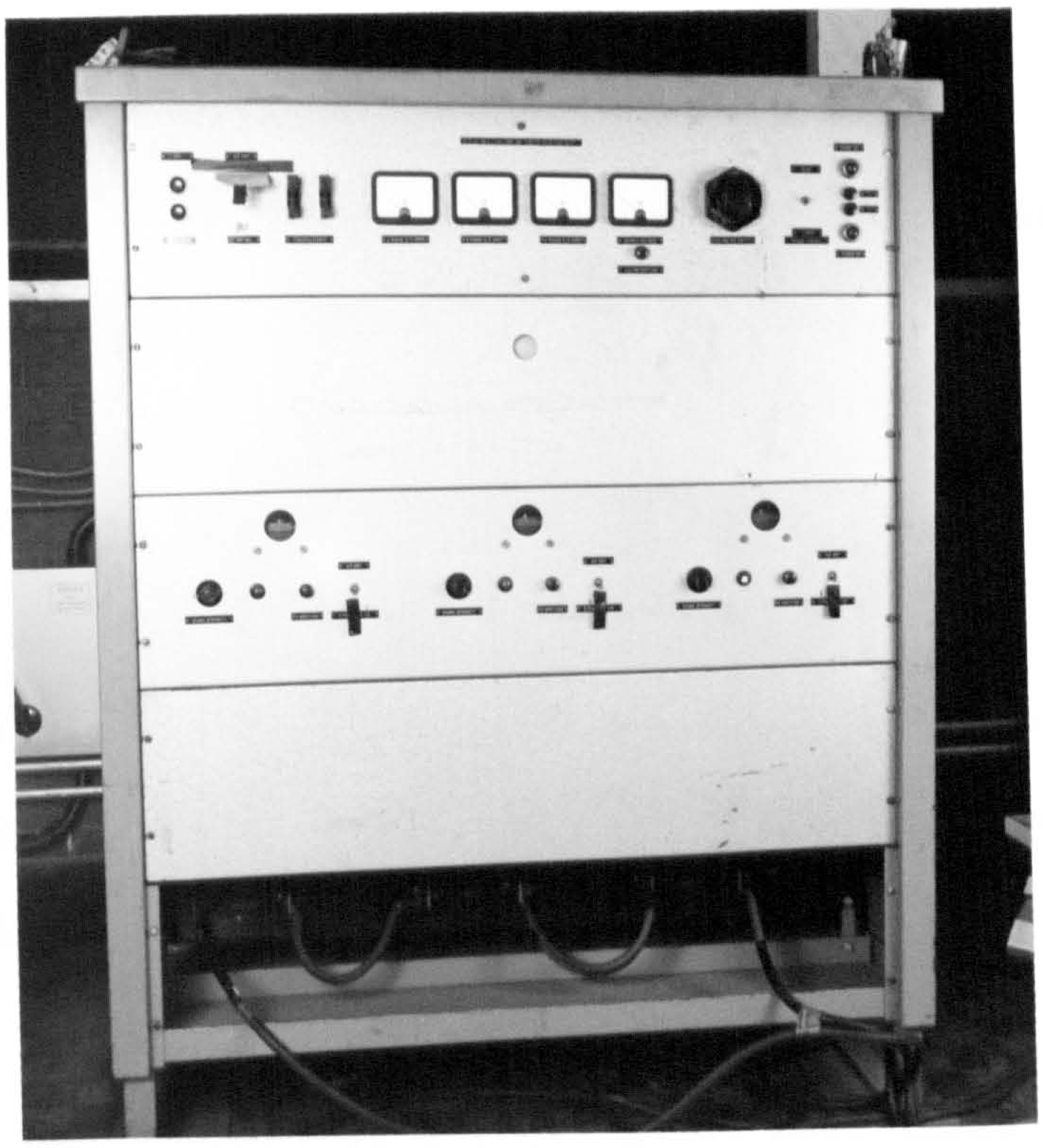

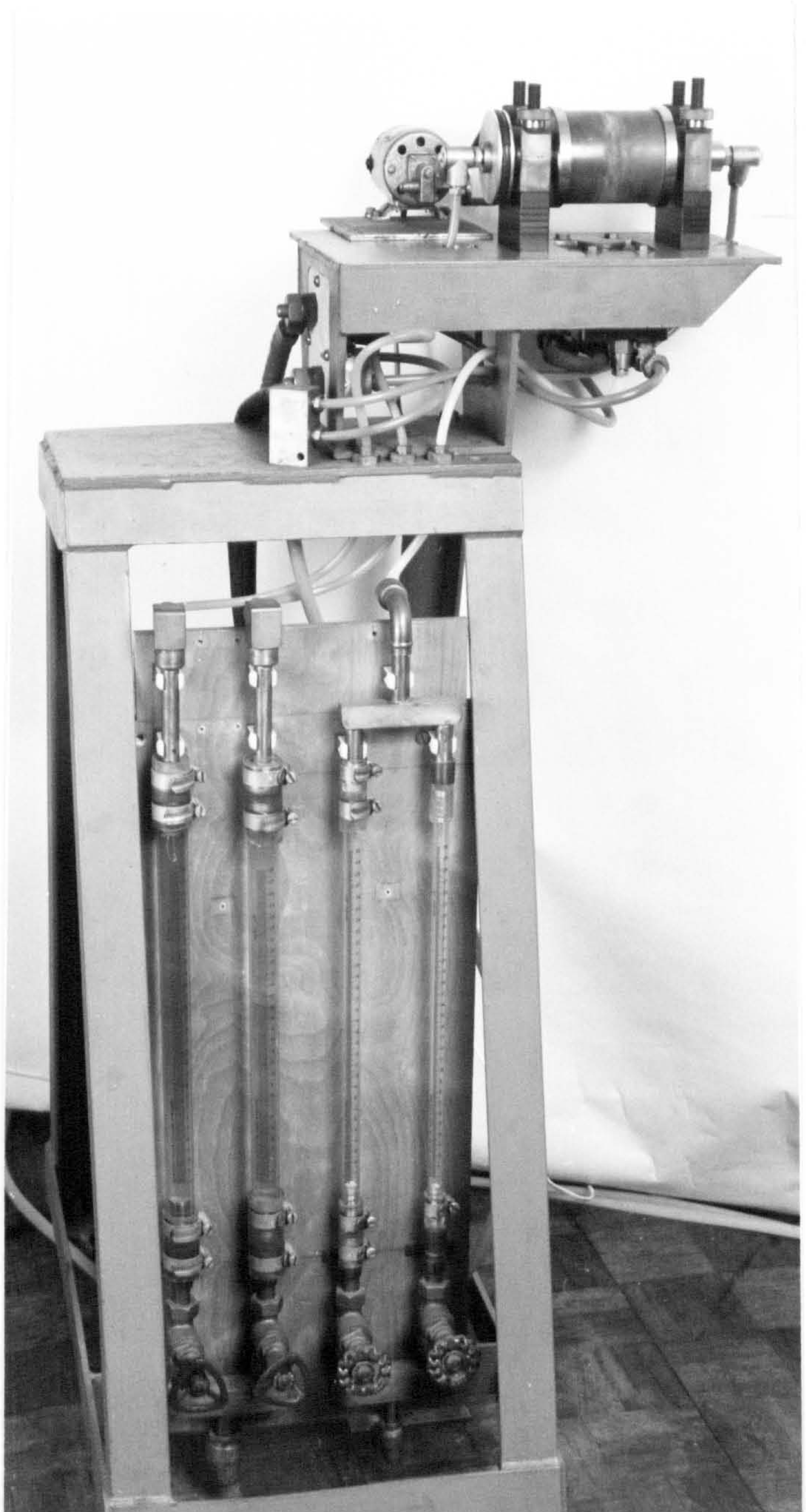

Fig. 11. Plasma Torch showing copper cylinder and supply rotameters.

3.2.2 The Interferometer

Equipment which could be used as a Michelson (17) or a Mach-Zehnder (24) interferometer was available in the department. With the Michelson interferometer, as shown in Fig. 12a the measurement beam passes through the object under investigation twice, whereas with the Mach-Zehnder, as shown in Fig. 12b the beam only passes through the jet once. With the Mach-Zehnder configuration it is also possible to localise the fringes in the jet, as covered in Chapter 2, which is not possible with the Michelson. Therefore the Mach-Zehnder configuration was used.

The equipment, as shown in Fig. 13, consists of a rectangular base table which can be made level horizontally by means of four adjustable legs. There is a cutout along one side, to accommodate the plasma torch.

At the four corners there is either a mirror or a beam splitter; Figs. 14 and 15 show the two beam splitters, B_1 and B_2, and the two mirrors, M_1 and M_2. The mirrors have a plane silvered surface, of diameter 75 mm. The beam splitters, of diameter 76 mm, are made of 15 mm thick Borosilicate Crown glass with each surface polished to a flatness of 1/10 wavelength. The substrate is Fused Silica of a like flatness and similar thickness. The front surface, common with the Borosilicate Crown glass, has an Inconel 30:30 coating, which allows equal transmission and reflection for unpolarised light, with 40% loss due to absorption. The rear surface of the substrate is coated with a single anti-reflection coating of magnesium flouride, which makes the parallel plate fringes sufficiently faint to be negligible.

The beam splitter B_1 can be rotated about a horizontal axis to allow the light beam to be adjusted to pass along both paths parallel to the base table. It can also be rotated about a vertical axis to allow the

Text cut off in original

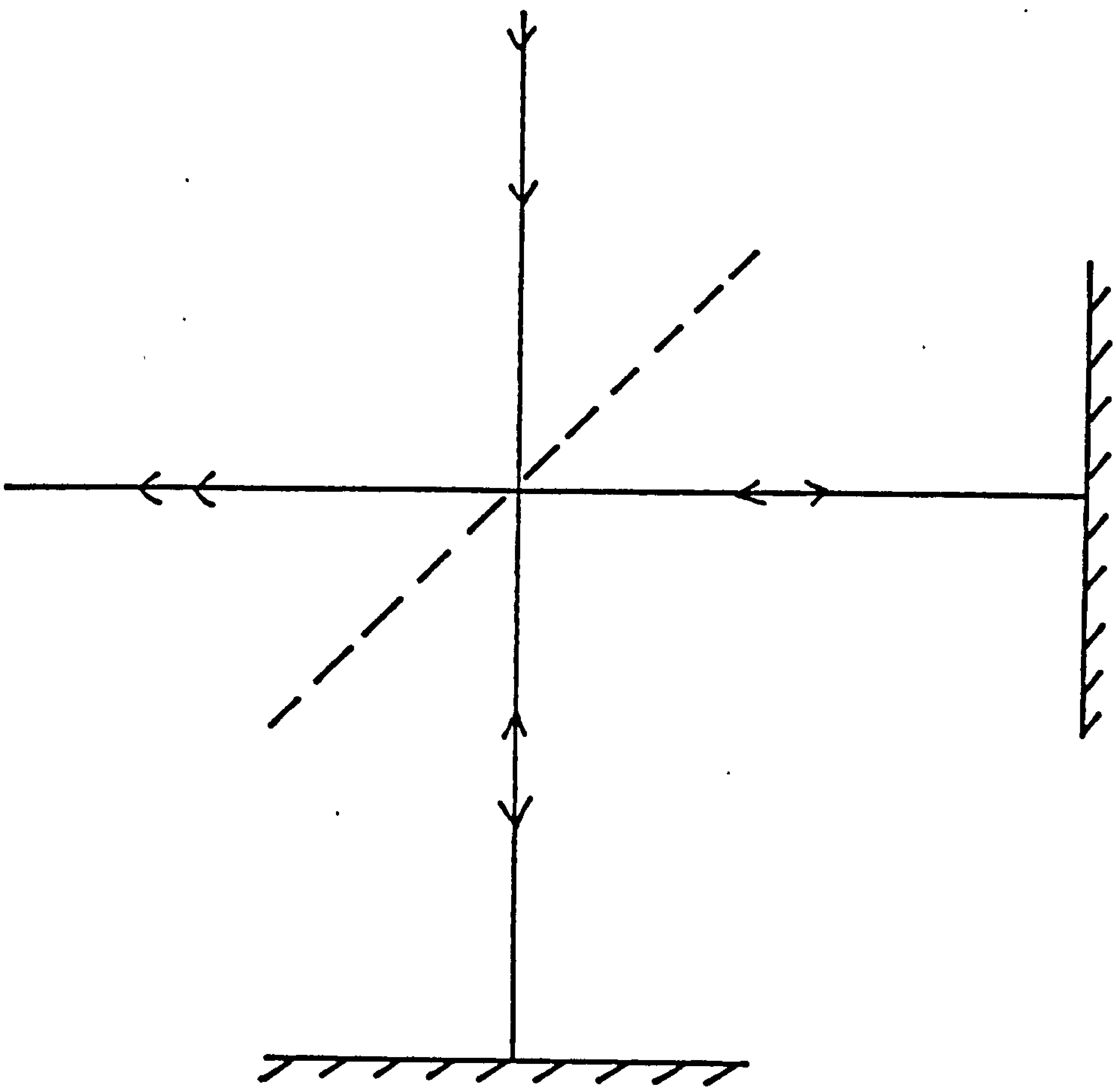

Fig. 12a. Michelson Interferometer.

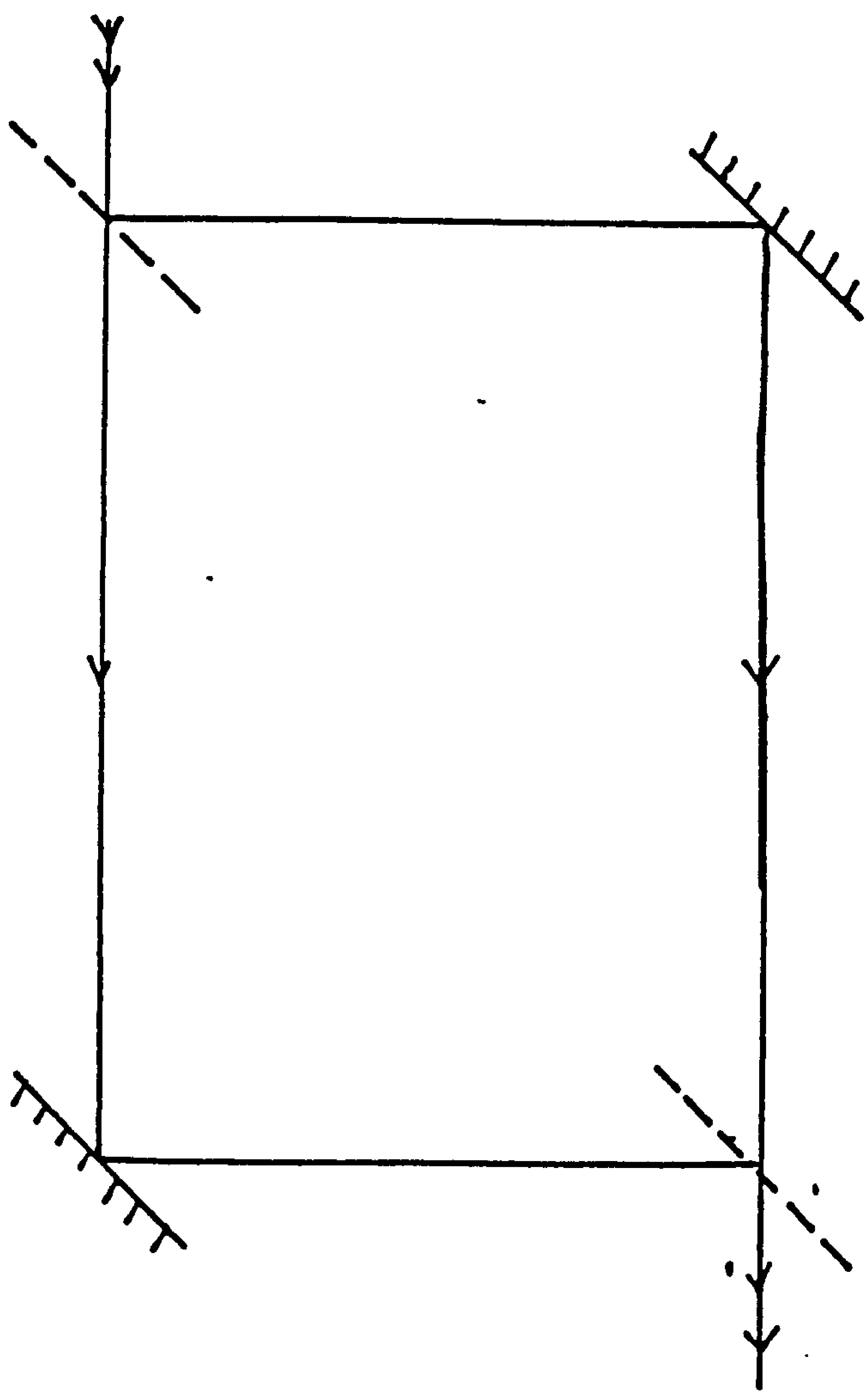

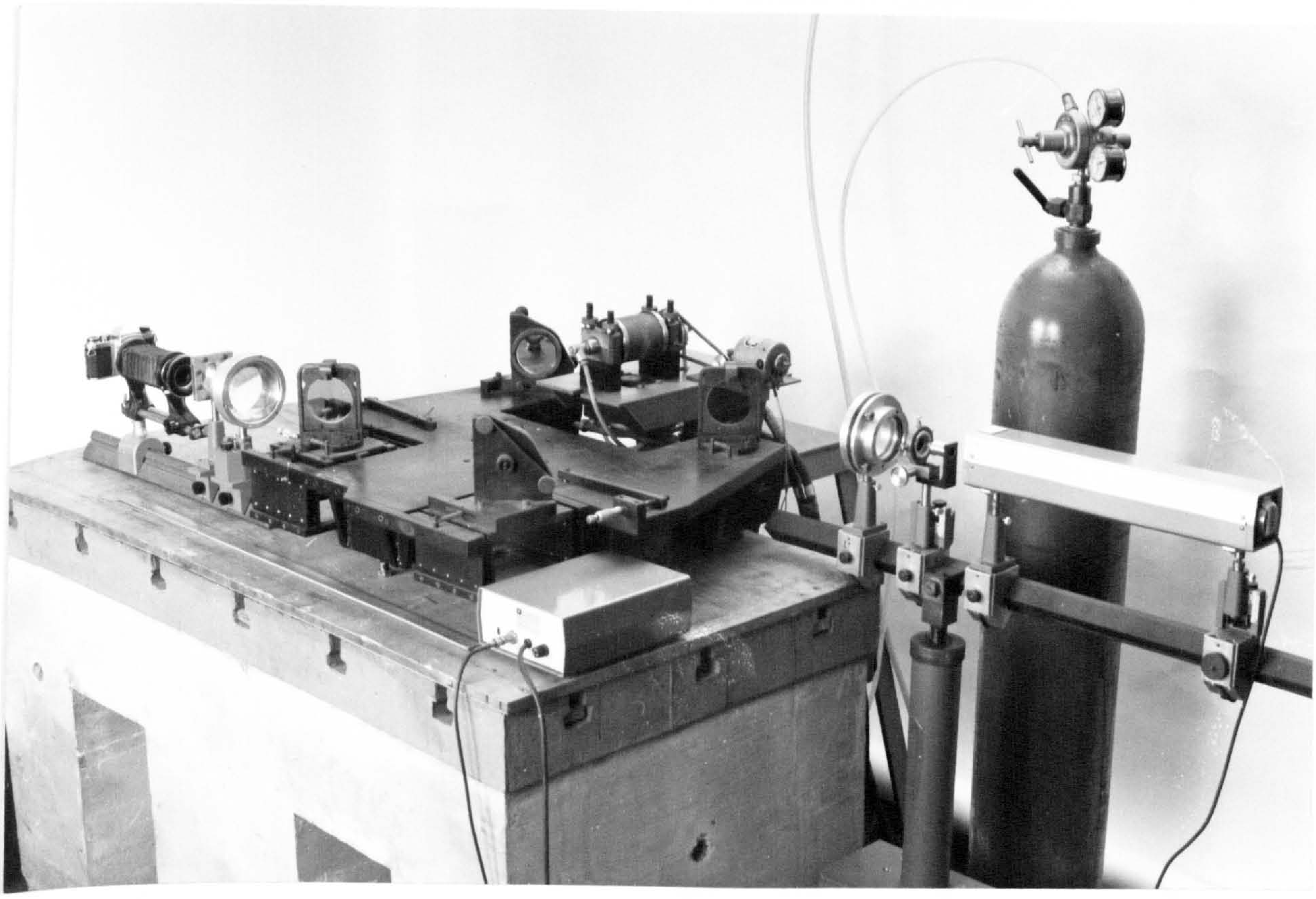

Fig. 13. Photograph of Mach-Zehnder Interferometer.

Fig. 14. Experimental Arrangement.

Fig. 15. Mach-Zehnder Interferometer.

reflected beam to be positioned at the centre of the mirror M_1.

Both mirrors can be rotated about the horizontal and vertical axes, and also translated in their own planes. In addition, M_2 can be translated in the direction of the impinging light, to lengthen or shorten the geometrical path length of the reference beam.

The second beam splitter, B_2, can be rotated about the two axes, and also translated in the two directions of the impinging light.

The translation of the beam splitter B_2 and the mirror M_2 in the direction of the impinging light is effected by component mounting plates, placed in recesses in the main base table and connected to it by kinematic joints. A wire and pivot arm is tensioned by a spring between the mounting plate and the base table, on the far side of the mount. The arm transmits motion from a micrometer screw to the mounting plate.

The translation of the beam splitter perpendicular to the direction of the impinging light is provided by a slide arrangement. This is adjusted directly by a micrometer screw with an opposing tension spring. Despite the kinematic joint, the mounts are not stable enough to prevent local structural vibrations affecting the fringes. As a result, when the mirror and beam splitter have been correctly adjusted, they have to be wedged into position.

In the reference beam, between B_1 and M_2, a template of 20 mm is set up so that a scale can be established for the fringes when they are photographed.

The whole interferometer is mounted on an antivibration concrete table.

3.2.3 The Illuminating System

The system is illuminated by a Spectra Physics Model 120 5 mW He-Ne laser, with a Model 256 Exciter. The laser operates in the TEM_{00} mode, giving red light of 632.8 nm wavelength. The beam emitted by the laser, of 1.5 mm diameter, is expanded and collimated to provide the interferometer with a plane wavefront large enough to fill the mirrors.

A microscope objective is used to expand the beam. At the focal point of this lens a pinhole is employed to act as a spatial filter, and remove the diffraction patterns of particles and aberrations in the microscope objective, which would upset the coherence of the light.

Ideally the rim of the pinhole should coincide with the first minimum in the focal plane diffraction pattern. This isolates the Airy Disc, which contains 84% of the light (17), as can be seen in the intensity distribution shown in Fig. 16.

A Beck 10x objective is used, this being a suitably short focal length, yet not short enough to cause serious problems due to aberrations. A pinhole of 25 µm diameter is used, this size allowing for ease of adjustment, yet filtering the beam to an adequate smoothness of intensity.

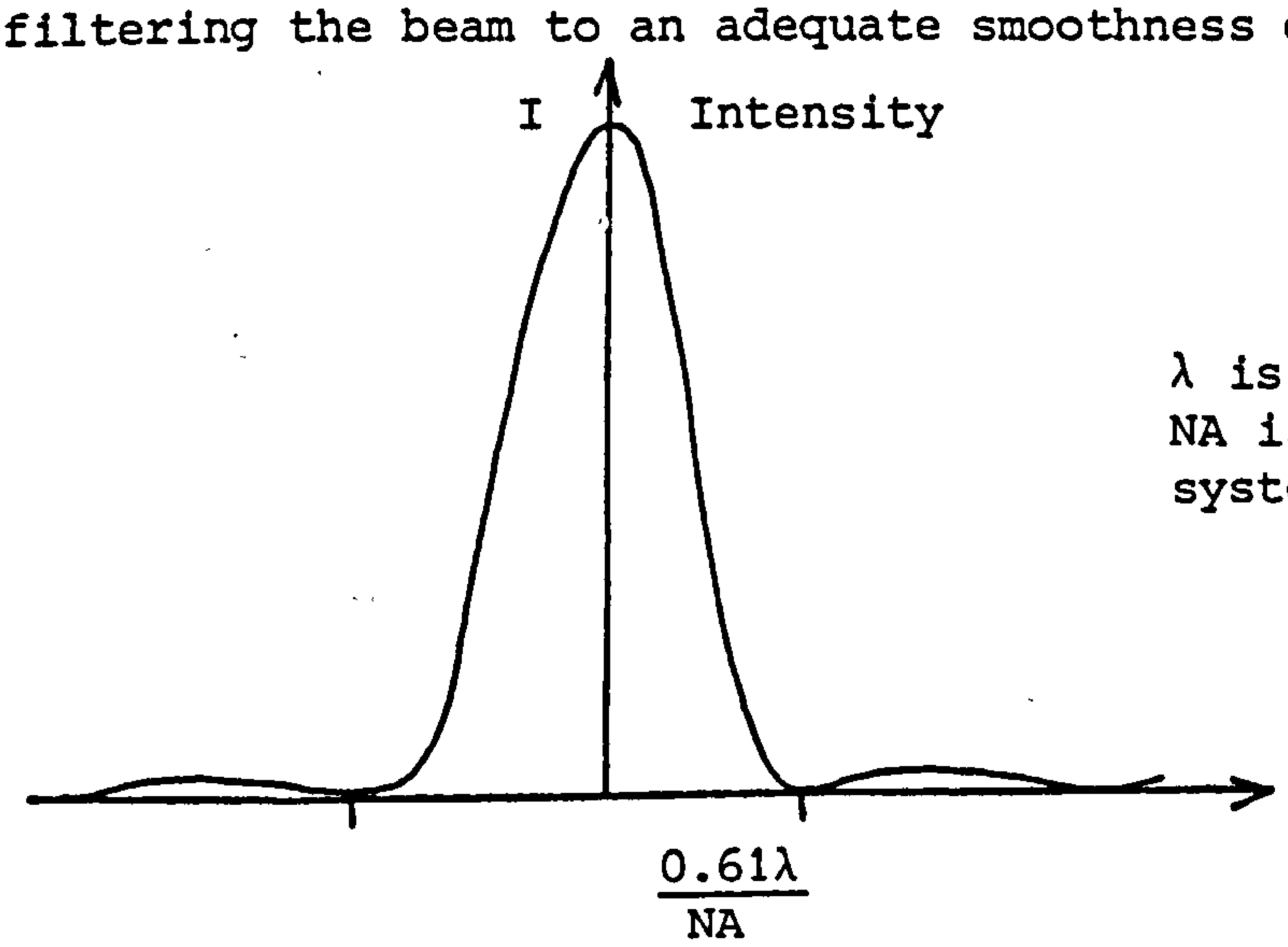

λ is wavelength of illuminating light.
NA is numerical aperture of optical system.

Fig. 16. Distribution of illumination in the focal plane diffraction pattern, showing the Airy Disc.

To provide a parallel beam of light of diameter 75 mm, a collimating lens of this diameter and about 1 m focal length is needed so that the light emerging from the pinhole fills the aperture of this lens. A suitable lens (f 12.6, focal length 945 mm) was obtained from Broadhurst Clarkson Co. The collimating lens is arranged so that its focal point coincides with that of the microscope objective.

The illuminating system is mounted on a free standing optical bench on two steel legs. These can be adjusted in height to allow the bench to be set horizontally at the correct height to illuminate the interferometer. For lateral movement, the legs have to be moved along the floor. The system is shown in Fig. 17.

3.2.4 The Recording System

The interferograms produced by the Mach-Zehnder interferometer are photographically recorded by a Pentax 35 mm camera. Because the standard aperture of the camera lens is not large enough to image the whole of the interferogram the camera lens is removed. A separate, corrected lens is used to collect the light emerging from the interferometer. The rays are focussed by this converging lens to a point in the plane of the camera shutter.

The camera shutter is attached to the camera by means of a bellows arrangement. This allows the camera to move horizontally, while leaving the shutter in position. The interferogram formed by the interferometer can thus be arranged to fill the negative plane of the camera. This is effectively the image plane of the lens, and the object plane is arranged to coincide with the centre of the gas jet. To prevent the film becoming fogged by any plasma radiation, an interference filter is placed in the recording system, between the lens and the shutter. The filter has a 3 nm

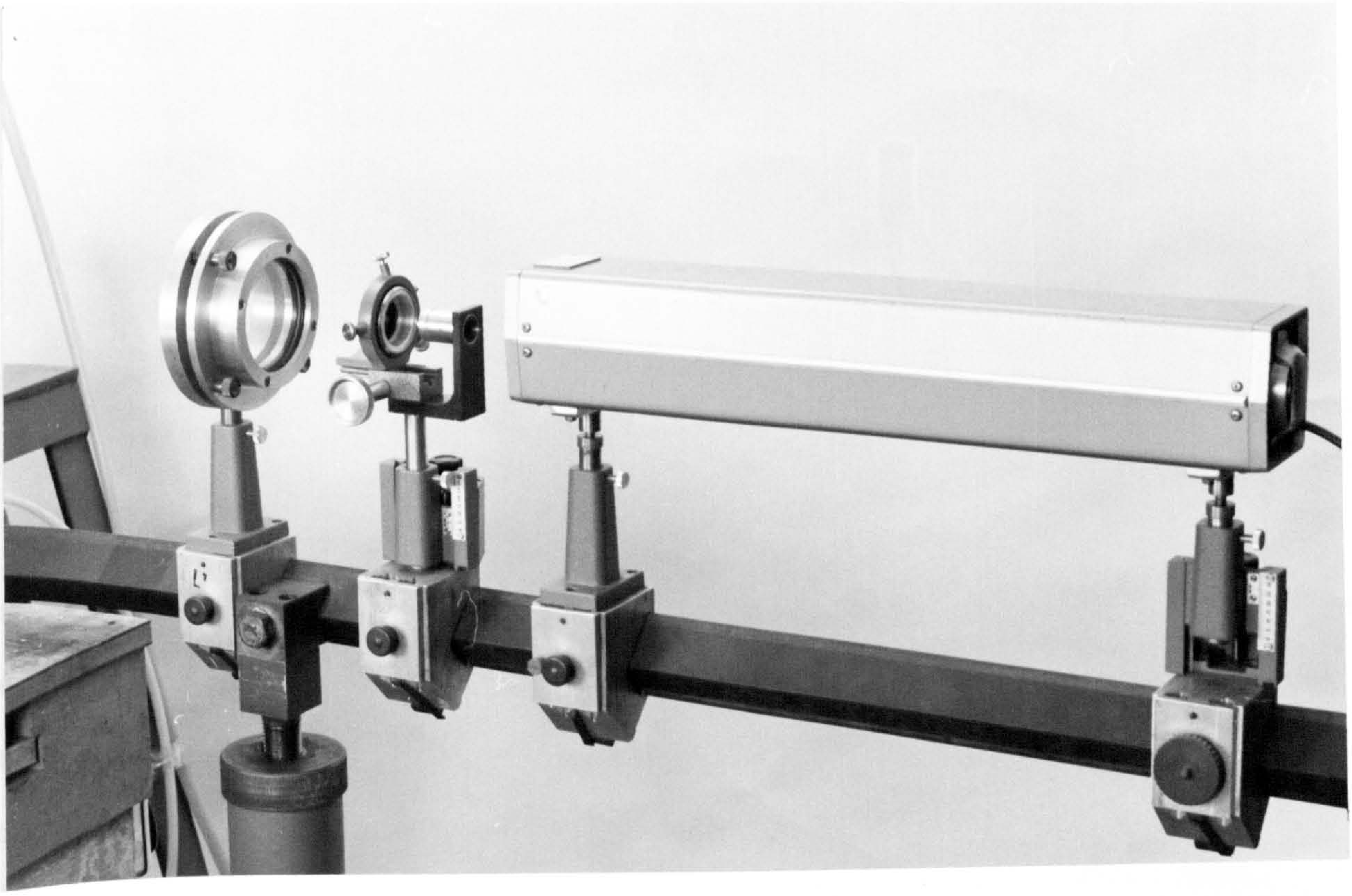

Fig. 17. Illuminating System.

bandpass about a 632.8 nm peak wavelength, the wavelength of the laser, and it allows 65% of the incident peak wavelength to pass.

The recording system is mounted on an optical bench, which is in its turn mounted on the same antivibration table as the interferometer and is shown in Fig. 18. This minimises any relative movement between the interferometer and the recording system.

3.3 ALIGNMENT OF THE SYSTEM

The system was initially set up to allow the laser beam to travel horizontally throughout. The optical components were removed from the free standing optical bench and the laser aligned so that the beam was parallel to the bench, and at the same height as the centres of the mirrors and beam splitters of the interferometer.

The beam splitter B_1 and the mirror M_1 were removed from their mounts. The position and tilt of the free standing optical bench was adjusted so that the laser beam passed through the centre of the beam splitter mount and hit the centre of the mirror mount. The mirror and beam splitter were then replaced in their mounts, with the beam splitter's reflecting surface towards the laser.

The beam splitters and mirrors were rotated about a horizontal axis until the laser beam travelled round the interferometer parallel to the base table. An engineer's square was used to check the alignment.

The optical components and camera were removed from the recording optical bench, and a screen set up on it. Slight rotational adjustments, about a vertical axis were made to the mirrors and the beam splitter B_2 until the two emerging beams were parallel to each other. This occurred when the

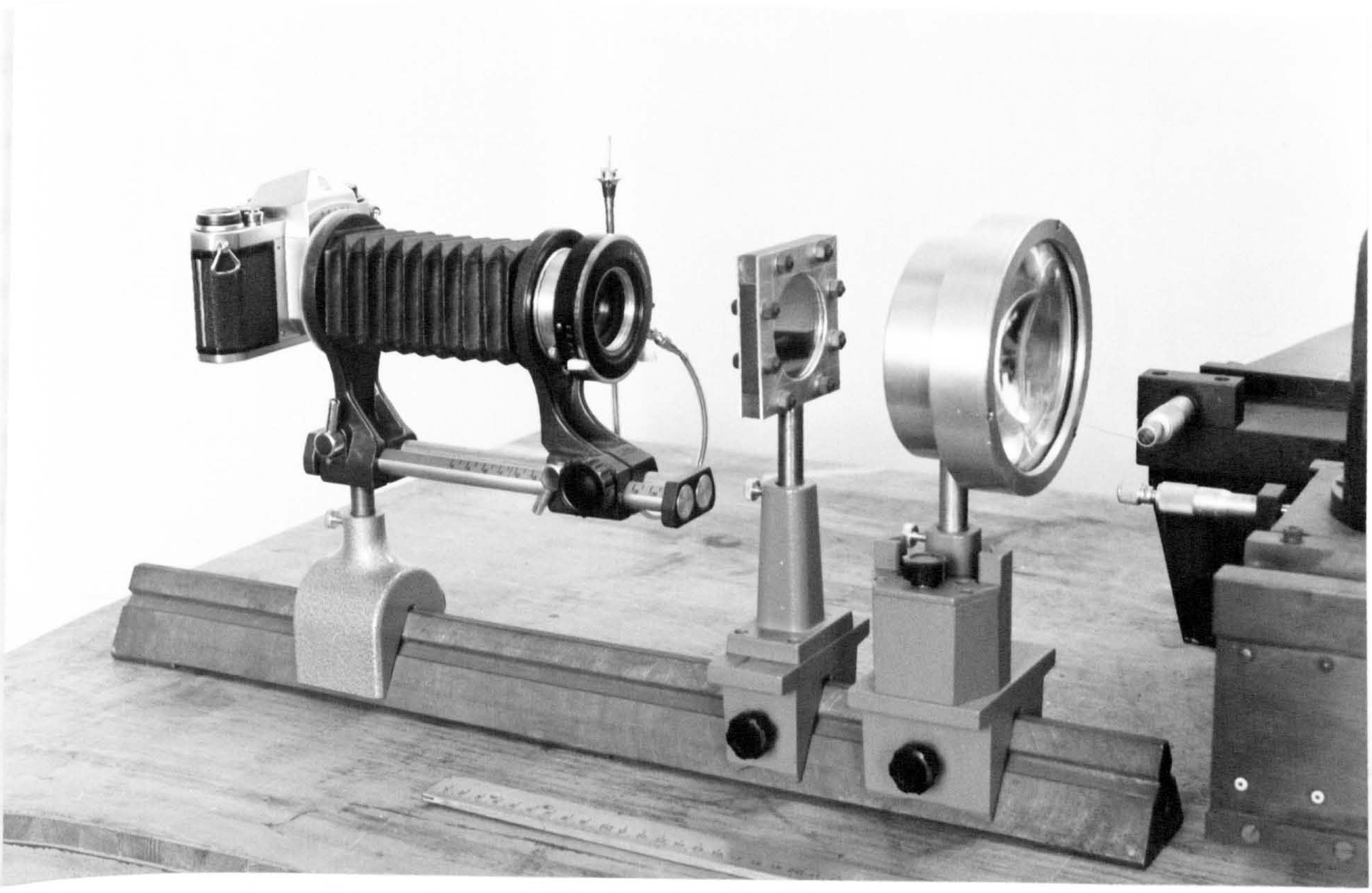

Fig. 18. Recording System.

two spots on the screen remained the same distance apart, regardless of the position of the screen on the optical bench. The screen was removed and the laser switched off.

The camera and converging field lens were set up on the recording and optical bench, so that the plane of the gas jet was imaged onto the negative plane of the camera. The laser was switched on again and a plane mirror was set up on the camera side of the field lens, with the reflecting face perpendicular to the optical bench and towards the lens. The lens was then adjusted accurately perpendicular to the laser beam by means of the Boy's Points method (29). The mirror was then removed.

The plane mirror was set up on the free standing optical bench, at the opposite end to the laser, and with the reflecting surface towards it. The collimating lens was placed in front of the mirror and adjusted perpendicular to the laser beam, again using Boy's Points. A screen was placed in front of the lens, and the point where the laser beam fell was marked. The microscope objective was placed in front of the laser, a distance from the collimation lens equal to the sum of the focal lengths of the two lenses. The objective was adjusted to allow the light to fall evenly about the spot marked on the screen.

A pinhole was placed at the common focal point of the two lenses and adjusted to give an even light intensity over the screen. This position was found by fine lateral and horizontal adjustment until the central spot in the diffraction pattern, the Airy Disc as shown in Fig. 16, expanded to engulf the dark rings.

The screen and the plane mirror were removed, and parallel interference fringes appeared at the exit of the interferometer. Slight adjustment of the mirrors M_1 and M_2 allowed the fringes to assume a favourable orientation, in this case about forty straight horizontal fringes.

The shutter of the camera was positioned so as to be at the focus of the field lens, and the aperture stopped down to filter out any spurious light. The torch head was placed in the object beam of the interferometer, parallel to the minor axis of the elliptical field of view. The torch nozzle was in the object plane of the camera and a calibration template was placed in the corresponding object plane of the reference beam.

3.4 RECORDING THE INTERFEROGRAMS

The interferograms were recorded on Kodak 2475 recording film, which is an extremely high speed, panchromatic film with extended red sensitivity. An exposure time of 1/500 seconds was used. The negatives were developed using the recommended Kodak developer and enlargements taken.

All possible care was taken that when the photographs were taken, there was as little turbulence as possible in the air of the laboratory, to avoid disturbing the gas jet.

The amount of fringe shift shown on the photographs was measured using a scale rule at each fringe along the jet. Photographs exhibiting the greatest symmetry were used. The readings thus obtained were used in the computation of radial and axial temperature distributions.

CHAPTER IV DERIVATIONS OF RADIAL TEMPERATURE PROFILES

4.1 INTRODUCTION

This chapter deals with the derivation of fringe shift data from photographed interferograms and the numerical analysis performed upon this data to transform it into radial temperature distribution data. The chapter covers the mathematical premise, the computer program and the effect of computational and experimental error.

4.2 THE DERIVATION OF FRINGE SHIFT DATA FROM PHOTOGRAPHS

Several photographs were taken of the interferogram produced by a jet with a particular set of input parameters. The one showing greatest axial symmetry and least fringe turbulence or distortion was chosen to provide data. Figs. 19 and 20 show sample fringe pattern photographs and both horizontal and vertical fringe orientations can be used. The horizontal fringes were chosen for analysis because, as can be seen from the photographs, the position where the fringe pattern becomes shifted is much more clearly defined on the horizontal fringes than on the vertical ones. The fringe shifts were measured at the position of each undisturbed fringe along the axis of the jet.

At each point of measurement along the axis of the jet, a base line was drawn on the photograph, across the fringe shift pattern joining the undisturbed portions of the edge of a fringe. The radial distance from the axis of the jet was measured at points where easily defined parts of the fringe shift pattern, i.e. the transition between dark and light fringes, intersected the base line. Thus by observing the number of fringe patterns intersecting the base line, a measurement of fringe shift with respect to position across the jet was made.

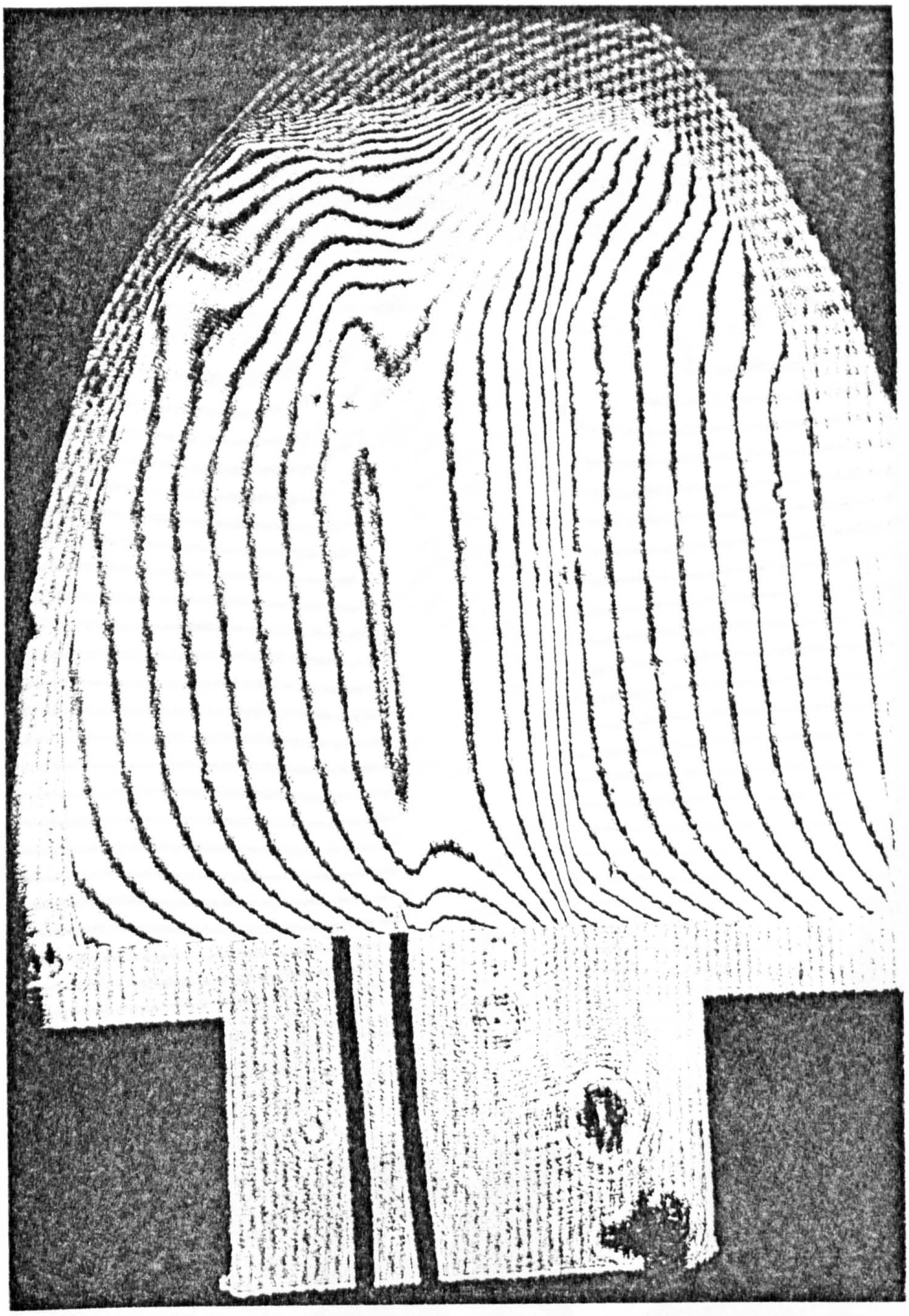

Fig. 19. Sample Photograph (Vertical Fringes).

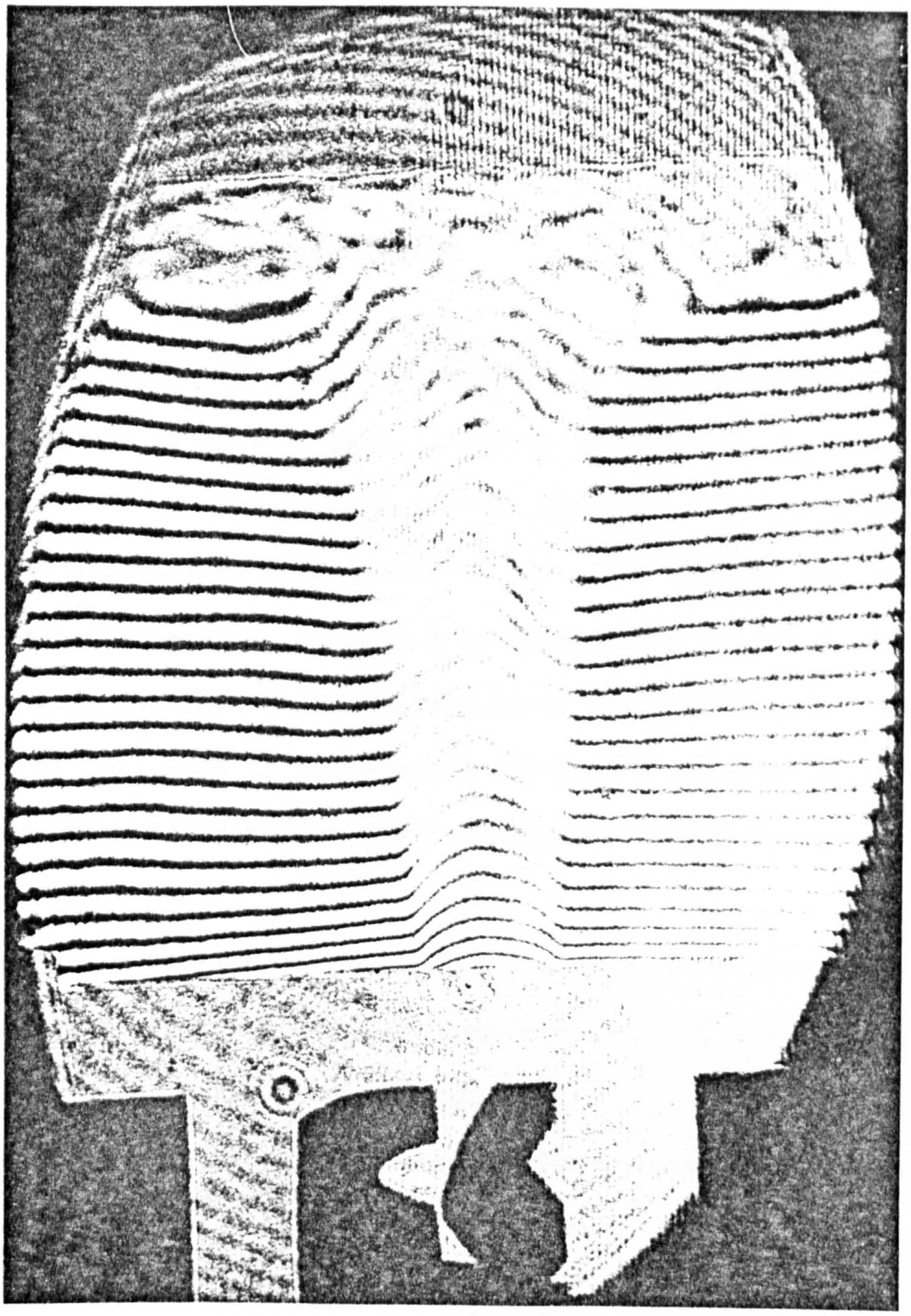

Fig. 20. Sample Photograph (Horizontal Fringes).

A graph of fringe shift against radial distance from the jet axis was plotted using measurements from both sides of the axis to ensure symmetry. A best fit smooth curve was drawn through the points by eye, and fringe shift values were taken off this curve at equally spaced radial points, from the axis ($r = 0$) to the point at which the fringe shift was zero ($r = a$). These values were fed into the computer for numerical analysis.

4.3 THE NUMERICAL TRANSFORMATION

The fringe shift patterns produced by the interferometer were formed by the change in optical path length as the beam of light in one arm of the interferometer passed through the hot gas jet. It can be seen from Fig. 21 that the geometrical path length of the light through the jet varies across the width of the jet. In such a situation, the fringe shift patterns result from collimated information along parallel chords. As it was the object of this work to investigate the RADIAL temperature of the jet, it was necessary to transpose these collimated measurements into radial data.

Considering a section of the jet of gas as shown in Fig. 21 the change in optical path length between the reference ray of laser light passing through air and a ray passing along a chord, is a result of the integration of the varying refractive index differences along that chord. This gives:

$$\text{change in optical path} = 2\int_0^{x_0} \left[(n - 1)_{air} - (n - 1)_{jet}(r)\right] dx \qquad 4.1$$

where $(n - 1)_{air}$ is the refractive index of the air in the reference beam, $(n - 1)_{jet}(r)$ is the refractive index of the jet at radius r, and $r^2 = x^2 + y^2$

From equation 2.15 :

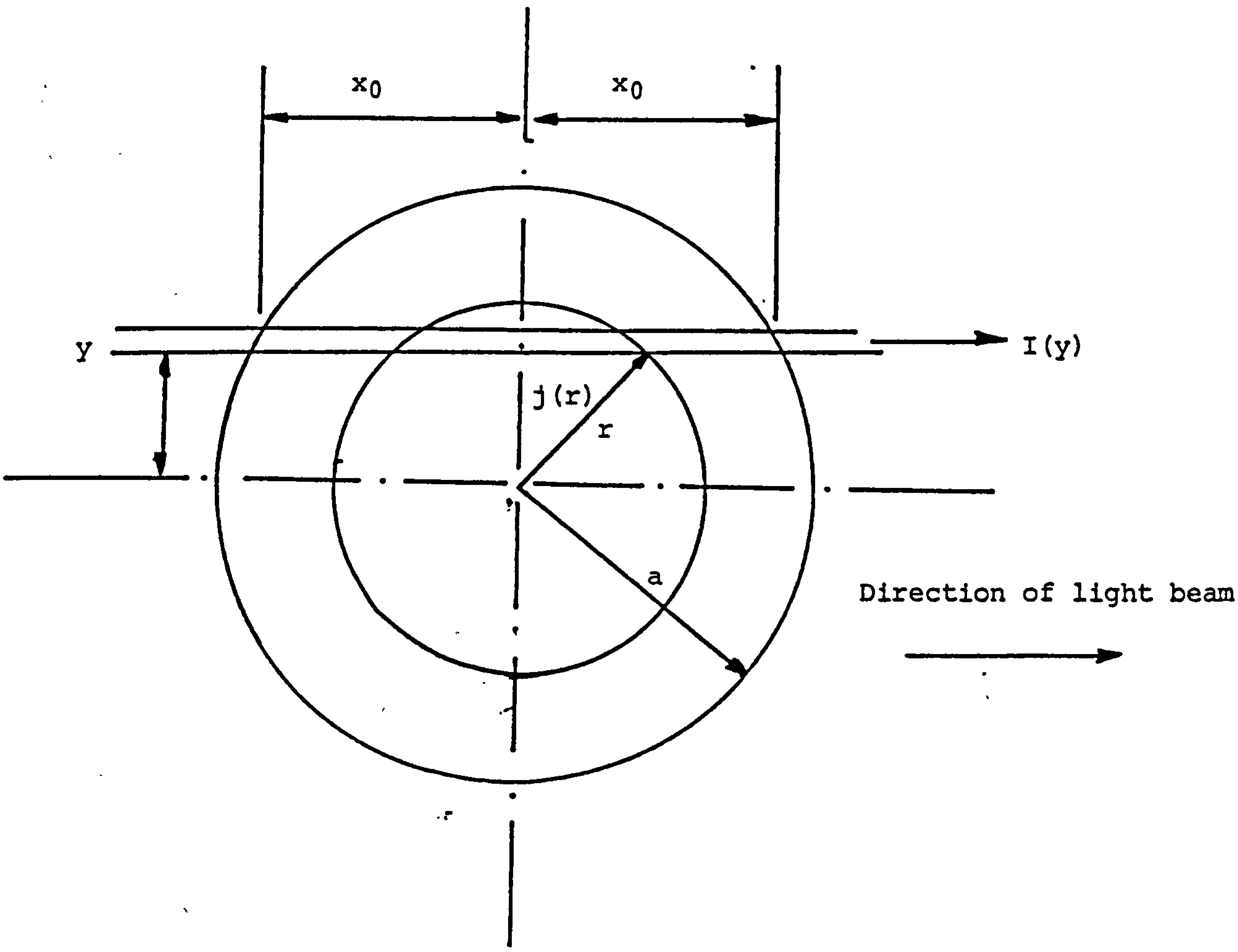

Fig. 21. Cross section of hot gas jet in light path showing a chord distance y from the axis which would give rise to a collimated fringe shift reading.

$$\text{change in optical path} = FS(y).\lambda \tag{4.2}$$

where FS(y) is the fringe shift at a distance y from the axis of the jet.

$$\therefore \quad FS(y).\lambda = 2\int_0^{x_0} \left[(n-1)_{air} - (n-1)_{jet}(r)\right] dx \tag{4.3}$$

This is an integral equation with the unknown radial refractive index inside the integral sign, related to the measured fringe shift data. By transforming the equation and a subsequent numerical analysis, values for the radial variations of refractive index can be found.

A possible method of solution is to transform the equation using the well known Abel inversion formula (26), to give an equation of the form

$$j(r) = -\frac{1}{\pi}\int_r^a \frac{dI(y)}{dy} \frac{1}{(y^2 - r^2)^{\frac{1}{2}}} dy \tag{4.4}$$

By assuming a suitable polynomial for I(y) between fixed points, the equation can be solved numerically for j(r) at different values of r (7,9,13). The method of solution used in this work is one developed by Harker (10) for analysis of current density in an electron beam, which is easily expanded to relate to refractive index in a hot gas. The derivation of this scheme is given in Appendix AI. The result can be expressed as

$$j(R) = \frac{N^{\frac{1}{2}}}{3\pi a} \sum_{Y=0}^{N-1} M_{RY} I(Y) \tag{4.5}$$

Here for convenience a change of variable has been made. The collimated function of I(Y) is obtained from I(y) at N equally spaced values of y2 in the range 0 to a^2, resulting in new variables $Y = Ny^2/a^2$ and $R = Nr^2/a^2$. In performing the integration I(Y) is approximated by parts of parabolas in each of the intervals $0 \leqslant Y < 2$, $2 \leqslant Y \leqslant 4$, ..., $N-2 \leqslant Y \leqslant N$.

M_{RY} is a matrix of coefficients, the derivation of which is detailed in Appendix AI.

Equation 4.5 is related to the case under study in that the radial function j(r) is the difference in the refractive index between the reference arm of the interferometer, $(n - 1)_{air}$, and at the radius r of the jet, $(n - 1)_{jet}(r)$. The collimated function, I(Y) is the change in optical path length, calculated from the fringe shift, at a distance Y from the axis of the jet,

$$j(r) = (n - 1)_{air} - (n - 1)_{jet}(r) \qquad 4.6$$

$$I(Y) = FS(Y) \qquad 4.7$$

A computer program was written to calculate the coefficient matrix, M_{RY}, to calculate the values of the function I(y), and extrapolate it to N values of Y, and to solve equation 4.5 for j(r). The value of the refractive index of the jet was then extracted using equation 4.6, and the temperature of the jet computed, using equation 2.7, $(n - 1) \propto 1/T$.

4.4 THE COMPUTER PROGRAM

The computer program processed the fringe shift data, converting it to change in optical path length. The optical path difference was then changed into radial change in refractive index, using Harker's numerical transformation, from which the radial temperature of the jet was calculated. A flow chart of the program is shown in Fig. 22.

The program consisted of a main program with four subprograms. It dealt with three sets of fringe data from a particular interferogram at one time and provided a print out of the fringe shift data, change in optical path

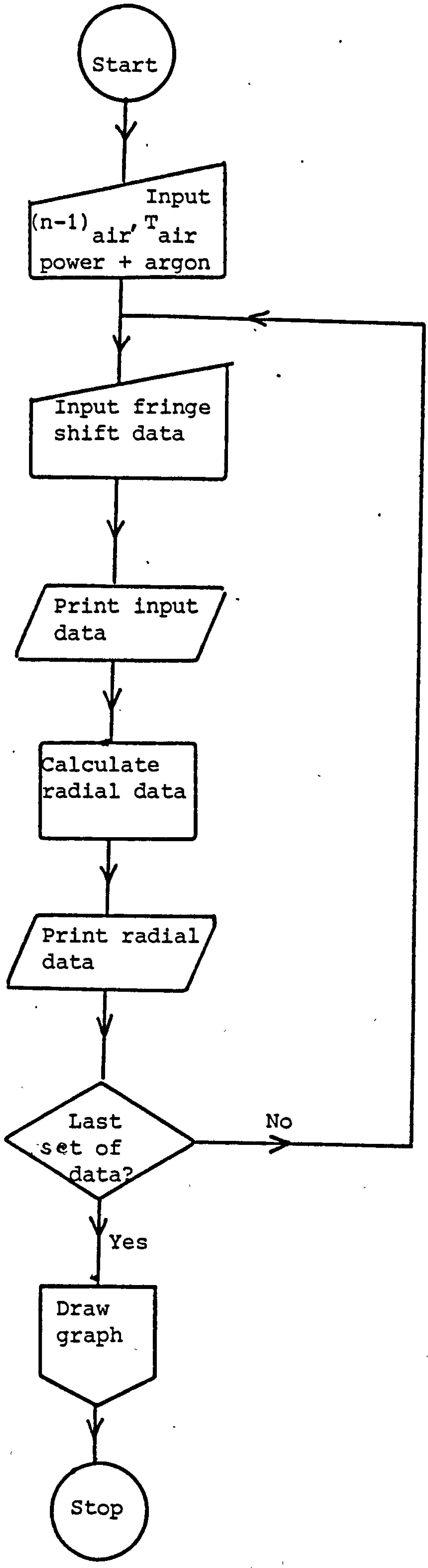

Fig. 22. Computer Program Flow Chart.

length, radial change in refractive index, radial refractive index of the jet, and radial temperature of the jet. It also plotted a graph of the three sets of radial temperature distributions. An example of this output is given with a listing of the computer program in Appendix AII.

The main program set the number of data points, N, used in the Harker transformation to be 40. It then accepted the input data of ambient temperature, the refractive index of the air corrected for ambient temperature and humidity, and the reference conditions of the gas jet (the power to the torch and the argon flow rate). For each set of fringe data, the program then called up the subprogram 'RUN' which read the fringe shift data and the overall jet radius at the axial distance under study.

The changes in optical path length values were calculated, using equation 4.2 and the values of the fringe shift and path length were printed out, together with the distance from the axis at which they occurred. The print out was headed with the position up the axis of the jet at which the readings were taken.

Subprogram 'RUN' then called up subprogram 'HARK' which assigned the chord position from the axis values, y, and the associated optical path length values I(y) to two arrays. In the numerical solution of the transformation as described in Appendix AI values of optical path length at previously undefined chord positions are used. In order to obtain the required values, subprogram 'HARK' called up the NAG library routine 'EO1ADF', a spline curve fitting routine. This fitted a cubic spline to a given set of data, in this case the y and I(y) arrays, and provided the value of the I(y) variable on the resulting curve at any required y axis value, giving two new arrays I(Y) and Y.

When the two new arrays had been set up, subprogram 'HARK' called up subprogram 'NUMB' which calculated the coefficient matrix M_{RY} required to solve equation 4.5. Control then returned to subprogram 'HARK' which evaluated the equation and calculated the new array of change in refractive index and hence radial temperature. The program control then returned to subprogram 'RUN' and the values of radial change in refractive index, radial refractive index and radial temperature were printed out. The control returned to the main program for the next set of results to be processed.

When all the data had been processed, a graph plotting subprogram 'PLOT32' was called up. This used the computer 'CGHOST' plotting library and produced a graph of the radial temperature distributions for all of the sets of data.

A listing of the computer program is given in Appendix AII.

4.5 THE EFFECT OF MEASUREMENT ERROR ON TEMPERATURE PROFILES

In any work dealing with physical measurements, it is inevitable that experimental errors occur. It is important to locate the source of these errors and investigate their effect upon the final results.

From equations 4.5, 4.6 and 4.7

$$n_{jet}(r) = n_{air} - \left[\frac{N^{\frac{1}{2}}}{3\pi a} \sum_{Y=0}^{N-1} M_{RY}\ FS(Y).\lambda\right] \tag{4.8}$$

The variables are the refractive index of the air, n_{air}, the radius of the jet, a, the number of data points used in the transformation, N, and the fringe shift data, FS(Y). Errors in these variables affect the calculated radial refractive index and hence the radial temperature of the jet.

As the readings from the photographs are scaled, the accuracy of the value of the overall radius of the jet is dependent on the scaling of the readings, as well as the precision to which they can be measured. The radius is averaged over values taken both sides of the axis, in an attempt to minimise any asymmetry, or misplacement of the position of the axis of the jet on the photograph.

The values of the fringe shift, FS, also depend on the accuracy of the measurements from the photograph of the interferogram, as well as the precision of the curve fitted through these points. In the majority of cases, it is possible to take measurements from the photographs to within 0.5 mm, which when scaled, is a value of 0.15 mm. However, when the fringes become less sharply defined, greater error is possible up to 1 mm before scaling.

The value of the refractive index in the reference arm of the interferometer depends on the wavelength of the illuminating light and ambient temperature, pressure and humidity. (n - 1) is calculated for the laser wavelength, using Cauchy's formula as quoted in Chapter 2, and then adjusted by the gas laws for atmospheric temperature and pressure, assuming an ideal gas. A correction is given by Lorenz (18) for humidity:

$$(n - 1)_{moist} = (n - 1)_{dry} + 0.000041\phi \qquad 4.9$$

where ϕ is the relative humidity. Thus errors in the measurement of ambient temperature, pressure and humidity of $\pm 2.5\%$, $\pm 0.25\%$ and $\pm 1\%$ respectively, give a cumulative error of $\pm 2\%$ in the value of the refractive index.

In order to investigate the effects of these sources of error on the final temperature distributions, a set of data was chosen and the changes in the final results observed for various input parameters.

To cover the errors introduced in transferring measurements from the photographs to the computer, a variation of ± 0.5 mm (0.15 mm when scaled) was introduced on the radius of the jet. Similarly, slightly different curves were drawn through the chosen set of fringe shift measurement points as shown in Fig. 23 and the readings from these different curves processed by computer.

To investigate the effect of the errors in the calculated value of the refractive index of air, the value of the refractive index was varied by $\pm 5\%$, a figure of the order introduced by the cumulative variations introduced by the measurement errors in temperature, pressure and humidity.

Another possible source of variation in the final result of radial temperature, is the number of data points chosen to be used in the solution of equation 4.5. The sample data was processed using values of N varying from 5 to 40.

The variations in the radial temperature distributions introduced by each of the above controlled errors taken singly were then calculated, and are shown in Figs. 24-27.

Fig. 24 shows the effect of varying the overall radius of the jet by ± 0.15 mm. At values of radius greater than 1.5 mm the three curves are superimposed, but between r = 1.5 and 0 mm they diverge, until, at the axis of the jet, there is a difference of 6000 K.

Fig. 25 shows the three temperature profiles for the three sets of data drawn through one set of data points shown in Fig. 23. This shows a variation of 750 K at the axis, and superimposed curves from radial values

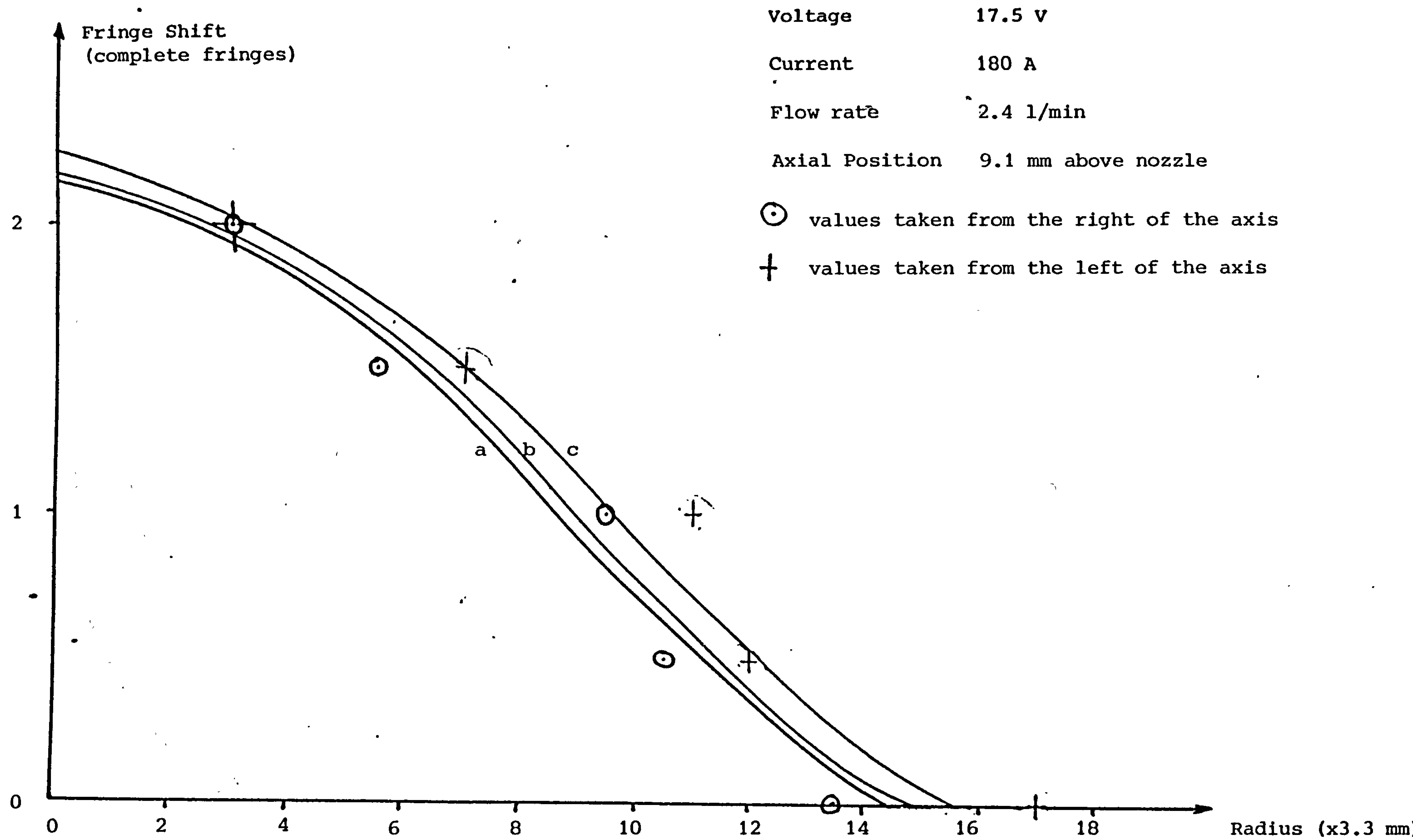

Fig. 23. Sample Fringe Shift Data - showing three possible curves drawn through the data points.

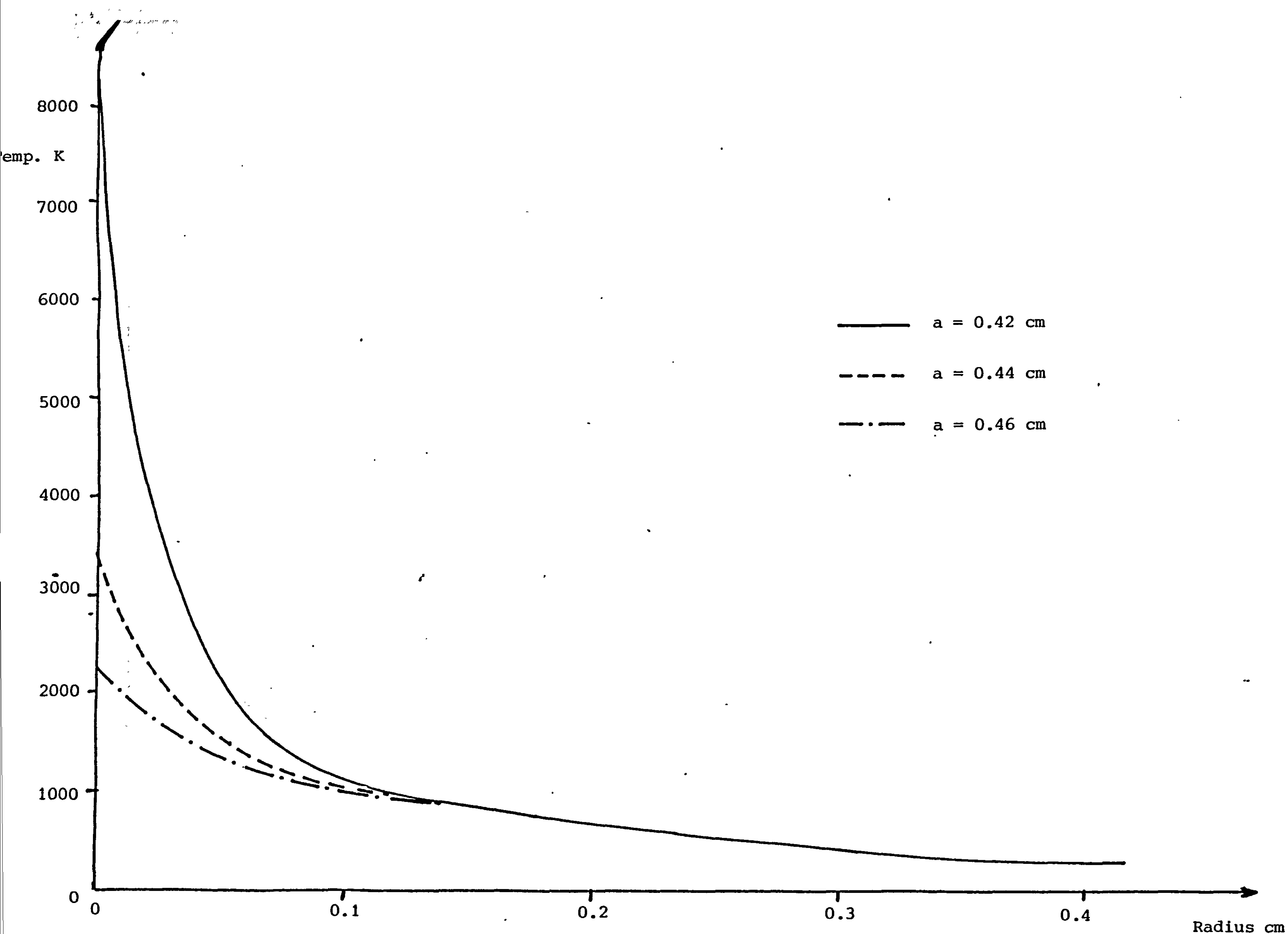

Fig. 24. Effect on radial temperature of varying overall radius of jet, a.

Fig. 25. Effect on radial temperature of varying curves through a set of data points.

of approximately 0.5 cm.

Fig. 26 shows the effect on temperature profiles of varying the value taken for the refractive index of air. The graph shows three complete curves, and one which is incomplete. The three complete curves show an axial temperature variation of 4750 K for a change in refractive index of 0.00004. The incomplete curve was the result of making n_{air} 1.00026. This transformed to give an axial temperature of -6000 K. By studying equation 4.8 it can be seen that if the refractive index of air is less than the result of the Harker transformation, then a negative value will be found for $(n - 1)_{jet}$, and hence the temperature.

Fig. 27 shows the effect of varying the number of points used in the Harker transformation. A variation of 2000 K axial temperature is the consequence of varying the value of N between 5 and 40.

The overall effect of these results will be discussed in Chapter 6.

Fig. 26. Effect on radial temperature of varying refractive index of air.

Fig. 27. Effect on radial temperature of varying N, number of points used in Harker Transformation.

CHAPTER V EXPERIMENTAL TEMPERATURE PROFILES

5.1 INTRODUCTION

This chapter contains descriptions of the temperature profiles derived from the photographs of interferometric fringe shift patterns. The first section deals with the radial temperature distributions. These distributions are collated and presented in the second section as axial temperature distributions.

To study the effect of input conditions to the torch on the temperature of the jet, the power to the torch was kept constant as the argon flow rate was varied, and the argon flow rate was kept constant while the power to the torch was varied.

Data is presented for a constant power of 1.4 kW and argon flow rates of 1.4, 3.2 and 4.3 l/min, and for a constant flow rate of 2.4 l/min and powers of 1.3, 2.5 and 3 kW.

The temperature of the jet was measured with a thermocouple and the results compared with those obtained by interferometric means.

5.2 RADIAL TEMPERATURE PROFILES

Radial temperature profiles were produced directly by the computer program, which provided both a numerical output of data and a graphical display. Appendix AV contains a selection of the radial temperature distribution curves.

Figs. 28 to 33 show sample fringe shift data together with the corresponding radial temperature distributions for each of the six sets of jet input

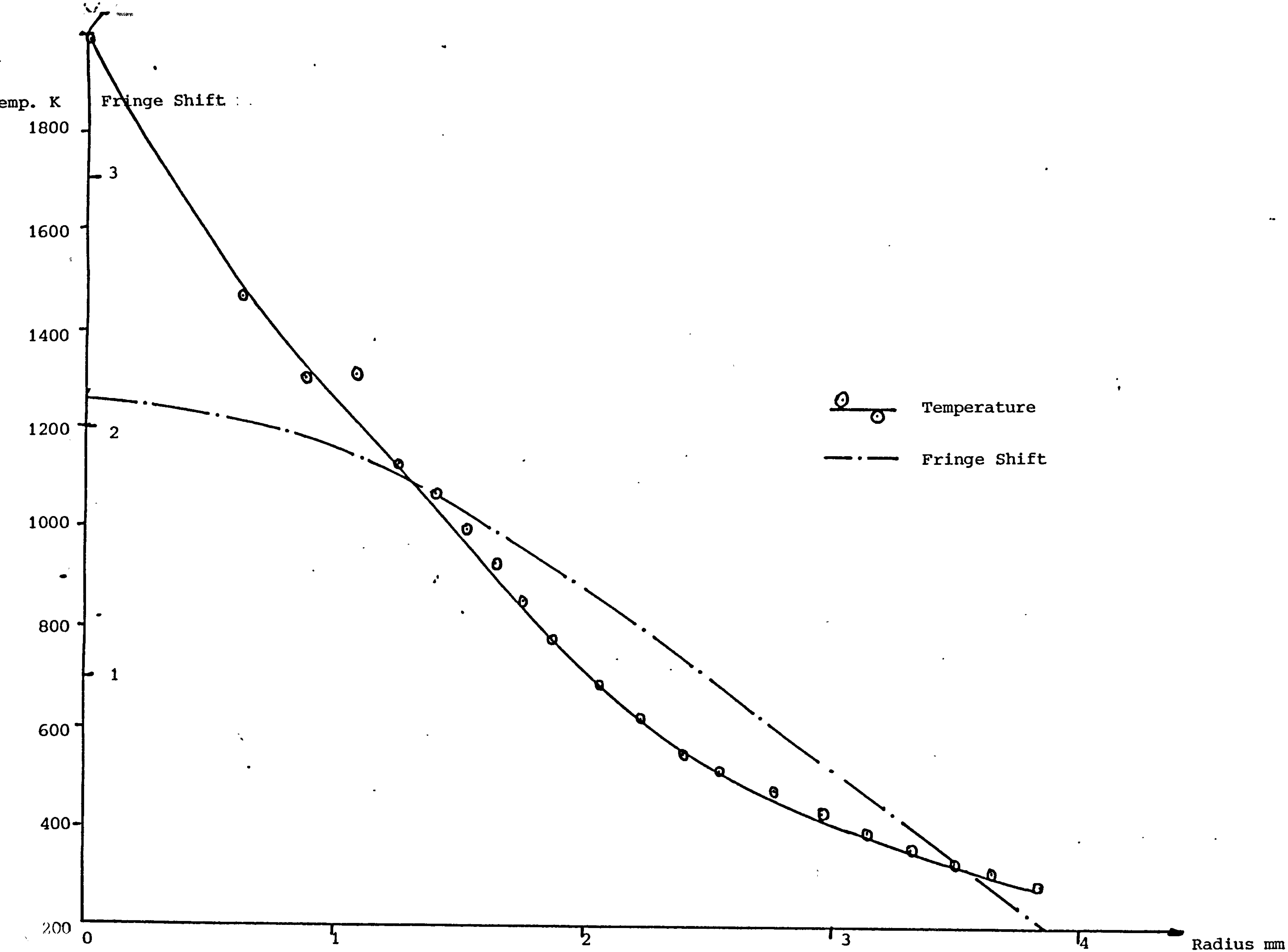

Fig. 28. Radial temperature and fringe shift for power 1.4 kW and flow rate 1.4 l/min and at an axial position of 7.7 mm.

Fig. 29. Radial temperature and fringe shift for power 1.4 kW and flow rate 3.2 l/min and at an axial position of 14.4 mm.

Fig. 30. Radial temperature and fringe shift for power 1.4 kW and flow rate 4.3 l/min and at an axial position of 10 mm.

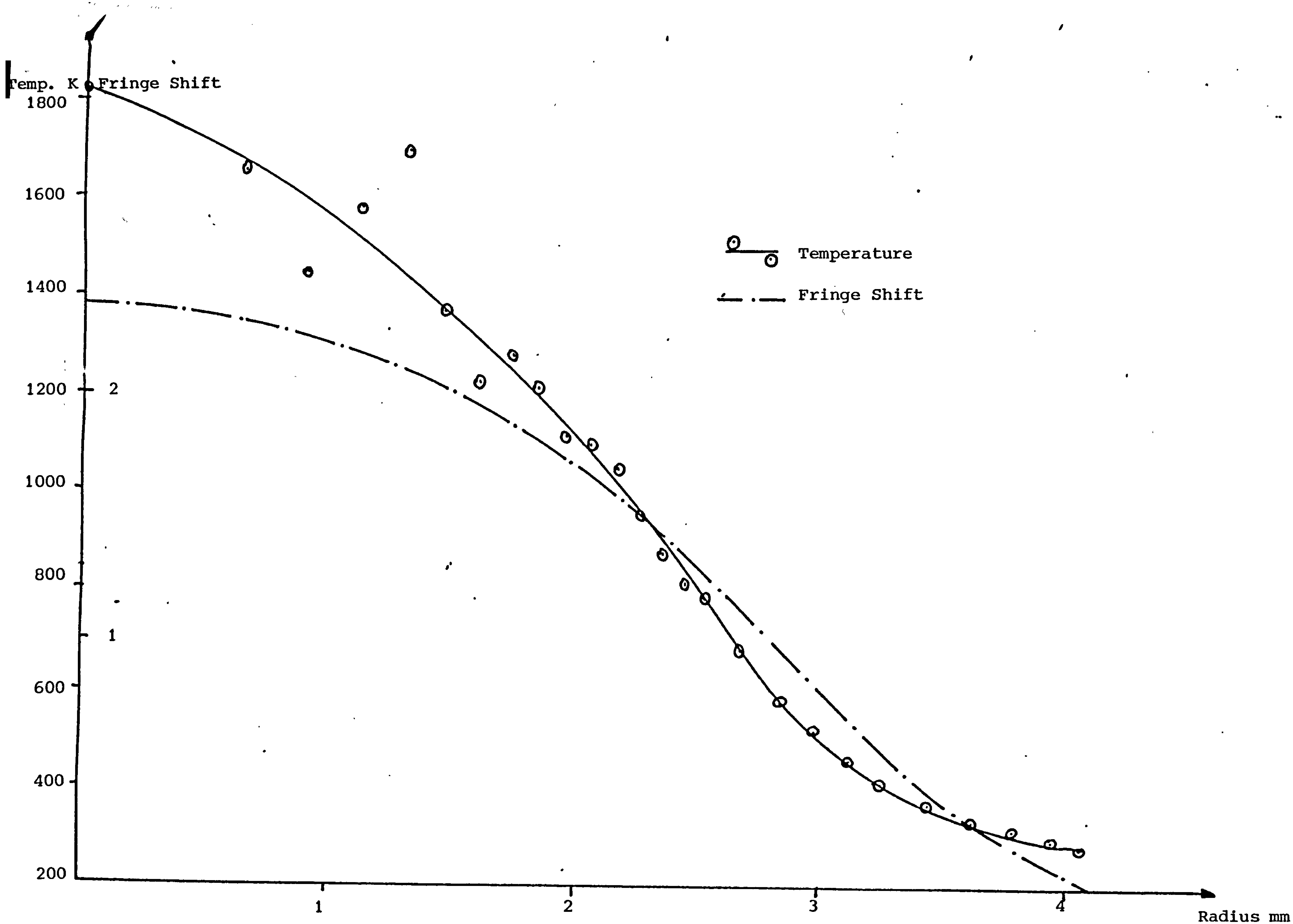

Fig. 31. Radial temperature and fringe shift for power 1.3 kW and flow rate 2.4 l/min and at an axial position of 10.2 mm.

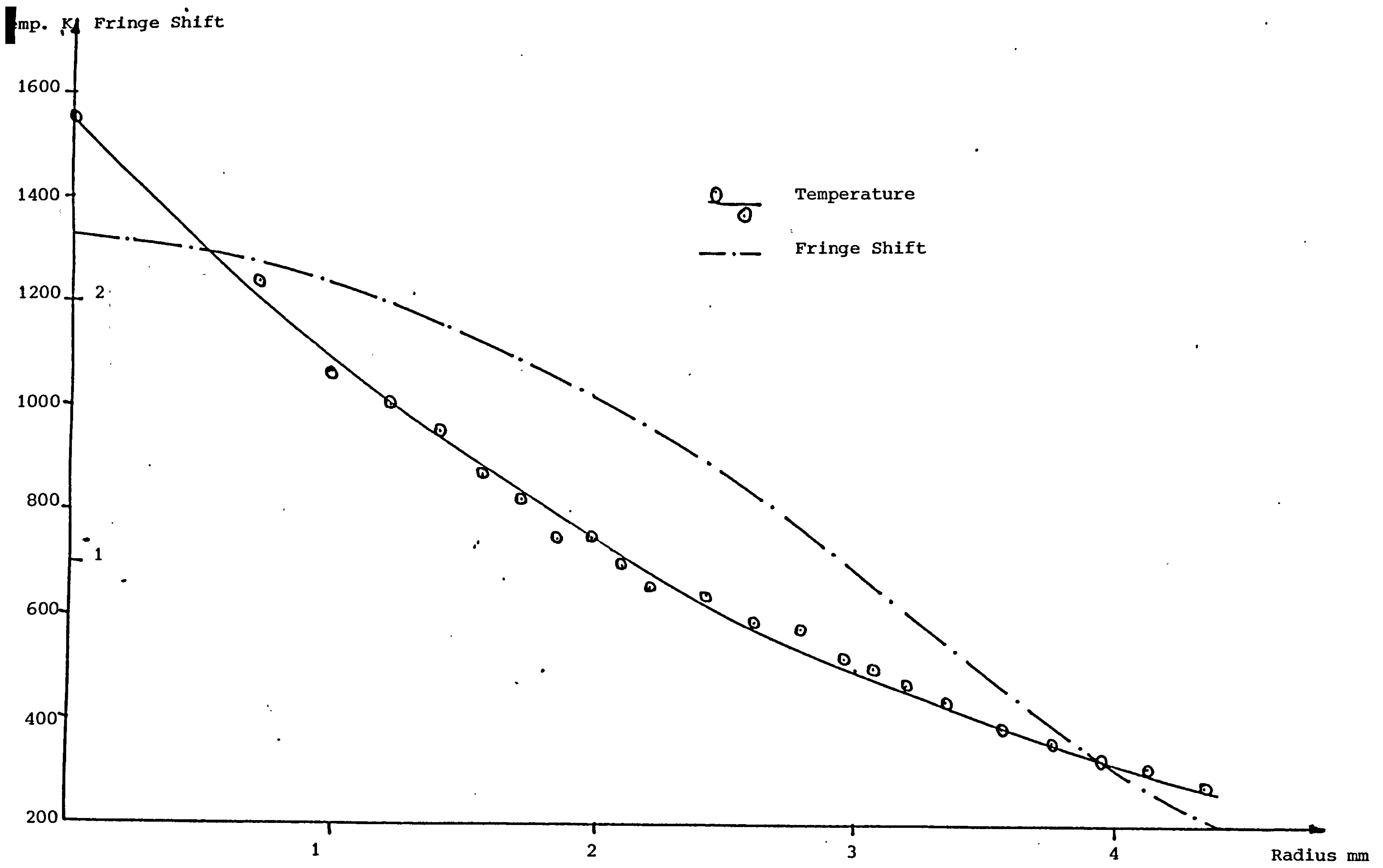

Fig. 32. Radial temperature and fringe shift for power 2.5 kW and flow rate 2.4 l/min and at an axial position of 14.5 mm.

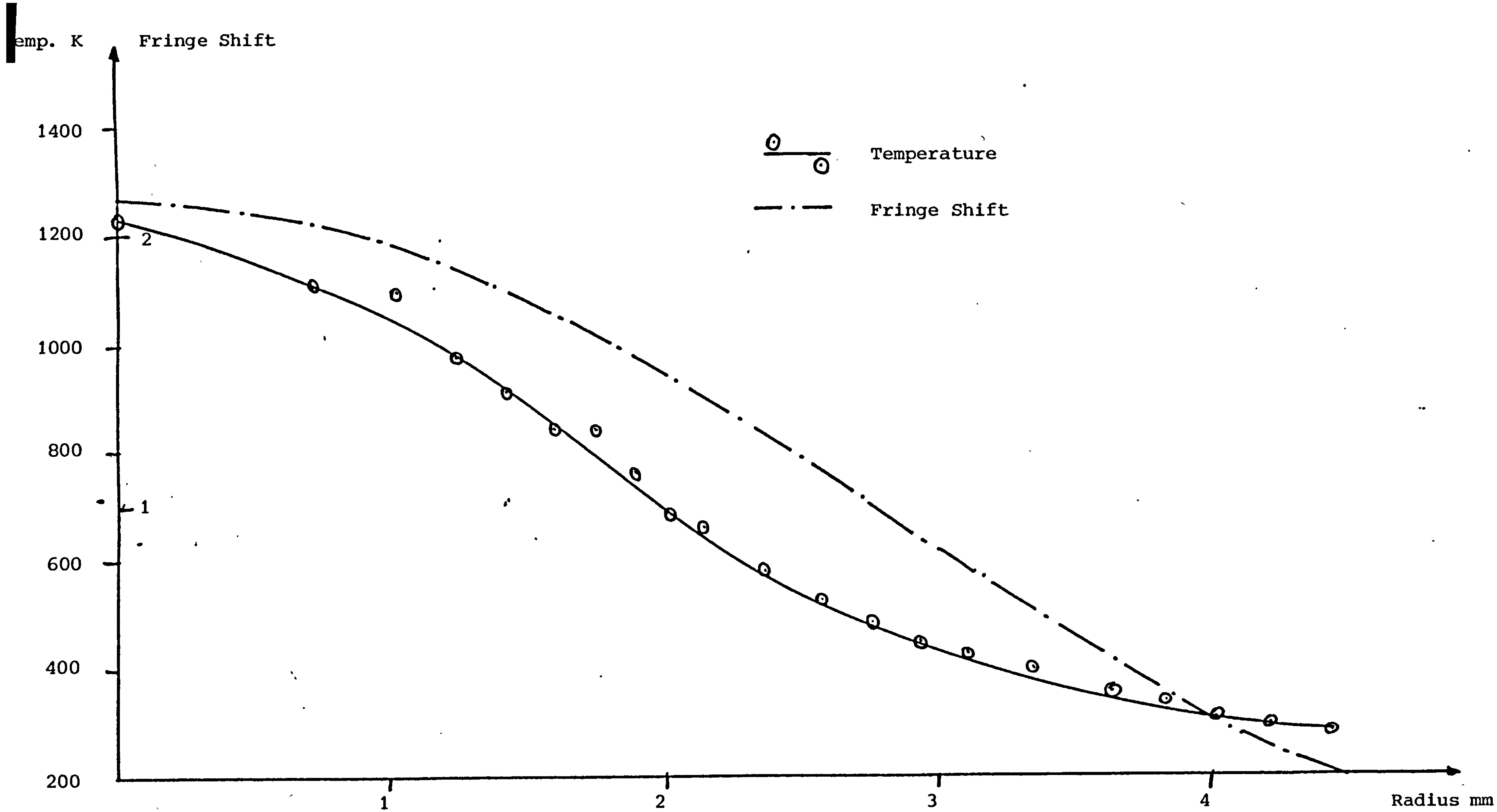

Fig. 33. Radial fringe shift and temperature profile for power 3 kW and flow rate 2.4 l/min and at an axial position of 9.1 mm.

conditions. With argon flow rates above 5 l/min or power input to the torch above 3 kW, the fringes were too turbulent to produce clear pictures at the fastest shutter speed of which the camera equipment was capable, that is 1/500 sec. Figs. 28 to 30 cover constant power of 1.4 kW with flow rates of 1.4, 3.2 and 4.3 l/min and figs. 31 to 33 cover constant flow rate of 2.4 l/min with powers of 1.3, 2.5 and 3 kW. Each sample was taken from approximately 10 mm above the jet nozzle. These graphs show the temperature on the jet axis varies between approximately 1000 K and 2000 K, while decreasing to approximately 280 K at the outer boundary of the jet.

Further study of the figures in Appendix AV show that the axial temperature can range from 800 K to 9000 K, depending on the axial position and the input conditions to the torch. Some of these figures also show very negative values of temperature - up to -20000 K. Obviously these are physically impossible results, and they will be discussed further in the next chapter.

Deviations from a smooth curve in the radial temperature profiles may be observed, in particular in Fig. 31, though it also occurs to a lesser extent in Fig. 28. It is noted in these two figures that there is a sharp rise in temperature in the final data point, that is on the axis of the jet. This phenomenon will be discussed further in the next chapter.

5.3 AXIAL TEMPERATURE PROFILES

For each set of input parameters to the jet, temperature profiles were plotted along the jet axis. Due to the phenomenon of suprisingly sharp increases in temperature actually on the axis indicated in Fig. 27 and in the error analysis of the previous chapter, the points comprising these profiles were very scattered. So temperature profiles parallel to the axis of the jet but located at a distance of 0.25 a from the axis, where a is the maximum radius of the jet at the level under consideration, were also plotted.

Figs. 34 to 39 show the axial distributions. Figs. 34 to 36 cover constant power of 1.4 kW with varying flow rates of 1.4, 3.2 and 4.3 l/min, and Figs. 37 to 39 cover constant flow rates of 2.4 l/min and varying powers of 1.3, 2.5 and 3 kW. Thermocouple readings of the jet temperature also appear on these graphs.

As would be expected, the axial temperature was highest close to the source of the jet, the torch, between 5000 K and 9000 K on axis, depending on the torch input parameters, tapering off to between 700 K and 1500 K around 20 mm above the torch orifice. Beyond 20 to 25 mm above the orifice, the interferomgrams were too turbulent to extract valid data.

In all the figures, it can be seen that the temperature distributions from the on-axis positions are very scattered, while those taken 0.25 a from the axis form a more continuous curve. Best fit curves were fitted as well as could be achieved by eye.

For a power of 1.3 kW and flow rate of 2.4 l/min, in Fig. 37, no valid results were gained past 12 mm above the nozzle. Beyond this position all the temperatures were negative between the axis and up to half the radius.

For a power of 3 kW and a flow rate of 2.4 l/min, Fig. 39, there appeared to be no appreciable variation in temperature along the length of the jet between 2.5 mm and 25 mm above the torch orifice. There was also little change between the two curves for r = 0 and r = 0.25 a.

At temperatures above about 1200 K the thermocouples melted, so it was

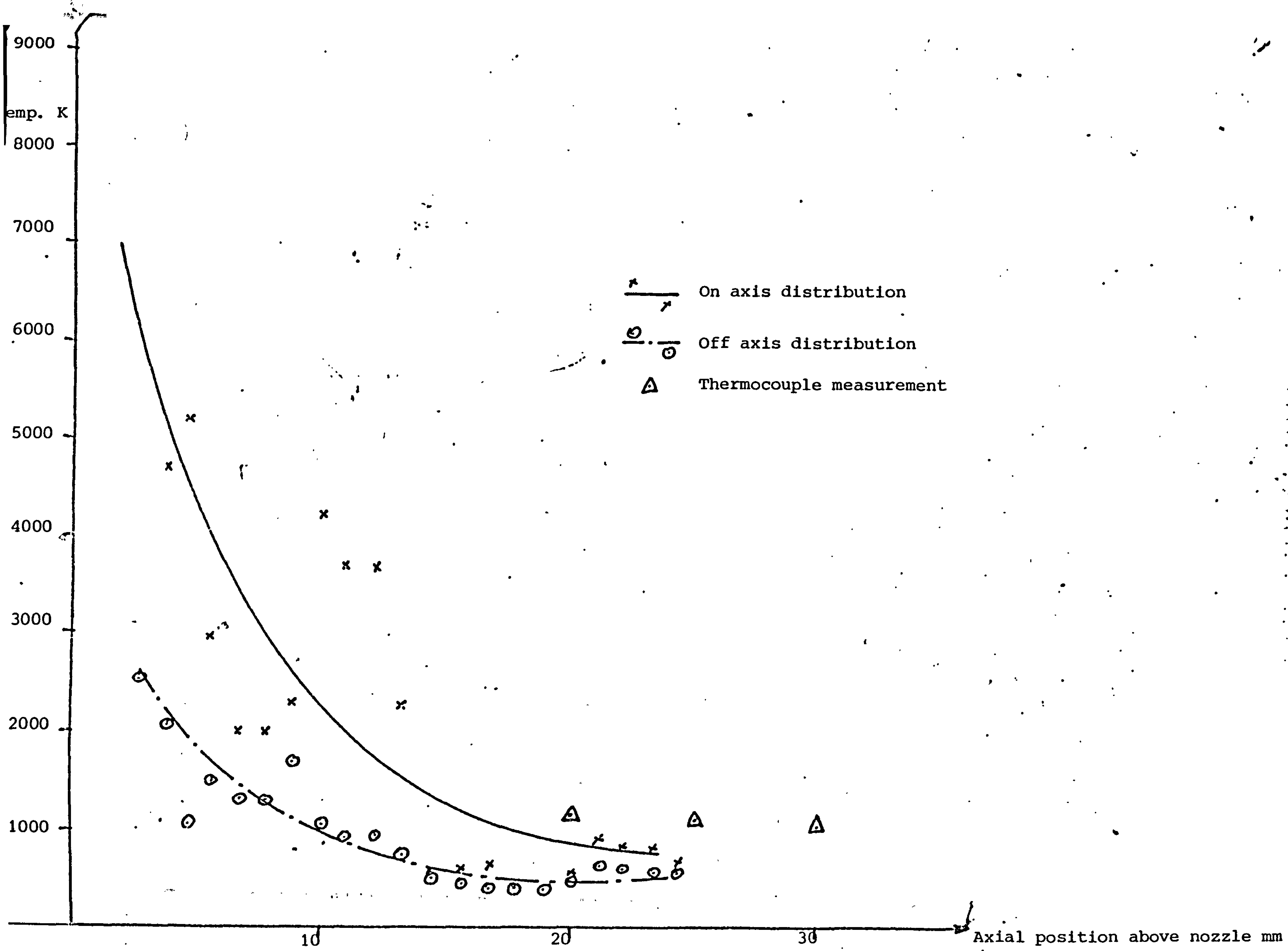

Fig. 34. Axial temperature distribution for power 1.4 kW and flow rate 1.4 l/min.

Fig. 35. Axial temperature distribution for power 1.4 kW and flow rate 3.2 l/min.

Fig. 36. Axial temperature distribution for power 1.4 kW and flow rate 4.3 l/min.

Fig. 37. Axial temperature distribution for 1.3 kW power and 2.4 l/min flow rate.

Fig. 38 Axial temperature distribution for 2.5 kW power and 2.4 l/min flow rate.

Fig. 39. Axial temperature distribution for 3 kW and 2.4 l/min.

only possible to take thermocouple readings in the top third of the jet, nearest the cool rotating surface, where it was impossible to take interferometric readings. However, by extrapolation, the two sets of readings appear to be of a similar order.

CHAPTER VI DISCUSSION AND CONCLUSION

6.1 INTRODUCTION

In this chapter the results presented in the previous chapter are discussed in respect of radial and axial temperature distributions. Correlation between temperatures and torch input conditions are sought. The accuracy of the results is considered in the context of the sources of error presented in Chapter 4 and any other possible sources.

6.2 RADIAL TEMPERATURE DISTRIBUTIONS

Some anomalous results for the radial temperature distribution were noted in the previous chapter. These were departures of the transformed data from a smooth curve, sharp temperature rises on the axis of the jet and large negative temperatures.

Negative temperatures and sharp temperature rises on the axis of the jet derive from the same cause. Equation 4.8 can be written

$$(n - 1)_{jet} = (n - 1)_{air} - \frac{N^{\frac{1}{2}}}{3\pi a} \sum_{Y=0}^{N-1} M_{RY}\, I(Y)$$

In Fig. 40 the second term on the right hand side of this equation, as determined from the numerical manipulation of the experimental fringe shift data, is plotted. A horizontal line can be superimposed on this plot to represent the value of $(n - 1)_{air}$. If, due to errors in the value ascribed to $(n - 1)_{air}$ and in the second computed term, these two plots overlap then, near the axis $(n - 1)_{jet}$ will take negative values. Since the computer uses the Gladstone-Dale formula, equation 2.6,

$$(n - 1)_{jet} = \frac{\text{const}}{T}$$

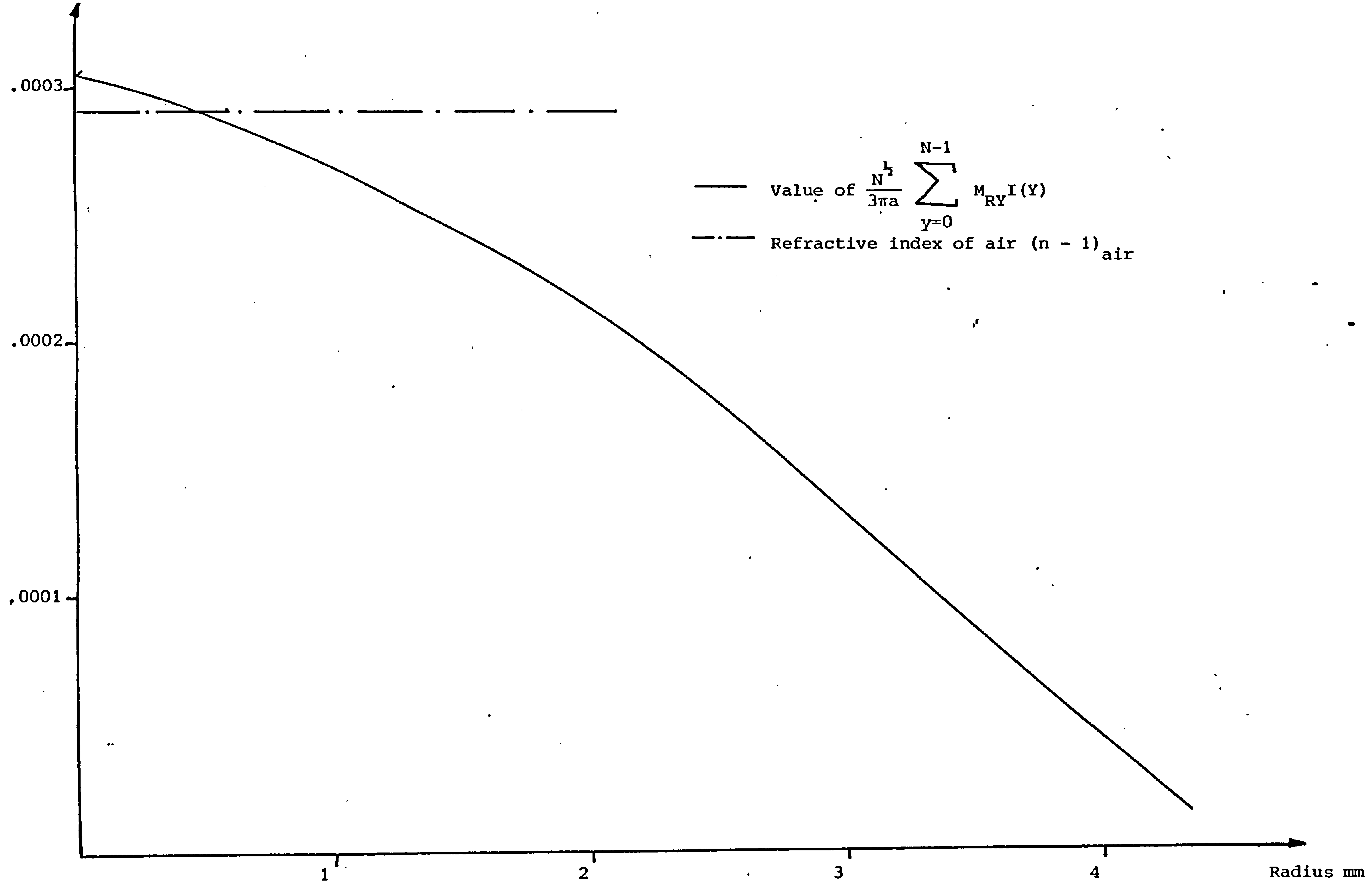

Fig. 40. Refractive index difference against radius, with refractive index of air superimposed.

negative temperatures are produced.

Alternatively, if the two lines do not overlap but come close together near the axis, i.e. $(n - 1)_{jet}$ very small, the calculated temperatures will become very large. It is therefore considered that no confidence can be placed in temperature values close to the axis, out to some radial value of less than 0.25 of the full radius.

As the numerical transformation of the data, the matrix of coefficients, M_{RY}, and the refractive index of air remains the same, regardless of the input data, it is possible that the shape of the input data curve is the cause of the instabilities in the result.

The experimentally determined fringe shift data is so scattered that a variety of shapes of curves could be drawn. To investigate the effect of this shape of curve of the fringe shift data on the final temperature values, a set of dummy data was fed to the computer, with the same typical values of maximum radius and fringe shift, but different shapes, as shown in Fig. 41. The three curves are representative of three of the possible shapes of curve which could be fitted through the fringe shift values from the photographs of the interferograms. Curve A approximates to a parabolic shape curve and curve B is approximately gaussian. The slope of both these curves tends to zero at the axis. Curve C has a relatively constant slope along its length. In this work, curves of type B were fitted through the data as much as possible. It was felt that the change in refractive index, along a chord, which is what these curves represent, would be unlikely to display discontinuities at the axis, hence the tendency to zero gradient at this point.

Fig. 42 shows the respective "temperature" distributions. Curve A transforms to a radial distribution which remains relatively constant at

Fig. 41. Typical fringe shift data for analysis of the numerical transformation.

Fig. 42. "Temperature" profiles from the dummy fringe shift data in Fig. 41.

approximately 650 K for three quarters of the radius from the axis, and then drops off to the ambient temperature sharply at the outer edge of the jet.

Curve B shows peaks of temperature on axis, and at 1.5 mm from the axis, but the temperature decays approximately exponentially towards the ambient at the outer edge of the jet. Curve C is discontinued between the axis and 0.64 mm from the axis, as the temperature value is negative. However, if the curve were to be extended by extrapolation, it would seem to tend towards infinity, or possibly intersect the axis at some point above 1600 K, as indicated by the broken line.

These curves would seem to support the premise to fit gaussian type curves through the data obtained from the photographs, and that flat curves lead to sharp rises of temperature on axis. Temperature curves with a double peak were found by Czernichowski in his paper (9).

By considering the data presented in the previous chapter, some correlation between actual input fringe shift data and the final radial temperature distribution is sought. Figs. 28, 30 and 32 have very similar shaped curves of fringe shift data and the temperature data curves also follow each other closely, from about 1.2 mm from the axis towards the edge of the jet. Here they separate, Fig. 30 having the lowest axial temperature, though the smoothest curve, and Fig. 28 having the highest axial temperature, though the curve would seem to indicate a very sharp discontinuity in temperature on the axis of the jet. These results would support the premise that no confidence could be placed in readings on the axis, but off axis, similar shaped fringe data curves produce similar shaped temperature curves. However, the on- and off- axis temperatures on these curves correlate closely to the maximum radius of the jet. Fig. 30 has the lowest axial temperature and the greatest radius, while Fig. 28 has the highest axial temperature and the lowest maximum radius value.

In the cases where there is a relatively small jet radius compared with the maximum amount of fringe shift, and hence portions of the fringe shift curve have high gradients, e.g. Fig. 31, then an oscillatory departure from a smooth curve is exhibited. It is not clear whether more data points would smooth out this departure, or accentuate it. Where, however, the jet radius is large in comparison with the fringe shift and the gradient is gradual as in Fig. 30, the temperature data tends to be smooth.

Thus, using these conclusions, it would seem to indicate that gaussian type curves should be fitted through the fringe shift data derived from the photographs, and care should be taken to avoid fitting curves exhibiting high fringe shift with small radius.

However, even using these criteria as a basis, there is still the difficulty of fitting the best true fit line through the available data points. As discussed in Chapter 4, the measurements of the fringe shift across the chosen base line were taken where easily defined sections of the fringe pattern crossed this line, and averaged for both sides of the axis of the jet. It was assumed that these easily defined sections, i.e. the demarcation between light and dark bands, occurred evenly across the intensity spectrum. This was not, however, necessarily the case. Fig. 43 shows the intensity vs phase of an interference pattern. If a line is drawn parallel to the phase axis, representing the intensity at which the demarcation between light and dark fringes occurs on the photographs, it can be seen, from such lines, a, b and c, that the phase from one side to another of a fringe is not necessarily π, as assumed. Of course, the phase between, say, the demarcation between light and dark and the next demarcation between light and dark, is 2π.

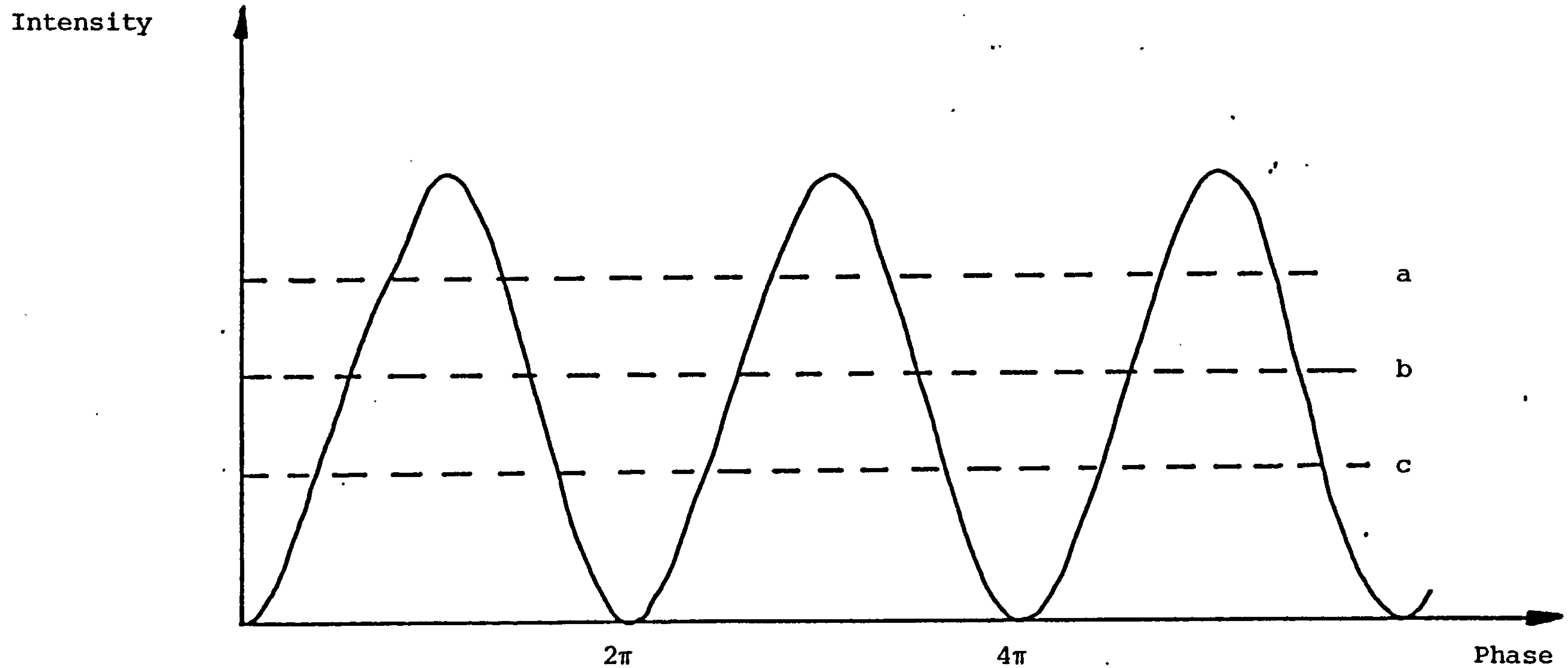

Fig. 43. Light intensity vs. phase for interference fringes showing possible positions of demarcation between light and dark fringes.

Thus, it would seem that the only values that can be said to be accurate on the fringe shift vs distance from the axis data are those at whole values of fringe shift. However, this would give, on average, only two data points on either side of the axis through which to attempt to fit a smooth curve, so intermediate points had to be estimated at half fringe separations.

In Chapter 4, different curves were fitted through a sample set of data. The variations in the final temperature on the axis was 750 K in 4000 K, while at 0.25 a, where a is the maximum radius of the jet, it was approximately 200 K in 1000 K, about 20% in both cases. However an error in the measured radius of the jet from the photograph of $\pm$0.5 mm gave a change in on-axis temperature of 6000 K in 8000 K, while at 0.25 a, the error was only 200 K in 1000 K.

From these results and the others shown in Chapter 4, it would indicate that temperature results on the axis are very susceptible to slight variation in conditions, while those at 0.25 a from the axis were much more stable.

6.3 AXIAL TEMPERATURE DISTRIBUTIONS

The temperature distributions along, and parallel to, the axis of the hot gas jet were derived from collating the radial temperature distributions for each set of results. These distributions are shown in Figs. 34 to 39 in Chapter 5.

The data points indicating distributions parallel to the axis at 0.25 of the maximum jet radius, a, were much more consistent than those on the axis. Taking into account the previous discussion on the radial temperature distributions and the anomalies in the data close to the axis, this is not unexpected. Due to the anomalies, the on-axis distributions are subject to large errors, up to 70%, in the case of radial error.

A correlation between the axial temperature distribution of the jet and the power and flow rate to the torch was sought. In a paper published by Dowd and Maxwell (27), based on the work covered in this report, it was stated that the axial temperature decreased with increased power to the torch. Since that paper was published, the method of deriving fringe shift data from photographs has been modified, and the computer program has been updated.

Fig. 44 shows the on-axis axial temperature distributions for jets of constant flow, but varying powers, and Fig. 45 shows the off-axis temperature distributions for the same conditions, taken from Figs. 37 to 39. In the on-axis curves, there is no discernible correlation, especially if the scatter of points making up these curves, as shown in Figs. 37 to 39 is taken into account. In the off-axis curves, Fig. 45, between axial positions of 5 mm and 15 mm the temperatures seem to decrease with increasing powers, as was indicated in the published paper (27). However, the curves again are too subject to variation to draw any firm conclusions.

Fig. 46 shows the on-axis temperature distribution for jets of constant power but varying flow rates, while Fig. 47 shows the off-axis distributions, taken from Figs. 34 to 36. In the on-axis distribution, Fig. 46, between axial positions of 4 mm and 14 mm, there seems to be an increase in temperature for an increase in flow rate. In the off-axis distribution, Fig. 47, the curves are so close as to be considered superimposed.

Due to the uncertainties in the data on-axis, as discussed in the previous section, it would be reasonable to assume the off-axis data to be more reliable. If this is taken as the case, then from the results presented,

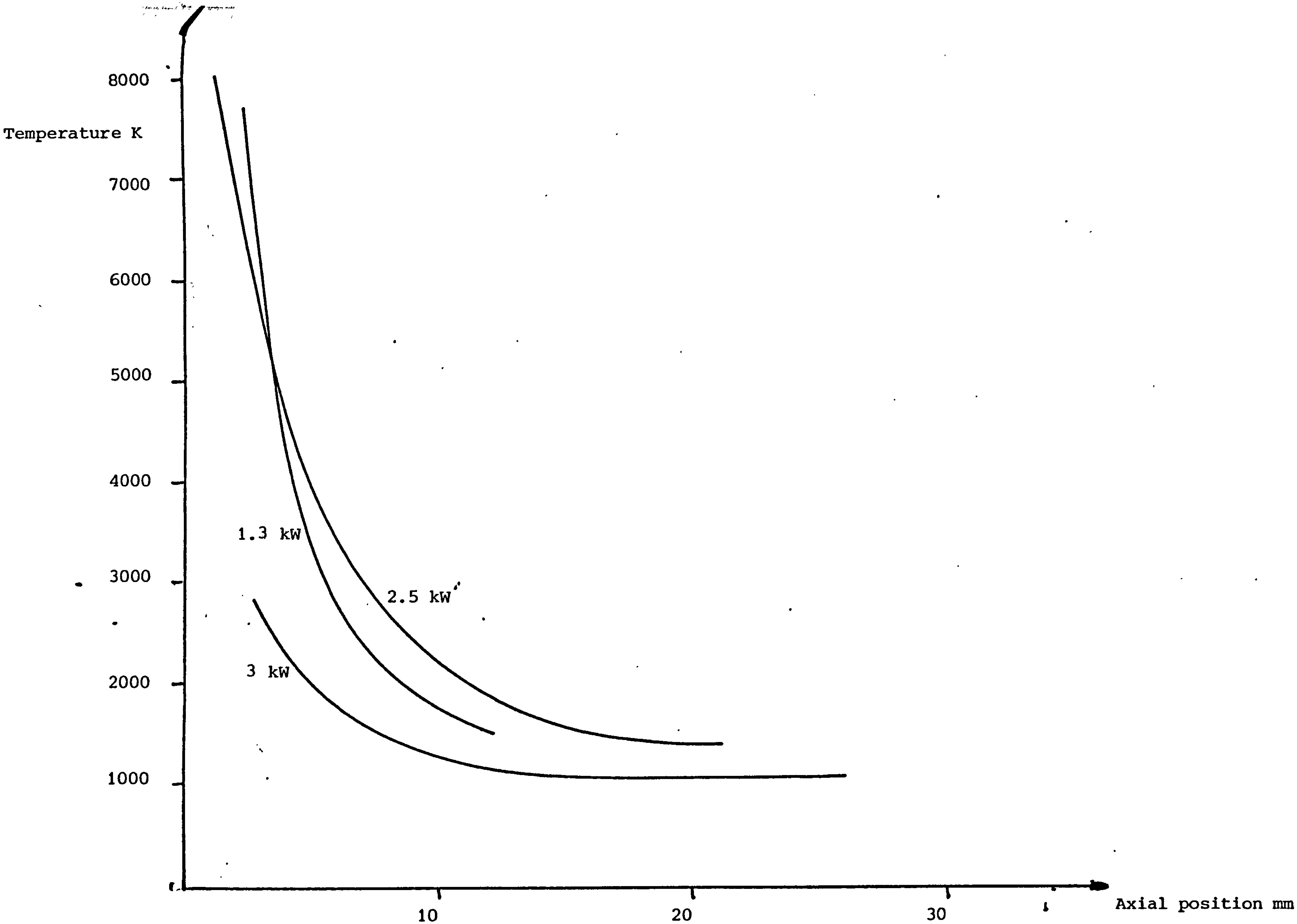

Fig. 44. On axis axial temperature distribution for constant flow rate of 2.4 l/min and varying powers.

Fig. 45. Off axis axial temperature distribution for constant flow rate of 2.4 l/min and varying powers.

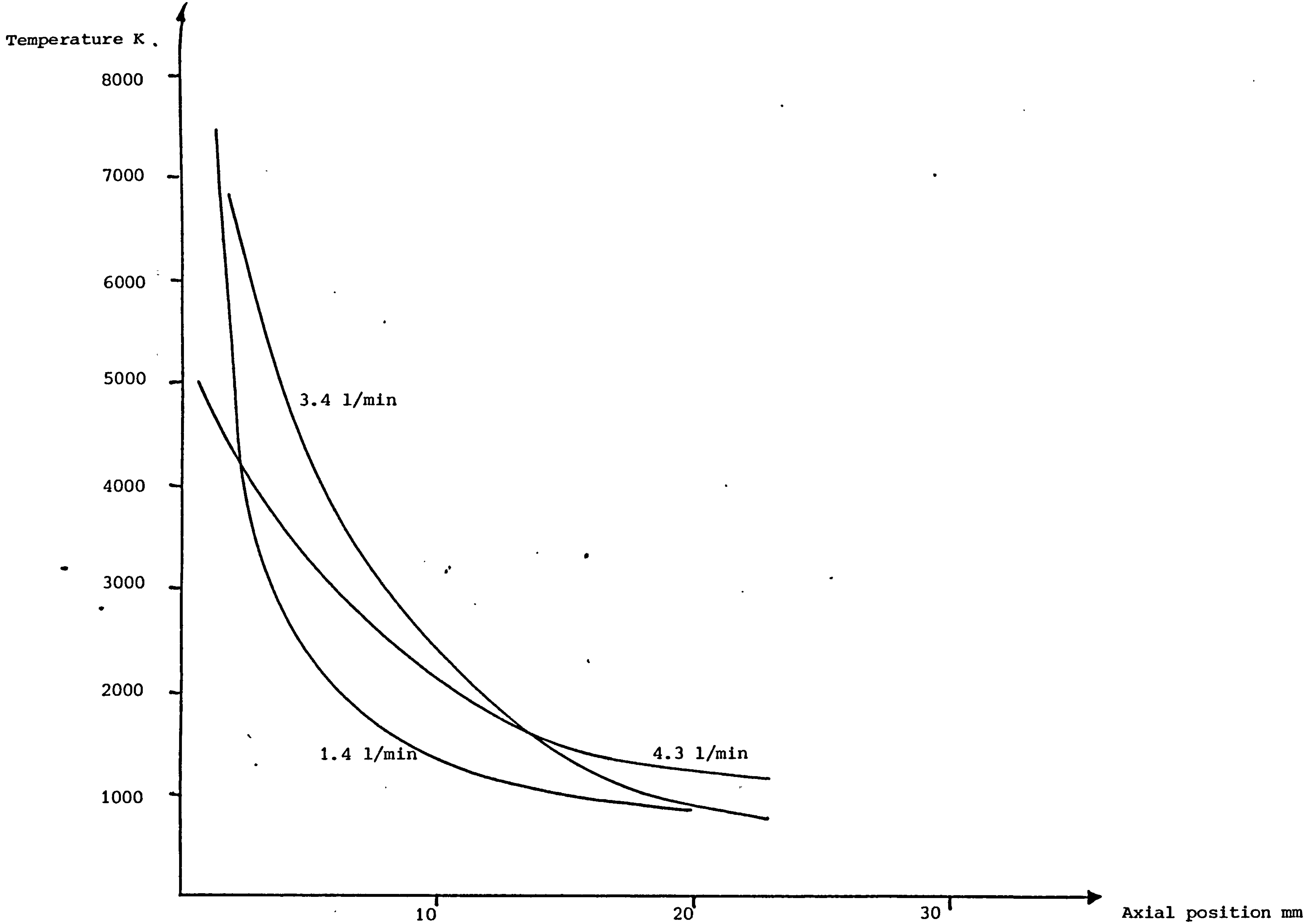

Fig. 46. On axis axial temperature distribution for constant power of 1.4 kW and varying flow rates.

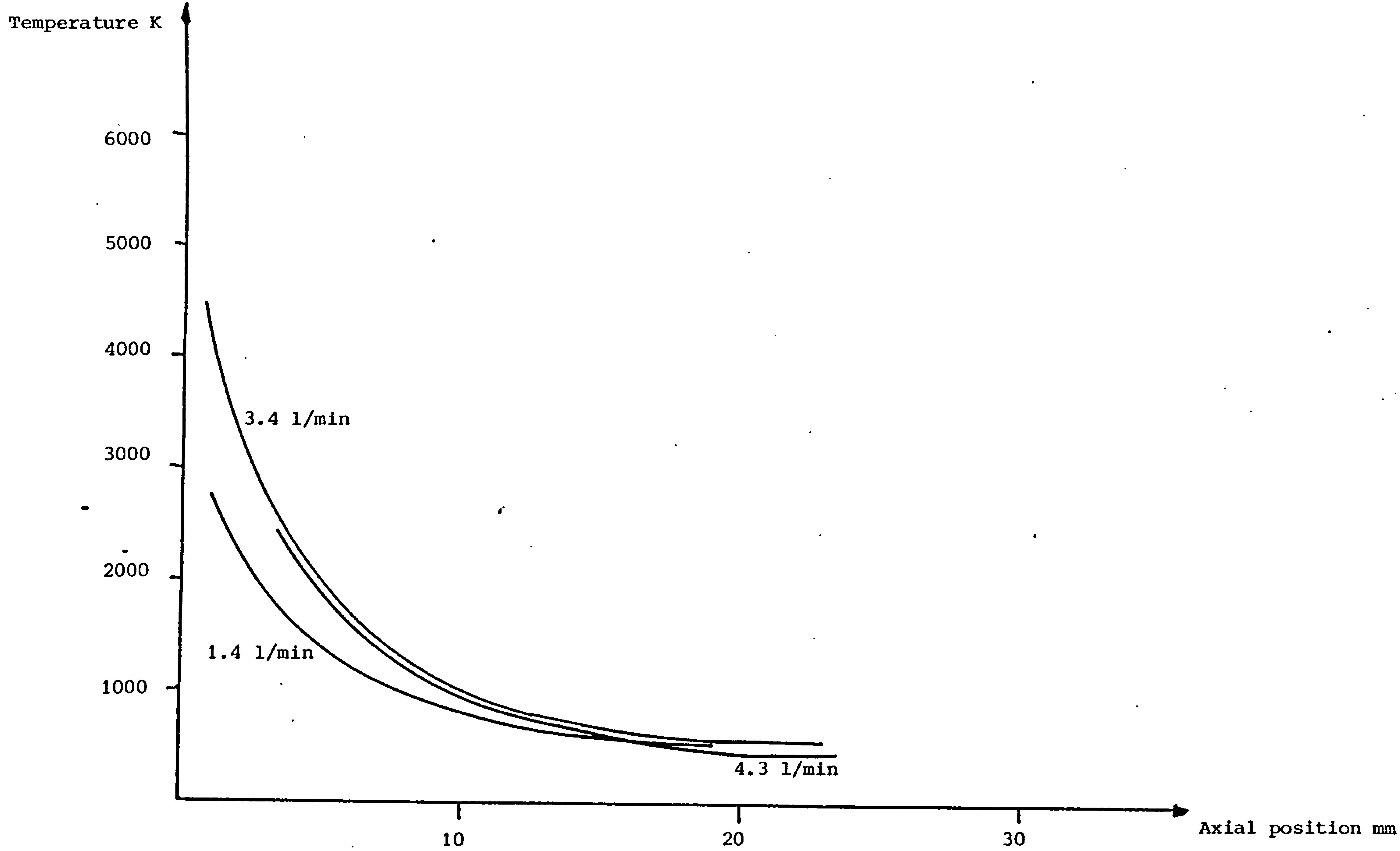

Fig. 47. Off axis axial temperature distribution for constant power of 1.4 kW and varying flow rates.

it would seem to indicate that for constant power supplied to the torch, an argon flow rate change of between 1.4 l/min and 4.3 l/min makes no appreciable difference to the axial temperature of the jet. If, however, the flow rate is kept constant and the power supplied to the torch is varied, there would seem to be a rise in axial temperature of the jet of approximately 40% for a fall in power between 1.4 kW and 3.2 kW, in a short section of the jet between 5 mm and 15 mm above the torch nozzle.

If a simple energy balance is taken for the torch, using the First Law of Thermodynamics, we have

$$\dot{Q}_{in} - \dot{W}_{in} = \sum \dot{m}(h + e_x) \qquad 6.1$$

where $\dot{Q}_{in}$ is the rate of heat flow into the system, in this case zero, $\dot{W}_{in}$ is the rate of work done by the system, in this case the power received by the torch, and hence negative, and $\dot{m}$, h and e_x are the mass flow rates, enthalpy and other energy components of the constituents of the system, in this case the argon and the cooling water to the torch. This reduces to

$$\text{Power} = \dot{m}_w C_{pw} \Delta T_w + \dot{m}_a C_{pa} \Delta T_a$$

$$\Delta T_a = \frac{P - \dot{m}_w C_{pw} \Delta T_w}{\dot{m}_a C_{pa}} \qquad 6.2$$

where P is the power supplied to the torch, $\dot{m}_w$, $\dot{m}_a$, C_{pw}, C_{pa}, ΔT_w and ΔT_a are the mass flow rates, specific heats at constant pressure and the change in temperatures for the cooling water and argon.

It can be seen from equation 6.2 that if the power to the torch is increased while the other variables of the equation are kept constant, the argon jet temperature would be expected to increase. Of course, although it is possible to keep $\dot{m}_w$ and $\dot{m}_a$ constant, and C_{pw} and C_{pa} are physical constants, there is no control of the temperature change of the cooling water. Unfortunately, no temperature measurements were taken in the cooling water for the experiments undertaken in this work. However, in other experiments carried out in the Leicester University Engineering Department on a similar torch, the temperature change in the cooling water remained constant to within 0.5 K over changes in power to the torch of 3 kW, which was more than the range of the experiments here. It would therefore be reasonable to assume that the change in cooling water temperature remained constant in the work covered in this report. This gives rise to the unexpected result of rising temperatures with falling power supplied to the torch.

A hypothesis suggested in the Dowd and Maxwell paper for the reason for this result, was the entrainment of air into the jet, the amount of which varied with power or jet temperature. To investigate this, some data was analysed assuming the jet to be air, rather than argon. Fig. 48 shows the variation in radial temperature between a jet assumed to be air and one assumed to be argon. From this graph, it can be seen that there is a slight rise in temperature of the air jet over the argon jet, but at the 0.25 a off-axis position, the change is less than 7%, which is too small to account for the apparent rise in temperature with fall in power.

The conclusion must then be drawn that the results are coincidental, and the apparent correlation between power and jet temperature is invalid, or that some power loss to the torch is responsible, and the values taken for the power into the torch are not directly proportional to the power into the plasma jet and hence the hot gas jet.

6.4 CLOSE TO THE COOL SURFACE

An aim of this work was to estimate the usefulness of interferometry

Fig. 48. Radial temperature distribution for a set of fringe shift data, comparing a jet of air with one of argon.

to measure the temperature of an impinging gas jet close to the cool surface. However, it was found that no readings could be made within 10 mm of the surface.

It is an intrinsic part of the data transformation between fringe shift and change in refractive index, that the geometrical path length of the optical disturbance in the object beam of the interferometer is known. To be able to measure this from the interferogram, it is necessary to have undisturbed interference fringes in the field of view at the point readings are to be taken. For the numerical transformation used, it is also necessary to be able to assume radial symmetry. Close to the cool surface, neither of the criteria were met.

Within approximately 5 mm of the surface, interference fringes either disappeared completely, or were so turbulent as to be meaningless, and no undisturbed fringes were visible in the field of view as shown in Fig. 20. Between 5 mm from the surface and 10 mm, though this is 15 mm in some examples, the symmetry of the fringe pattern deteriorated and discontinuities appeared in the fringes, implying lack of radial symmetry of the refractive index.

6.5 CONTRIBUTIONS AND LIMITATIONS OF THE PRESENT WORK

The method of interferometry to measure temperature distribution in an impinging gas jet is rather limited. It is, for reasons previously mentioned in this chapter, impossible to obtain readings close to the surface upon which the jet impinges, so the method is only of value to investigate the temperature distributions clear of the surface.

Another limitation on the work is the derivation of the fringe shift data from the photographs. There is difficulty in defining parts of the fringe pattern, as discussed earlier in this chapter. This could be overcome to some extent by using a densimeter to measure the intensity of the light on the photographic interferograms.

The data processing techniques used in this work have been shown to be limited, and very sensitive to input data. There is the instability of the transformed data close to the axis of the jet, especially where the temperature was expected to be high, near the jet nozzle. There was also the necessary assumption that the jet was radially symmetrical. Despite care in choosing the most axially symmetrical photographs to process, and averaging readings over either side of the axis, there was no way to prove this, and errors could have been introduced.

Although the method of temperature measurement used in this work has these limitations, it has indicated a number of fields which would bear further investigation.

6.6 AREAS OF FURTHER INTEREST

The areas of further interest break down into three groups. Further improved experiments using the two dimensional interferometry used in this work, to investigate further the effect of power and flow rate on axial temperature in a jet. Development of more sophisticated data processing methods, for both symmetrical and asymmetrical data. Finally investigation of experimental techniques to obtain three dimensional interferometric data, especially for studying asymmetric gas jets.

To improve the existing experimental method, the main improvement could be made in deriving fringe shift data from the photographic interferograms. A densimeter to measure the light intensity in the fringes would facilitate the demarcation of phase shifts across the fringe patterns. Increasing the shutter speed of the camera could eliminate some of the indistinct fringes caused by turbulence in the jet, or atmospheric and structural vibrations.

Another enhancement would be to investigate the use of two colour interferometry. A frequency doubler in the laser beam would change the wavelength of the light, λ, and by repeating the experiments using this different wavelength, further results could be obtained using different constants in the analysis and thus helping to pinpoint sources of error.

Work could be done to investigate further the effect the shape of the function I(Y) curve has on the transformed data j(r), in the Harker's Transformation. It may be found that using higher orders of approximation for the values of I(Y) between data points would be advantageous. At present a second order approximation is used in the solution. A third order might lead to the elimination of instabilities around $r = 0$.

However, the limitation of the presently used transformation is the need to assume radial symmetry. It would be of interest, in conjunction with three dimensional experimental data, to be able to deal with asymmetric data. There are two possible three dimensional experimental techniques. One is interferometry using two perpendicular light paths through the gas jet, giving simulataneous fringe shift patterns from two directions, which could then be used, with suitable numerical analysis, to account for asymmetries. Another technique is interferometric holography. This gives a three dimensional fringe pattern, which can then be photographed at different angles, building up a complete picture of the data for analysis taking into account any asymmetries.

In conclusion, despite the limitations of the present work, it would be possible to use the results and conclusions drawn from them as a basis for further interesting developments in techniques for the derivation of temperature distributions in gas jets.

APPENDIX AI

NUMERICAL TRANSFORMATION OF COLLIMATED LINEAR DATA TO RADIAL DATA

A1.1 INTRODUCTION

The data resulting from the experiments in this work is taken from measurements along parallel chords in a cylindrical gas jet. In order to estimate radial distribution of parameters, refractive index and hence temperature, from this data, it is necessary to use some mathematical transformation. The use of the Abel inversion formula (26) is a well known technique for removing an unknown from under an integral, and various numerical methods have been suggested for the solution of the inverted equations (9, 28, 29, 30). The method used in this work is one developed by Harker (10). Harker used the solution for electron beam analysis, but his method is easily adapted to the subject of this work.

A1.2 THE NUMERICAL TRANSFORMATION

The equation relating collimated measurements along a parallel chord I(y) to a radial function j(r), as shown in Fig. 49, is

$$I(y) = 2\int_0^{x_o} j(r)\, dx \qquad \text{A1.1}$$

In this study, the function I(y) represents the change in optical path length along a chord of length $2x_0$ located a distance y from the cylinder axis, while j(r) represents the difference between the refractive index of the gas at radius r in the jet and that of the surrounding air.

A change in the variable can be effected. Since

$$r^2 = x^2 + y^2 \quad , \quad 2r\left.\frac{dr}{dx}\right|_y = 2x \quad ,$$

substituting into equation A1.1 gives

$$I(y) = 2\int_y^a \frac{r\, j(r)}{(r^2 - y^2)^{\frac{1}{2}}}\, dr \qquad \text{A1.2}$$

The Abel inversion (26) then transforms this equation to give

$$j(r) = -\frac{1}{\pi}\int_r^a \frac{dI(y)}{dy}\,\frac{1}{(y^2 - r^2)^{\frac{1}{2}}}\, dy \qquad \text{A1.3}$$

From this equation, various methods of solution are possible, by approximating the function I(y) to different order polynomials between points. The method used by Harker assumes that I(y) is smooth enough so that it may be represented by N equally spaced values of y^2 in the range 0 to a^2, where a is the radius at which, and beyond I(y) is zero, then new variables can be introduced

i.e. $\quad Y = \dfrac{Ny^2}{a^2} \qquad \dfrac{dy}{dY} = \dfrac{1}{2}\,\dfrac{a}{(NY)^{\frac{1}{2}}}$

$\quad R = \dfrac{Nr^2}{a^2} \qquad \dfrac{dr}{dR} = \dfrac{1}{2}\,\dfrac{a}{(NR)^{\frac{1}{2}}}$

Substitution into equation A1.3 gives

$$j(R) = -\frac{1}{\pi}\,\frac{N^{\frac{1}{2}}}{a}\int_R^N \frac{dI(Y)}{dY}\,\frac{1}{(Y - R)^{\frac{1}{2}}}\, dY \qquad \text{A1.4}$$

If I(Y) is known at N points, then I(Y) can be approximated to part of a parabola in each of the intervals $0 \leqslant Y \leqslant 2$, $2 \leqslant Y \leqslant 4$, ..., $(N-2) \leqslant Y \leqslant N$, where

$$\left.\begin{aligned} I(Y) &= AY^2 + BY + C \\ \text{and} \quad \frac{dI(Y)}{dY} &= 2AY + B \end{aligned}\right) \qquad \text{A1.5}$$

Substituting into equation A1.4 gives

$$j(R) = -\frac{N^{\frac{1}{2}}}{a\pi}\int_R^N \frac{(2AY + B)}{(Y - R)^{\frac{1}{2}}}\, dY \qquad \text{A1.6}$$

Using Lagrangian Interpolation to solve equations A1.5 for A and B (C is not needed in equation A1.6), in each of the intervals, where in Fig. 50

$$I(Y_1) \equiv i_1 = AY_1^2 + BY_1 + C$$

$$I(Y_2) \equiv i_2 = AY_2^2 + BY_2 + C$$

$$I(Y_3) \equiv i_3 = AY_3^2 + BY_3 + C$$

$$\therefore \quad A = \frac{(Y_2 - Y_1)(i_3 - i_1) - (Y_3 - Y_1)(i_2 - i_1)}{(Y_2 - Y_1)(Y_3^2 - Y_1^2) - (Y_3 - Y_1)(Y_2^2 - Y_1^2)}$$

$$B = \frac{i_2 - i_1 - A(Y_2^2 - Y_1^2)}{Y_2 - Y_1}$$

Consider the three Y variables to be an equal distance of 1 apart, then

$$\left.\begin{aligned} 2A &= i_1 - 2i_2 + i_3 \\ 2B &= (-3 - 2Y_1)i_1 + (4 + 4Y_1)i_2 + (-2Y_1 - 1)i_3 \end{aligned}\right) \qquad \text{A1.7}$$

Integrating equation A1.6 gives

$$j(R) = \frac{-N^{\frac{1}{2}}}{3a\pi}\left\{2.2A\left[(Y - R)^{3/2} + 3R(Y - R)^{\frac{1}{2}}\right]_R^N + 2B\left[3(Y - R)^{\frac{1}{2}}\right]_R^N\right\}$$

$$= \frac{-N^{\frac{1}{2}}}{3a\pi}\left\{2.2A\oint_R^N + 2B\,\mathcal{K}_R^N\right\} \qquad \text{A1.8}$$

where $2A = i_{n-1} - 2i_n + i_{n+1}$

and $2B = (-3 - 2Y_{n-1})i_{n-1} + (4 + 4Y_{n-1})i_n - (1 - 2Y_{n-1})i_{n+1}$

for each interval between R = 0 and N.

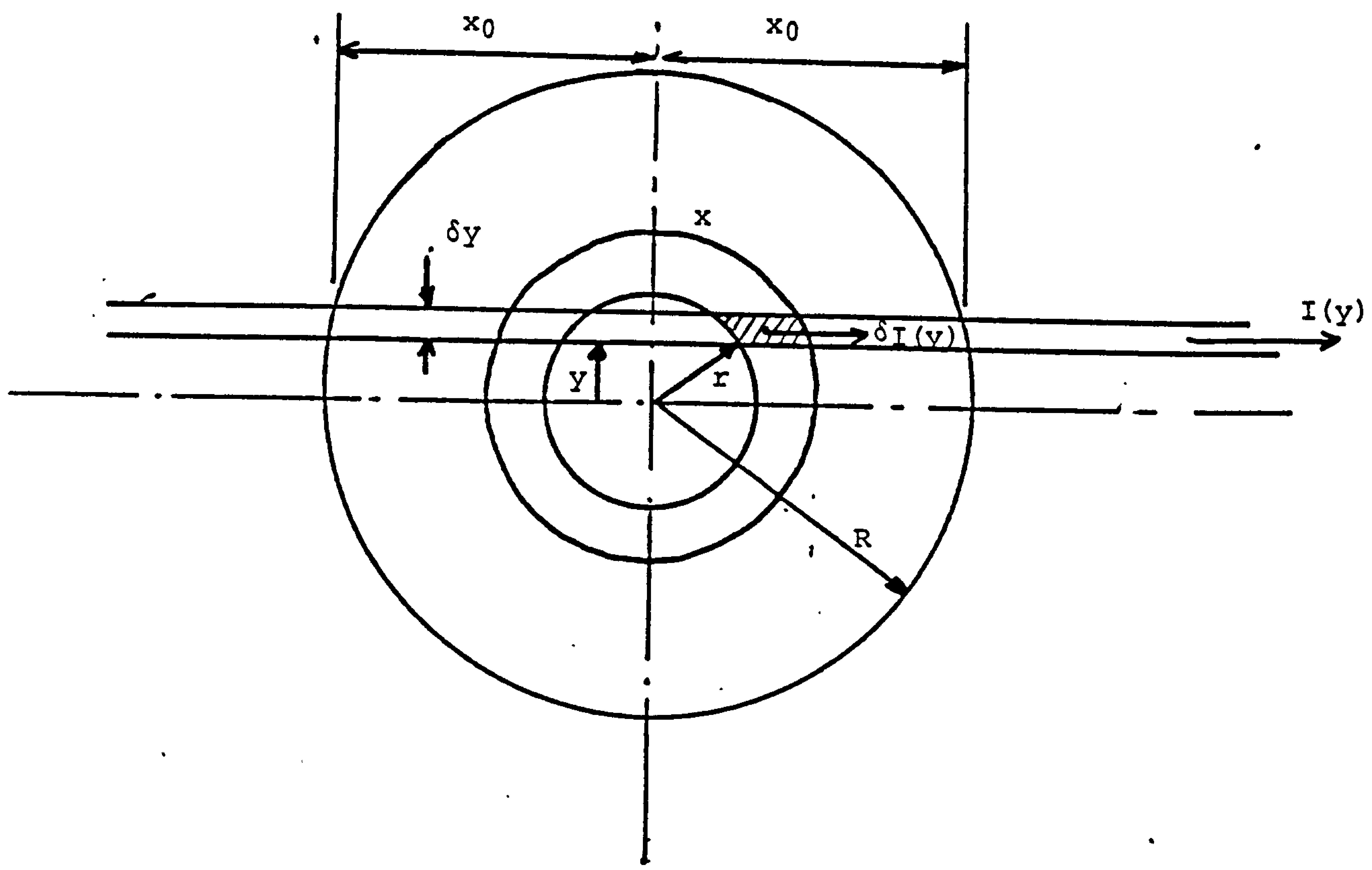

Fig. 49. Cross section of a cylindrical gas column.

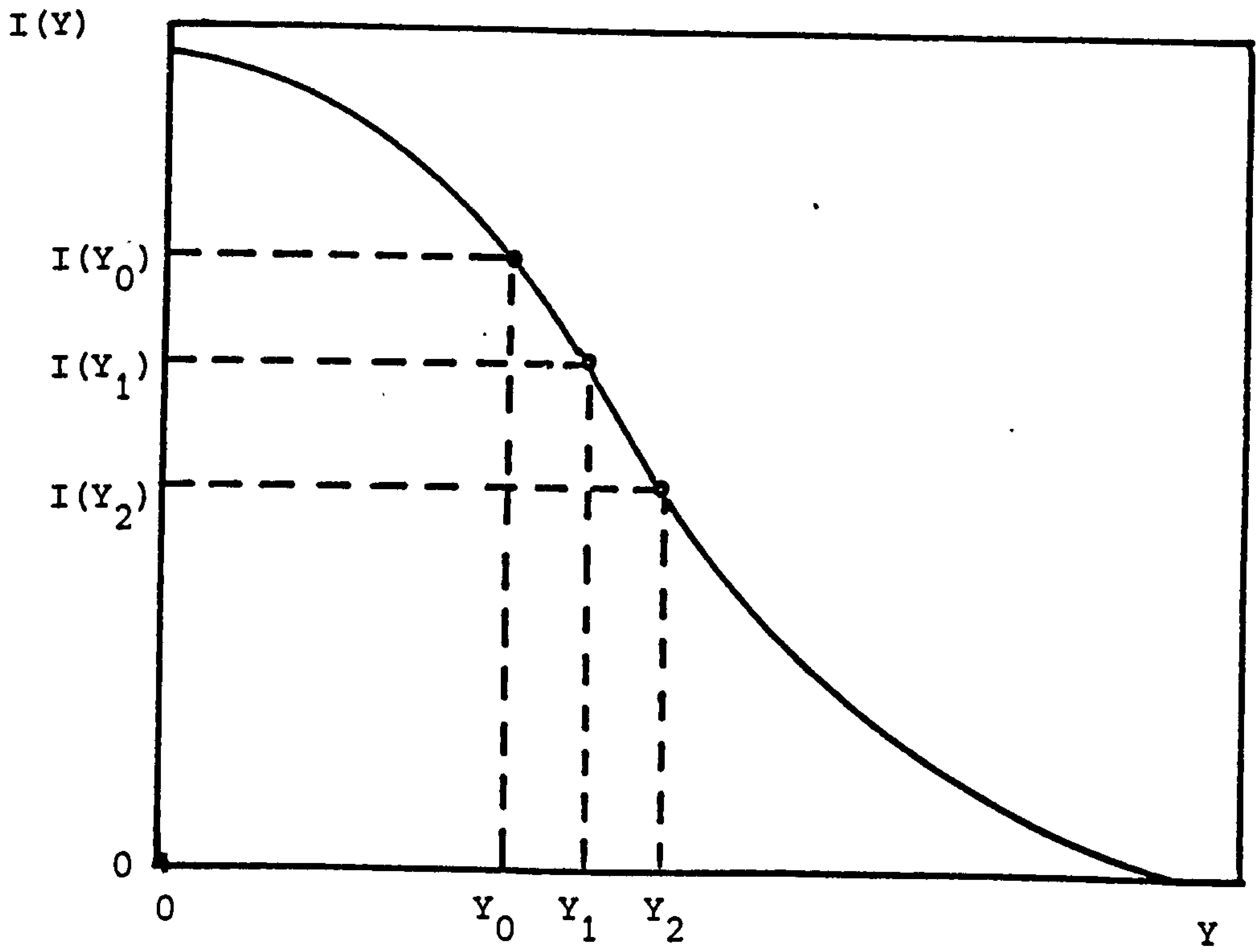

Fig. 50. Lagrangian interpolation coordinates.

Considering R = 0, the section of equation A1.8 within curly brackets evaluates to

$$2\left[i_0 - 2i_1 + i_2\right]\oint_0^2 + \left[(-3 - 2*0)i_0 + (4 + 4*0)i_1 - (1 + 2*0)i_2\right]\mathcal{K}_0^2$$

$$+ 2\left[i_2 - 2i_3 + i_4\right]\oint_2^4 + \left[(-3 - 2*2)i_2 + (4 + 4*2)i_3 - (1 + 2*2)i_4\right]\mathcal{K}_2^4$$

$$+ \;.....$$

$$+ 2\left[i_{N-2} - 2i_{N-1} + i_N\right]\oint_{N-2}^{N} + \Big[(-3 - 2*(N-2))i_{N-2} +$$

$$(4 + 4*(N-2))i_{N-1} - (1 + 2*\overline{N-2})i_N\Big]\mathcal{K}_{N-2}^{N} \qquad \text{A1.9}$$

Rearranging these equations for i gives

$$i_0\left\{2\oint_0^2 \quad -3\,\mathcal{K}_0^2\right\}$$

$$+ i_1\left\{-4\oint_0^2 \quad +4\,\mathcal{K}_0^2\right\}$$

$$+ i_2\left\{2\oint_0^2 + 2\oint_2^4 \quad -1\,\mathcal{K}_0^2 \quad -7\,\mathcal{K}_2^4\right\}$$

$$+ \;.....$$

$$+ i_N\left\{2\oint_{N-2}^{N} \quad -(1 + 2*\overline{N-2})\,\mathcal{K}_{N-2}^{N}\right\}$$

Considering R = 1, the first line of equations A1.9 reduces to

$$2\left[i_0 - 2i_1 + i_2\right]\oint_1^2 + \left[(-3 - 2*0)i_0 + (4 + 4*0)i_1 - (1 + 2*0)i_2\right]\mathcal{K}_1^2$$

while the other lines remain the same. Again rearranging these equations for i gives

$$i_0\left\{2\mathcal{J}_1^2 \qquad -3\,\mathcal{K}_1^2\right\}$$

$$+\ i_1\left\{-4\mathcal{J}_1^2 \qquad +4\,\mathcal{K}_1^2\right\}$$

$$+\ i_2\left\{2\mathcal{J}_1^2 + 2\mathcal{J}_2^4 \quad -1\,\mathcal{K}_1^2 \quad -7\,\mathcal{K}_2^4\right\}$$

$+ \ .....$

$$+\ i_N\left\{2\mathcal{J}_{N-2}^N \qquad -(1 + 2*\overline{N-2})\,\mathcal{K}_{N-2}^N\right\}$$

For R = 2 the first line of equation A1.9 disappears completely, and the pattern continues until R = N.

In this way, a coefficient matrix, M_{RY} can be built up, such that

$$j(R) = \frac{N^{\frac{1}{2}}}{3\pi a} \sum_{Y=0}^{N-1} M_{RY}\, I(Y)$$

Fig. 51 shows the values of matrix M_{RY} for N = 40.

R \ Y	0	1	2	3	4	5	6	7	8	9	10	11	12	13	14	15	16	17	18	19
0	7.07	-5.66	0.54	-0.40	-0.12	-0.18	-0.07	-0.11	-0.04	-0.07	-0.03	-0.05	-0.02	-0.04	-0.02	-0.03	-0.02	-0.03	-0.01	-0.02
1	1.00	4.00	-2.41	-0.78	-0.16	-0.26	-0.09	-0.14	-0.05	-0.09	-0.04	-0.06	-0.03	-0.05	-0.02	-0.04	-0.02	-0.03	-0.01	-0.03
2	0	0	7.07	-5.66	0.54	-0.40	-0.12	-0.18	-0.07	-0.11	-0.04	-0.07	-0.03	-0.05	-0.02	-0.04	-0.02	-0.03	-0.02	-0.03
3	0	0	1.00	4.00	-2.41	-0.78	-0.16	-0.26	-0.09	-0.14	-0.05	-0.09	-0.04	-0.06	-0.03	-0.05	-0.02	-0.04	-0.02	-0.03
4	0	0	0	0	7.07	-5.66	0.54	-0.40	-0.12	-0.18	-0.07	-0.11	-0.04	-0.07	-0.03	-0.05	-0.02	-0.04	-0.02	-0.03
5	0	0	0	0	1.00	4.00	-2.41	-0.78	-0.16	-0.26	-0.09	-0.14	-0.05	-0.09	-0.04	-0.06	-0.03	-0.05	-0.02	-0.04
6	0	0	0	0	0	0	7.07	-5.66	0.54	-0.40	-0.12	-0.18	-0.07	-0.11	-0.04	-0.07	-0.03	-0.05	-0.02	-0.04
7	0	0	0	0	0	0	1.00	4.00	-2.41	-0.78	-0.16	-0.26	-0.09	-0.14	-0.05	-0.09	-0.04	-0.06	-0.03	-0.05
8	0	0	0	0	0	0	0	0	7.07	-5.66	0.54	-0.40	-0.12	-0.18	-0.07	-0.11	-0.04	-0.07	-0.03	-0.05
9	0	0	0	0	0	0	0	0	1.00	4.00	-2.41	-0.78	-0.16	-0.26	-0.09	-0.14	-0.05	-0.09	-0.04	-0.06
10	0	0	0	0	0	0	0	0	0	0	7.07	-5.66	0.54	-0.40	-0.12	-0.18	-0.07	-0.11	-0.04	-0.07
11	0	0	0	0	0	0	0	0	0	0	1.00	4.00	-2.41	-0.78	-0.16	-0.26	-0.09	-0.14	-0.05	-0.09
12	0	0	0	0	0	0	0	0	0	0	0	0	7.07	-5.66	0.54	-0.40	-0.12	-0.18	-0.07	-0.11
13	0	0	0	0	0	0	0	0	0	0	0	0	1.00	4.00	-2.41	-0.78	-0.16	-0.26	-0.09	-0.14
14	0	0	0	0	0	0	0	0	0	0	0	0	0	0	7.07	-5.66	0.54	-0.40	-0.12	-0.18
15	0	0	0	0	0	0	0	0	0	0	0	0	0	0	1.00	4.00	-2.41	-0.78	-0.16	-0.26
16	0	0	0	0	0	0	0	0	0	0	0	0	0	0	0	0	7.07	-5.66	0.54	-0.40
17	0	0	0	0	0	0	0	0	0	0	0	0	0	0	0	0	1.00	4.00	-2.41	-0.78
18	0	0	0	0	0	0	0	0	0	0	0	0	0	0	0	0	0	0	7.07	-5.66
19	0	0	0	0	0	0	0	0	0	0	0	0	0	0	0	0	0	0	1.00	4.00
20	0	0	0	0	0	0	0	0	0	0	0	0	0	0	0	0	0	0	0	0
21	0	0	0	0	0	0	0	0	0	0	0	0	0	0	0	0	0	0	0	0
22	0	0	0	0	0	0	0	0	0	0	0	0	0	0	0	0	0	0	0	0
23	0	0	0	0	0	0	0	0	0	0	0	0	0	0	0	0	0	0	0	0
24	0	0	0	0	0	0	0	0	0	0	0	0	0	0	0	0	0	0	0	0
25	0	0	0	0	0	0	0	0	0	0	0	0	0	0	0	0	0	0	0	0
26	0	0	0	0	0	0	0	0	0	0	0	0	0	0	0	0	0	0	0	0
27	0	0	0	0	0	0	0	0	0	0	0	0	0	0	0	0	0	0	0	0
28	0	0	0	0	0	0	0	0	0	0	0	0	0	0	0	0	0	0	0	0
29	0	0	0	0	0	0	0	0	0	0	0	0	0	0	0	0	0	0	0	0
30	0	0	0	0	0	0	0	0	0	0	0	0	0	0	0	0	0	0	0	0
31	0	0	0	0	0	0	0	0	0	0	0	0	0	0	0	0	0	0	0	0
32	0	0	0	0	0	0	0	0	0	0	0	0	0	0	0	0	0	0	0	0
33	0	0	0	0	0	0	0	0	0	0	0	0	0	0	0	0	0	0	0	0
34	0	0	0	0	0	0	0	0	0	0	0	0	0	0	0	0	0	0	0	0
35	0	0	0	0	0	0	0	0	0	0	0	0	0	0	0	0	0	0	0	0
36	0	0	0	0	0	0	0	0	0	0	0	0	0	0	0	0	0	0	0	0
37	0	0	0	0	0	0	0	0	0	0	0	0	0	0	0	0	0	0	0	0
38	0	0	0	0	0	0	0	0	0	0	0	0	0	0	0	0	0	0	0	0
39	0	0	0	0	0	0	0	0	0	0	0	0	0	0	0	0	0	0	0	0

Fig. 51. Table of values of the coefficient matrix M_{RY} for N = 40

20	21	22	23	24	25	26	27	28	29	30	31	32	33	34	35	36	37	38	39
-0.01	-0.02	-0.01	-0.02	-0.01	-0.02	-0.01	-0.01	-0.01	-0.01	-0.01	-0.01	-0.01	-0.01	-0.01	-0.01	0	-0.01	0	-0.01
-0.01	-0.02	-0.01	-0.02	-0.01	-0.02	-0.01	-0.02	-0.01	-0.01	-0.01	-0.01	-0.01	-0.01	-0.01	-0.01	0	-0.01	0	-0.01
-0.01	-0.02	-0.01	-0.02	-0.01	-0.02	-0.01	-0.02	-0.01	-0.01	-0.01	-0.01	-0.01	-0.01	-0.01	-0.01	-0.01	-0.01	0	-0.01
-0.01	-0.03	-0.01	-0.02	-0.01	-0.02	-0.01	-0.02	-0.01	-0.02	-0.01	-0.01	-0.01	-0.01	-0.01	-0.01	-0.01	-0.01	0	-0.01
-0.02	-0.03	-0.01	-0.02	-0.01	-0.02	-0.01	-0.02	-0.01	-0.02	-0.01	-0.01	-0.01	-0.01	-0.01	-0.01	-0.01	-0.01	-0.01	-0.01
-0.02	-0.03	-0.01	-0.03	-0.01	-0.02	-0.01	-0.02	-0.01	-0.02	-0.01	-0.02	-0.01	-0.01	-0.01	-0.01	-0.01	-0.01	-0.01	-0.01
-0.02	-0.03	-0.01	-0.03	-0.01	-0.02	-0.01	-0.02	-0.01	-0.02	-0.01	-0.02	-0.01	-0.01	-0.01	-0.01	-0.01	-0.01	-0.01	-0.01
-0.02	-0.03	-0.02	-0.03	-0.01	-0.03	-0.01	-0.02	-0.01	-0.02	-0.01	-0.02	-0.01	-0.02	-0.01	-0.01	-0.01	-0.01	-0.01	-0.01
-0.02	-0.04	-0.02	-0.03	-0.02	-0.03	-0.01	-0.02	-0.01	-0.02	-0.01	-0.02	-0.01	-0.02	-0.01	-0.01	-0.01	-0.01	-0.01	-0.01
-0.03	-0.05	-0.02	-0.04	-0.02	-0.03	-0.01	-0.03	-0.01	-0.02	-0.01	-0.02	-0.01	-0.02	-0.01	-0.02	-0.01	-0.01	-0.01	-0.01
-0.03	-0.05	-0.02	-0.04	-0.02	-0.03	-0.02	-0.03	-0.01	-0.02	-0.01	-0.02	-0.01	-0.02	-0.01	-0.02	-0.01	-0.01	-0.01	-0.01
-0.04	-0.06	-0.03	-0.05	-0.02	-0.04	-0.02	-0.03	-0.01	-0.03	-0.01	-0.02	-0.01	-0.02	-0.01	-0.02	-0.01	-0.02	-0.01	-0.01
-0.04	-0.07	-0.03	-0.05	-0.02	-0.04	-0.02	-0.03	-0.02	-0.03	-0.01	-0.02	-0.01	-0.02	-0.01	-0.02	-0.01	-0.02	-0.01	-0.01
-0.05	-0.09	-0.04	-0.06	-0.03	-0.05	-0.02	-0.04	-0.02	-0.03	-0.01	-0.03	-0.01	-0.02	-0.01	-0.02	-0.01	-0.02	-0.01	-0.02
-0.07	-0.11	-0.04	-0.07	-0.03	-0.05	-0.02	-0.04	-0.02	-0.03	-0.02	-0.03	-0.01	-0.02	-0.01	-0.02	-0.01	-0.02	-0.01	-0.02
-0.09	-0.14	-0.05	-0.09	-0.04	-0.06	-0.03	-0.05	-0.02	-0.04	-0.02	-0.03	-0.01	-0.03	-0.01	-0.02	-0.01	-0.02	-0.01	-0.02
-0.12	-0.18	-0.07	-0.11	-0.04	-0.07	-0.03	-0.05	-0.02	-0.04	-0.02	-0.03	-0.02	-0.03	-0.01	-0.02	-0.01	-0.02	-0.01	-0.02
-0.16	-0.26	-0.09	-0.14	-0.05	-0.09	-0.04	-0.06	-0.03	-0.05	-0.02	-0.04	-0.02	-0.03	-0.01	-0.03	-0.01	-0.02	-0.01	-0.02
0.54	-0.40	-0.12	-0.18	-0.07	-0.11	-0.04	-0.07	-0.03	-0.05	-0.02	-0.04	-0.02	-0.03	-0.02	-0.03	-0.01	-0.02	-0.01	-0.02
-2.41	-0.78	-0.16	-0.26	-0.09	-0.14	-0.05	-0.09	-0.04	-0.06	-0.03	-0.05	-0.02	-0.04	-0.02	-0.03	-0.01	-0.03	-0.01	-0.02
7.07	-5.66	0.54	-0.40	-0.12	-0.18	-0.07	-0.11	-0.04	-0.07	-0.03	-0.05	-0.02	-0.04	-0.02	-0.03	-0.02	-0.03	-0.01	-0.02
1.00	4.00	-2.41	-0.78	-0.16	-0.26	-0.09	-0.14	-0.05	-0.09	-0.04	-0.06	-0.03	-0.05	-0.02	-0.04	-0.02	-0.03	-0.01	-0.03
0	0	7.07	-5.66	0.54	-0.40	-0.12	-0.18	-0.07	-0.11	-0.04	-0.07	-0.03	-0.05	-0.02	-0.04	-0.02	-0.03	-0.02	-0.03
0	0	1.00	4.00	-2.41	-0.78	-0.16	-0.26	-0.09	-0.14	-0.05	-0.09	-0.04	-0.06	-0.03	-0.05	-0.02	-0.04	-0.02	-0.03
0	0	0	0	7.07	-5.66	0.54	-0.40	-0.12	-0.18	-0.07	-0.11	-0.04	-0.07	-0.03	-0.05	-0.02	-0.04	-0.02	-0.03
0	0	0	0	1.00	4.00	-2.41	-0.78	-0.16	-0.26	-0.09	-0.14	-0.05	-0.09	-0.04	-0.06	-0.03	-0.05	-0.02	-0.04
0	0	0	0	0	0	7.07	-5.66	0.54	-0.40	-0.12	-0.18	-0.07	-0.11	-0.04	-0.07	-0.03	-0.05	-0.02	-0.04
0	0	0	0	0	0	1.00	4.00	-2.41	-0.78	-0.16	-0.26	-0.09	-0.14	-0.05	-0.09	-0.04	-0.06	-0.03	-0.05
0	0	0	0	0	0	0	0	7.07	-5.66	0.54	-0.40	-0.12	-0.18	-0.07	-0.11	-0.04	-0.07	-0.03	-0.05
0	0	0	0	0	0	0	0	1.00	4.00	-2.41	-0.78	-0.16	-0.26	-0.09	-0.14	-0.05	-0.09	-0.04	-0.06
0	0	0	0	0	0	0	0	0	0	7.07	-5.66	0.54	-0.40	-0.12	-0.18	-0.07	-0.11	-0.04	-0.07
0	0	0	0	0	0	0	0	0	0	1.00	4.00	-2.41	-0.78	-0.16	-0.26	-0.09	-0.14	-0.05	-0.09
0	0	0	0	0	0	0	0	0	0	0	0	7.07	-5.66	0.54	-0.40	-0.12	-0.18	-0.07	-0.11
0	0	0	0	0	0	0	0	0	0	0	0	1.00	4.00	-2.41	-0.78	-0.16	-0.26	-0.09	-0.14
0	0	0	0	0	0	0	0	0	0	0	0	0	0	7.07	-5.66	0.54	-0.40	-0.12	-0.18
0	0	0	0	0	0	0	0	0	0	0	0	0	0	1.00	4.00	-2.41	-0.78	-0.16	-0.26
0	0	0	0	0	0	0	0	0	0	0	0	0	0	0	0	7.07	-5.66	0.54	-0.40
0	0	0	0	0	0	0	0	0	0	0	0	0	0	0	0	1.00	4.00	-2.41	-0.78
0	0	0	0	0	0	0	0	0	0	0	0	0	0	0	0	0	0	7.07	-5.66
0	0	0	0	0	0	0	0	0	0	0	0	0	0	0	0	0	0	1.00	4.00

Fig. 51. continued.

APPENDIX AII THE COMPUTER PROGRAM

A2.1 INTRODUCTION

This appendix contains the listing of the computer program used in this work to calculate radial temperature profiles from fringe shift data due to collimated measurements along parallel chords in a gas jet.

A2.2 PROGRAM LISTING

```
      PROGRAM ALD720 (OUTPUT,TAPE1,TAPE 2=OUTPUT)
      DIMENSION AR(40).TE(40)
     *    ,X1(40),X2(40),X3(40),Y1(40),Y2(40),Y3(40)
     *   ,X(3,40),Y(3,40),D(3)
     *    ,TITLE(3),SUBTI(2),XAX(1)
     *    ,LE1(1),LE2(1),LE3(1),LE4(2),LE5(2)
     *    ,GR1(1),GR2(1),GR3(1)
C     NH=NUMBER OF MARKERS POINTS
C     RA=REFACTIVITY AIR
C     NR=NUMBER OF RUNS
      NH=40
      READ(1,15)TI
15    FORMAT(F6.2)
      READ(1,10)VOLTS,AMPS,FLOW.NR,RA
  10  FORMAT(3F6.2,I1,F8.6)
      DO 20 J=1,NR
      CALL RUN(AR,TE,RA,DIS,NH,TI)
      D(J)=DIS
      DO 40 I=1,NH
      X(J,I)=AR(I)
      Y(J,I)=TE(I)
   40 CONTINUE
   20 CONTINUE
      DO 30 I=1,NH
      X1(I)=X(1,I)
      X2(I)=X(2,I)
      X3(I)=X(3,I)
      Y1(I)=Y(1,I)
      Y2(I)=Y(2,I)
      Y3(I)=Y(3,I)
30    CONTINUE
      D1=D(1)
      D2=D(2)
      D3=D(3)
```

```
      TITLE(1)=10HARGON JET
      TITLE(2)=10HTEMPERATUR
      TITLE(3)=10HE(K)
      SUBTI(1)=10HPROGRAMME
      SUBTI(2)=10H 710
      XAX(1)=10HRADIUS(CM)
      GR1(1)=2H
      GR2(1)=2H
      GR3(1)=2H
      LE1(1)=10HVOLTS
      LE2(1)=10HAMPS
      LE3(1)=10HLITRES/MIN
      LE4(1)=10HCMS(AXIAL
      LE4(2)=10HDISTANCE)
      LE5(1)=10HREF OF AIR

      CALL PLOT32(X1,Y1,X2,Y2,X3,Y3,
     *   GR1,GR2,GR3,LE1,LE2,LE3,LE4,LE5,
     *   D1,D2,D3,VOLTS,AMPS,FLOW,RA,
     *   TITLE,SUBTI,XAX,NH)

      CALL GREND
      STOP
      END
```

```
      SUBROUTINE RUM(AR,TE,RA,DIS,NH,TI)
      DIMENSION AR(1),TE(40),RJ(57),AX(57),AD(57),RE(40)
C     ND=NUMBER OF DATA POINTS
C     AL =RADIUS BEYOND WHICH DATA IS ZERO
C     FD=FRINGE DISTANCE
      READ(1,100)AL,DIS,ND,FD
      WRITE(2,200)DIS,FD

      READ (1,300)(AD(I),I=1,ND)

      AX(1)=0.0
      DO 30 I=2,ND
      AX(I)=AX(I-1)+AL/FLOAT(ND-1)
   30 CONTINUE
      AX(ND)=AL
      DO 25 I=1,ND
      FS=AD(I)
      RJ(I)=FS*6280.0E-8


      WRITE (2,400)I,AX(I),FS,RJ(I)
   25 CONTINUE
      CALL HARK(ND,AX,RJ,NH,AR,AL,RE)
      WRITE (2,1000)
      DO 35 I=1,NH
      TE(I)=(273.0*.000281/(RA-RE(I)))
      WRITE(2,2000)AR(I),RE(I),RA-RE(I),TE(I)
   35 CONTINUE
      RETURN
 2000 FORMAT(1H ,6X,F20.3,2F23.7,F13.2)
 1000 FORMAT(1H ,6HOUTPUT,15X,2HAR,13X,8HR.I.DIFF.13X,7HR.I.ARG,13X,
     *4HTEMP)
  100 FORMAT(2F5.2,I5,F5.2)
  200 FORMAT(1H1,/5X,14HAXIAL DISTANCE,F5.2
     *    ,3X,15HFRINGE DISTANCE,F5.2,///5X,5HINPUT
     *,29X,2HAX,14X,2HFS,13X,9HR.I.DIFF)
  300 FORMAT(5F5.2)
  400 FORMAT(1H ,22X,I3,6X,F10.3,6X,F10.2,6X,F10.6)
      END
```

```
      SUBROUTINE HANK(ND,AX,BJ,NH,AR,AL,RE)
      DIMENSION AX(1),BJ(1),AR(1),RE(1),
     *BI(40),X(57),Y(57),AM(40,40),R(57),W(57)
      DO 20 I=1,NH
      DO 10 J=1,NH
      AM(I,J)=0.0
   10 CONTINUE
   20 CONTINUE
CURVE AX,AD TO X,BI
      DO 100 I=1,ND
      X(I)=AX(I)
      Y(I)=BJ(I)
  100 CONTINUE
      N=ND-1
      IG=N+1
      DO 200 I=1,NH
      A=(FLOAT(I-1)*AL*AL/FLOAT(NH))**0.5
      AR(I)=(FLOAT(I-1)*AL*AL/FLOAT(NH))**0.5
      CALL E01ADF(N,A,X,Y,W,R,IG,VAL)
      BI(I)=VAL
  200 CONTINUE
      CALL NUMB(NH,AM)
C TRANSFORM R,BI TO AR,BJ
      DO 940 I=1,NH
      S=0.0
      DO 930 J=1,NH
      S=S+AM(I,J)*BI(J)
  930 CONTINUE
      RE(I)=(S*FLOAT(NH)**0.5/(3.0*4.0*ATAN(1.0)*AL))
  940 CONTINUE
      RETURN
      END
```

```
      SUBROUTINE NUMB(N,AM)
      DIMENSION AM(40,40)
      C(R,P1,P2,P3,P4)=2.0*((P1-R)**1.5/3.0+R*(P1-R)**0.5-(P2-R)**1.5/3.
     *0-R*(P2-R)**0.5+(P3-R)**1.5/3.0+R*(P3-R)**0.5-(P4-R)**1.5/3.0-R*(
     *P4-R)**0.5)+(-2.0*(P1-2.0)-1.0)*((P1-R)**0.5-(P2-R)**0.5)-(3.0+2.
     *0*P4)*((P3-R)**0.5-(P4-R)**0.5)
      F(R,P3,P4)=-4.0*((P3-R)**1.5/3.0+R*(P3-R)**0.5-(P4-R)**1.5/3.0-R*
     *((P4-R)**0.5))+(4.0+4.0*(P3-2.0))*((P3-R)**0.5-(P4-R)**0.5)
      NM1=N-1
      DO 220 I=1,N
      DO 230 J=1,N
      AM(I,J)=0.0
  230 CONTINUE
  220 CONTINUE
      AM(1,1)=-3.0*(2.0*((2.0**1.5)/3.0)-3.0*(2.0**0.5))
      DO 400 J=3,NM1,2
      P1=FLOAT(J-1)
      P2=P1-2.0
      P3=P1+2.0
      AM(1,J)=-3.0*C(0.0,P1,P2,P3,P1)
  400 CONTINUE
      AM(1,2)=-3.0*(-4.0*(2.0**1.5)/3.0+4.0*2.0**0.5)
      DO 410 J=4,N,2
      P3=FLOAT(J)
      P4=P3-2.0
      AM(1,J)=-3.0*F(0.0,P3,P4)
  410 CONTINUE
      AM(2,1)=1.0
      K=0
      DO 610 J=3,NM1,2
      P1=FLOAT(J-1)
      P2=P1-2.0
      P3=P1+2.0
```

```
      IF(K.GT.0) GO TO 611
      P2=P1-1.0
  611 K=K+1
      AM(2,J)=-3.0*C(1.0,P1,P2,P3,P1)
  610 CONTINUE
      K=0
      DO 620 J=2,N,2
      P3=FLOAT(J)
      P4=P3-2.0
      IF (K.GT.0) GOTO 612
      P4=P3-1.0
612   K=K+1
      AM(2,J)=-3.0*F(1.0,P3,P4)
  620 CONTINUE
      DO 100 I=3,NM1,2
      DO 110 J=3,N
      AM(I,J)=AM(I-2,J-2)
  110 CONTINUE
  100 CONTINUE
      DO 300 I=4,N,2
      DO 310 J=3,N
      AM(I,J)=AM(I-2,J-2)
  310 CONTINUE
  300 CONTINUE
      RETURN
      END


      SUBROUTINE PLOT32(X1,Y1,X2,Y2,X3,Y3,
     *   GR1,GR2,GR3,LE1,LE2,LE3,LE4,LE5,
     *   D1,D2,D3,VOLTS,AMPS,FLOW,RA,
     *   TITLE,SUBTT,XAX,N)
      DIMENSION X1(N),Y1(N),X2(N),Y2(N),X3(N),Y3(N)
     *   ,TITLE(1),XAX(1),GR1(1),GR2(1),GR3(1)
     *   ,LE1(1),LE2(1),LE3(1),LE4(1),LE5(1)

      CALL PAPER(1)
      CALL CTRMAG(12)
      CALL PSPACE(0.0,0.7,0.0,0.9)
      CALL CSPACE(0.0,0.7,0.0,0.9)
      CALL MAP(0.0,30.0,0.0,30.0)
      CALL PLOTCS(2.0,23.0,TITLE,70)
      CALL PLOTCS (20.0,1.0,XAX,10)
      CALL CTRMAG(5)
      CALL REDPEN
      CALL PLOTCS(0.5,0.5,SUBTI,20)
      CALL BLKPEN
      CALL CTRMAG(8)

      CALL PLOTCS(15.0,25.0,LE1,10)
      CALL TYPENF(VOLTS,1)
      CALL PLOTCS(15.0,24.0,LE2,10)
      CALL TYPENF(AMPS,1)
      CALL PLOTCS(15.0,23.0,LE3,10)
      CALL TYPENF(FLOW,4)
      CALL PLOTCS(15.0,22.0,LE5,10)
      CALL TYPENF(RA,6)

      XMAX =-1.0E+70
      XMIN =+1.0E+70
      YMAX =-1.0E+70
      YMIN =+1.0E+70

      DO 10 I=1,N
      IF (X1(I).LT.XMIN) XMIN=X1(I)
      IF (X1(I).GT.XMAX) XMAX=X1(I)
      IF (Y1(I).GT.YMAX) YMAX=Y1(I)
      IF (Y1(I).LT.YMIN) YMIN=Y1(I)

      IF (Y2(I).LT.YMIN) YMIN=Y2(I)
      IF (X2(I).LT.XMIN) XMIN=X2(I)
      IF (X2(I).GT.XMAX) XMAX=X2(I)
      IF (Y2(I).GT.YMAX) YMAX=Y2(I)
```

```
      IF (Y3(I).GT.YMAX) YMAX=Y3(I)
      IF (Y3(I).LT.YMIN) YMIN=Y3(I)
      IF (X3(I).GT.XMAX) XMAX=X3(I)
      IF (X3(I).LT.XMIN) XMIN=X3(I)
   10 CONTINUE

      XMAX=1.2*XMAX
      YMAX=1.2*YMAX

      CALL PSPACE(0.1,0.6,0.1,0.8)
      CALL MAP(XMIN,XMAX,YMIN,YMAX)
      CALL AXES


      CALL POSITN(X1(1),Y1(1))
      DO 20 I=2,N
      CALL JOIN(X1(I),Y1(I))
   20 CONTINUE
      CALL PLOTCS(X1(2),Y1(3),GR1,2)
      CALL TYPENF(D1,1)
      CALL CTRMAG(6)
      CALL PLOTCS(X1(5),Y3(3),LE4,20)
      CALL CTRMAG(8)

      CALL POSITN(X2(1),Y2(1))
      DO 30 I=2,N
      CALL JOIN(X2(I),Y2(I))
   30 CONTINUE
      CALL PLOTCS(X1(2),Y2(3),GR2,2)
      CALL TYPENF(D2,1)

      CALL POSITN(X3(1),Y3(1))
      DO 40 I=2,N
      CALL JOIN(X3(I),Y3(I))
   40 CONTINUE
      CALL PLOTCS(X1(2),Y3(3),GR3,2)
      CALL TYPENF(D3,1)

      CALL FRAME

      RETURN
      END
```

AXIAL DISTANCE .26 FRINGE DISTANCE 3.50

INPUT

	AX	FS	O.P.D.
1	0	2.14	.000134
2	.017	2.12	.000133
3	.034	2.10	.000132
4	.050	2.06	.000129
5	.067	2.02	.000127
6	.084	1.97	.000124
7	.101	1.92	.000121
8	.118	1.85	.000116
9	.135	1.77	.000111
10	.151	1.68	.000106
11	.168	1.58	.000099
12	.185	1.46	.000092
13	.202	1.33	.000084
14	.219	1.19	.000075
15	.235	1.04	.000065
16	.252	.87	.000055
17	.269	.71	.000045
18	.286	.56	.000035
19	.303	.43	.000027
20	.320	.30	.000019
21	.336	.19	.000012
22	.353	.09	.000006
23	.370	0	0

OUTPUT

AR	R.I.DIFF	R.I.ARG	TEMP
0	.0002779	.0000121	6314.43
.059	.0002509	.0000391	1959.87
.083	.0002368	.0000532	1442.60
.101	.0002394	.0000506	1516.51
.117	.0002361	.0000539	1424.52
.131	.0002318	.0000582	1318.17
.143	.0002275	.0000625	1226.61
.155	.0002239	.0000661	1160.90
.165	.0002218	.0000682	1125.30
.176	.0002178	.0000722	1062.10
.185	.0002119	.0000781	982.01
.194	.0002060	.0000840	913.54
.203	.0002004	.0000896	856.29
.211	.0001942	.0000958	800.77
.219	.0001878	.0001022	750.89
.227	.0001829	.0001071	716.01
.234	.0001779	.0001121	684.38
.241	.0001702	.0001198	640.16
.248	.0001605	.0001295	592.26
.255	.0001500	.0001400	548.04
.262	.0001407	.0001493	513.80
.268	.0001325	.0001575	486.94
.274	.0001240	.0001660	452.26
.281	.0001150	.0001750	438.45
.287	.0001065	.0001835	418.07
.293	.0001000	.0001900	403.73
.298	.0000945	.0001955	392.36
.304	.0000894	.0002006	382.33
.310	.0000833	.0002067	371.15
.315	.0000760	.0002140	358.54
.320	.0000688	.0002212	346.79
.326	.0000625	.0002275	337.26
.331	.0000570	.0002330	329.17
.336	.0000520	.0002380	322.32
.341	.0000469	.0002431	315.60
.346	.0000416	.0002494	308.78
.351	.0000360	.0002540	301.97
.356	.0000302	.0002598	295.26
.361	.0000240	.0002650	288.38
.365	.0000167	.0002733	280.57

AXIAL DISTANCE .33 FRINGE DISTANCE 3.50

INPUT

	AX	FS	O.P.D.
1	0	2.18	.000137
2	.017	2.16	.000136
3	.033	2.14	.000134
4	.050	2.10	.000132
5	.066	2.06	.000129
6	.083	2.01	.000126
7	.099	1.95	.000122
8	.116	1.89	.000119
9	.132	1.82	.000114
10	.149	1.74	.000109
11	.165	1.65	.000104
12	.182	1.55	.000097
13	.198	1.44	.000090
14	.215	1.32	.000083
15	.231	1.18	.000074
16	.248	1.04	.000065
17	.264	.89	.000056
18	.281	.74	.000046
19	.297	.60	.000038
20	.314	.45	.000028
21	.330	.32	.000020
22	.347	.20	.000013
23	.363	.10	.000006
24	.380	0	0

OUTPUT

AR	R.T.DIFF	R.I.ARG	TEMP
0	.0002778	.0000122	6308.12
.060	.0002501	.0000399	1922.81
.085	.0002394	.0000506	1515.55
.104	.0002301	.0000599	1280.16
.120	.0002266	.0000634	1209.95
.134	.0002230	.0000670	1144.44
.147	.0002193	.0000707	1085.54
.159	.0002155	.0000745	1029.79
.170	.0002116	.0000784	978.19
.180	.0002076	.0000824	931.03
.190	.0002032	.0000868	883.49
.199	.0001989	.0000911	842.14
.208	.0001957	.0000943	813.32
.217	.0001920	.0000980	782.62
.225	.0001857	.0001043	735.71
.233	.0001778	.0001122	683.50
.240	.0001711	.0001189	645.41
.248	.0001659	.0001241	618.08
.255	.0001599	.0001301	589.61
.262	.0001527	.0001373	558.53
.269	.0001449	.0001451	528.74
.275	.0001366	.0001534	499.98
.282	.0001287	.0001613	475.62
.288	.0001231	.0001659	459.54
.294	.0001182	.0001718	446.58
.300	.0001125	.0001775	432.18
.306	.0001052	.0001848	415.06
.312	.0000962	.0001938	395.78
.318	.0000879	.0002021	379.55
.324	.0000813	.0002087	367.55
.329	.0000754	.0002146	357.40
.335	.0000692	.0002208	347.42
.340	.0000626	.0002274	337.39
.345	.0000557	.0002343	327.39
.350	.0000493	.0002407	318.68
.355	.0000440	.0002460	311.85
.360	.0000390	.0002510	305.63
.365	.0000339	.0002561	299.53
.370	.0000277	.0002623	292.47
.375	.0000195	.0002705	283.61

AXIAL DISTANCF .42 FRINGF DISTANCE 3.50

INPUT

	AX	FS	O.P.D.
1	0	2.21	.000139
2	.016	2.19	.000138
3	.032	2.16	.000136
4	.048	2.13	.000134
5	.064	2.10	.000132
6	.080	2.05	.000129
7	.096	2.00	.000126
8	.112	1.93	.000121
9	.128	1.86	.000117
10	.144	1.77	.000111
11	.160	1.68	.000106
12	.176	1.57	.000099
13	.192	1.46	.000092
14	.208	1.35	.000085
15	.224	1.22	.000077
16	.240	1.08	.000068
17	.256	.94	.000059
18	.272	.77	.000048
19	.288	.63	.000040
20	.304	.50	.000031
21	.320	.38	.000024
22	.336	.28	.000018
23	.352	.20	.000013
24	.368	.12	.000008
25	.384	.06	.000004
26	.400	0	0

OUTPUT

AR	R.I.DIFF	R.I.ARG	TEMP
0	.0002797	.0000103	7444.50
.063	.0002563	.0000337	2279.21
.089	.0002488	.0000412	1860.34
.110	.0002402	.0000498	1539.48
.126	.0002391	.0000509	1507.87
.141	.0002294	.0000606	1266.80
.155	.0002247	.0000653	1175.27
.167	.0002195	.0000705	1088.40
.179	.0002100	.0000800	958.79
.190	.0002020	.0000880	872.12
.200	.0001971	.0000929	826.06
.210	.0001946	.0000954	804.06
.219	.0001900	.0001000	765.89
.228	.0001820	.0001080	710.16
.237	.0001727	.0001173	653.98
.245	.0001669	.0001231	623.20
.253	.0001637	.0001263	607.52
.261	.0001558	.0001342	571.56
.268	.0001425	.0001475	520.10
.276	.0001284	.0001616	474.68
.283	.0001180	.0001720	446.13
.290	.0001109	.0001791	428.23
.297	.0001034	.0001866	411.13
.303	.0000954	.0001946	394.28
.310	.0000875	.0002025	378.79
.316	.0000796	.0002104	364.55
.322	.0000720	.0002180	351.89
.329	.0000648	.0002252	340.59
.335	.0000583	.0002317	331.08
.341	.0000535	.0002365	324.33
.346	.0000497	.0002403	319.18
.352	.0000465	.0002435	315.00
.358	.0000424	.0002476	309.77
.363	.0000368	.0002532	302.99
.369	.0000313	.0002587	296.51
.374	.0000271	.0002629	291.81
.379	.0000237	.0002653	288.07
.385	.0000208	.0002692	285.00
.390	.0000172	.0002728	281.23
.395	.0000122	.0002778	276.14

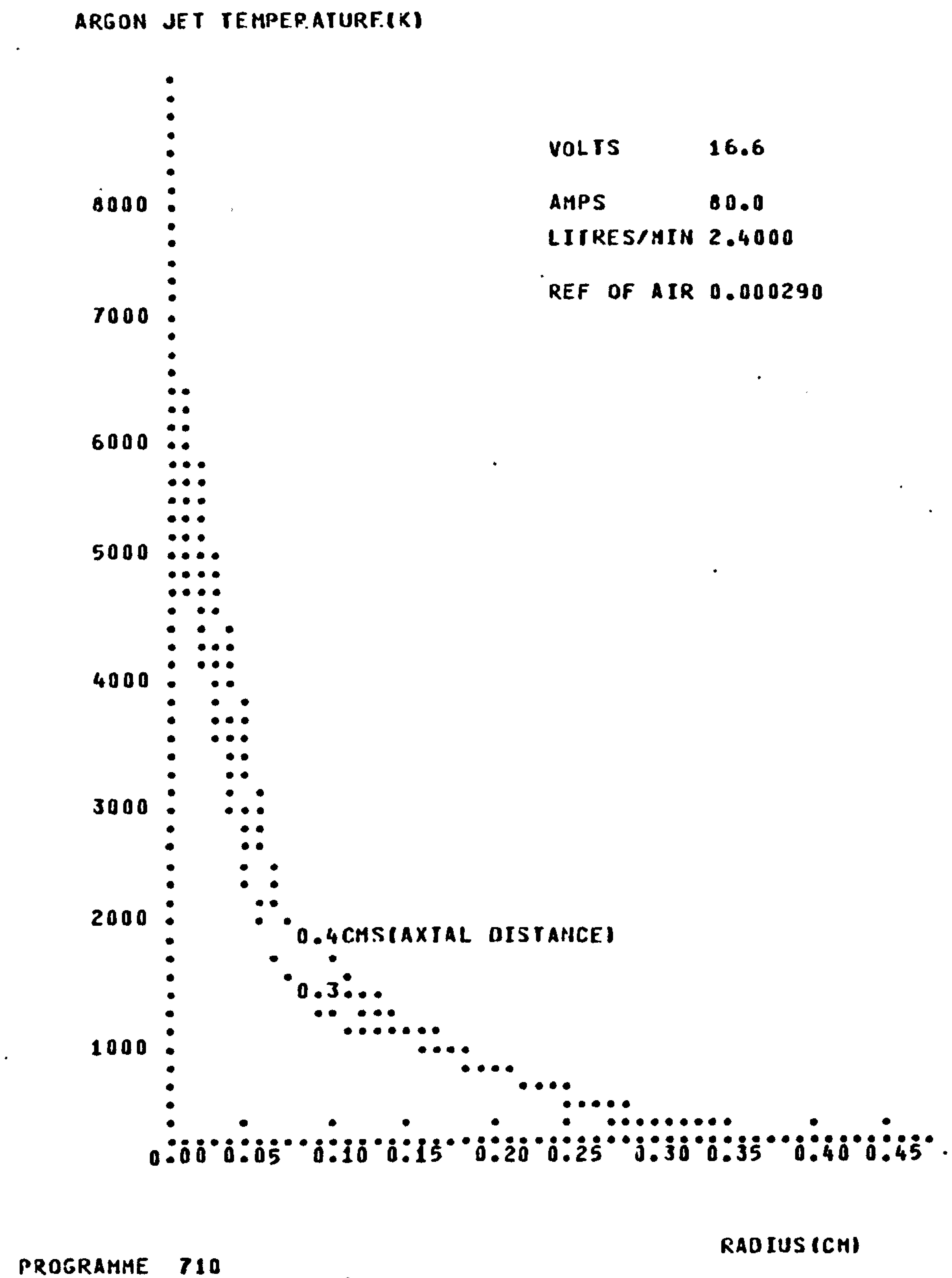
ARGON JET TEMPERATURE(K)
VOLTS 16.6
AMPS 80.0
LITRES/MIN 2.4000
REF OF AIR 0.000290
8000
7000
6000
5000
4000
3000
2000
1000
0.4CMS(AXIAL DISTANCE)
0.3
0.00 0.05 0.10 0.15 0.20 0.25 0.30 0.35 0.40 0.45
RADIUS(CM)
PROGRAMME 710

APPENDIX AIII THE CALCULATION OF IONISATION WITH TEMPERATURE

A3.1 INTRODUCTION

A gas becomes ionised when the atoms of that gas have absorbed sufficient energy for electrons to escape. A way for the atoms to gain enough energy for this to occur, is for the gas to be heated to high temperatures by an electric arc, as in this work.

A3.2 THE RELATIONSHIP BETWEEN TEMPERATURE AND DEGREE OF IONISATION

Assuming there is a degree of ionisation ε in a gas mixture containing atoms, ions and electrons, then the particle density in the mixture is given by (31)

$$N_T \Rightarrow (1 - \varepsilon)N_{AI} + \varepsilon N_{AII} + \varepsilon N_E$$

where N_{AI}, N_{AII} and N_E are the relative particle densities of atoms, ions and electrons respectively. When $\varepsilon = 1$, there is total ionisation and when $\varepsilon = 0$ there is no ionisation. The total number of particles is therefore $(1 + \varepsilon)$, so expressions for the individual particle densities can be obtained as (19)

$$n_{AI} = \frac{1 - \varepsilon}{1 + \varepsilon} \quad ; \quad n_{AII} = \frac{\varepsilon}{1 + \varepsilon} \quad ; \quad n_E = \frac{\varepsilon}{1 + \varepsilon}$$

Thus, using Saha's equation,

$$\frac{N_E \, N_{AII}}{N_{AI}} = 2\left(\frac{2\pi m_e kT}{h}\right)^{3/2} \exp(-X/kT)$$

where $N_E = n_E.kT/p$, $N_{AI} = n_{AI}.kT/p$ and $N_{AII} = n_{AII}.kT/p$.

Thus the expression for degree of ionisation is (10, 32, 33)

$$\frac{\varepsilon^2}{1 - \varepsilon^2} = \frac{2kT}{p}\left(\frac{2\pi m_e kT}{h^2}\right)^{3/2} \exp(-X/kT)$$

Expanding this equation for ε, assuming atmospheric pressure, a relationship between the temperature and degree of ionisation of argon can be calculated. The values thus obtained are shown in Fig. 2.

APPENDIX AIV THE CALIBRATION OF A ROTAMETER

A4.1 INTRODUCTION

Argon and water flow rates to the experimental apparatus are metered by metric rotameters. The water gauge is calibrated directly, but for the one used by the argon, the relatioship between the scale markings on the rotameter and the gas flow rate has to be calculated.

A4.2 CALIBRATION OF A ROTAMETER FOR ARGON FLOW

The manufacturer's data associated with the rotameter gives constants and equations from which the calibration curves for the different size tubes and different weight floats can be determined.

The physical constants used are:

Argon density	$1.7837\ 10^{-3}$ gm/cm^2 at STP
Working density ρ	$\frac{(\text{line pressure} + 14.7)}{14.7}\ 1.7837\ 10^{-3}$ gm/cm^2
Kinematic viscosity ν	$\frac{221.7\ 10^{-6}}{\rho}$ gm/cm.s
Weight of the float ω	0.278 gm for size 7 rotameter
	0.689 gm for size 10 rotameter
Density of the float σ	2.80 gm/cm^2
Constant K_1	0.147 for size 7 rotameter
	0.224 for size 10 rotameter
Constant K_2	0.679 for size 7 rotameter
	0.892 for size 10 rotameter

Relationships for $I = \log \left\{ K_1 \times \nu \sqrt{\frac{\sigma \times \rho}{\omega(\sigma - \rho)}} \times 10^4 \right\}$

and $F_T = K_2 \times \sqrt{\frac{\omega(\sigma - \rho)}{\sigma \times \rho}}$ are given, which relate to the theoretical capacity with no change in Reynolds Number.

From a manufacturer's chart it is possible to read values of f against scale readings on the tube. Now the free flow of the argon is given as $f \times F_T \times \frac{(\text{line pressure} + 14.7)}{14.7}$ l/min , hence it is possible to plot a curve of flow rate against scale reading, for the rotameter, at different argon line pressures (Fig. 8).

APPENDIX AV RADIAL TEMPERATURE DISTRIBUTION

A5.1 INTRODUCTION

This Appendix contains samples of the graphical output of the computer program, showing the radial temperature distribution curves for three sets of data from one fringe pattern photograph at a time.

PAGE NUMBERS CUT OFF IN ORIGINAL

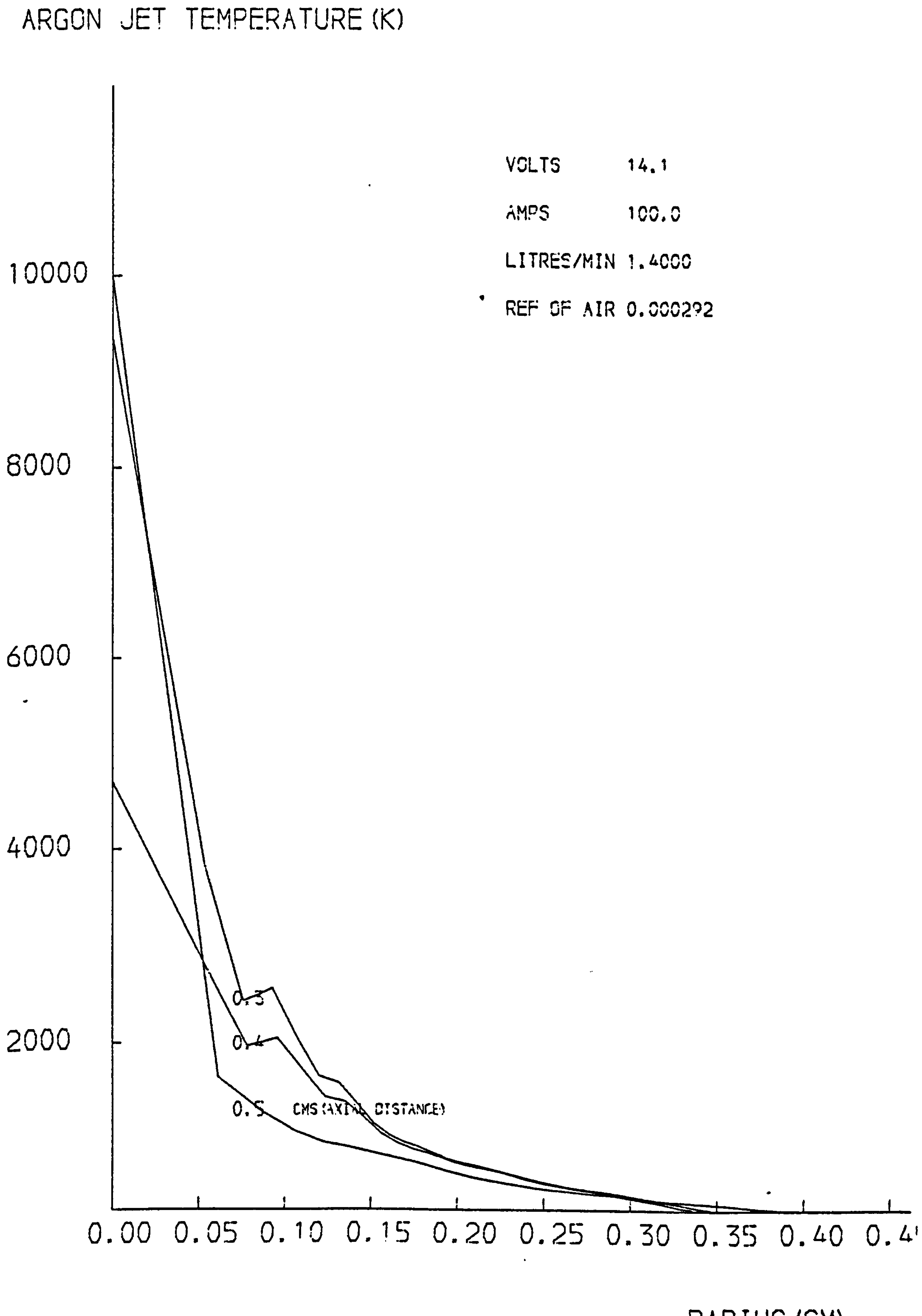

PROGRAMME 710

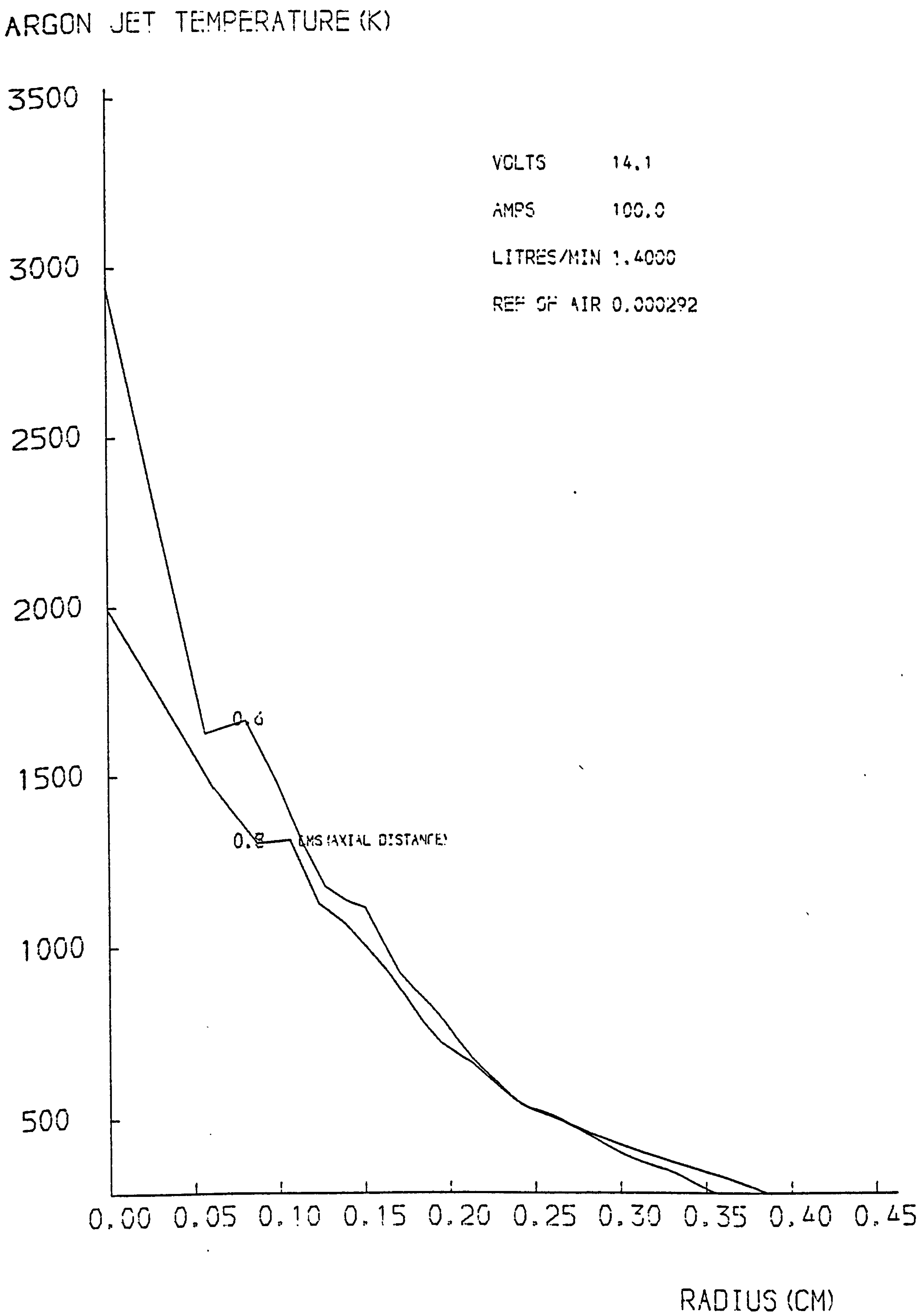
ARGON JET TEMPERATURE (K)
3500
3000
2500
2000
1500
1000
500
VOLTS 14.1
AMPS 100.0
LITRES/MIN 1.4000
REF OF AIR 0.000292
0.6
0.8 CMS (AXIAL DISTANCE)
0.00 0.05 0.10 0.15 0.20 0.25 0.30 0.35 0.40 0.45
RADIUS (CM)

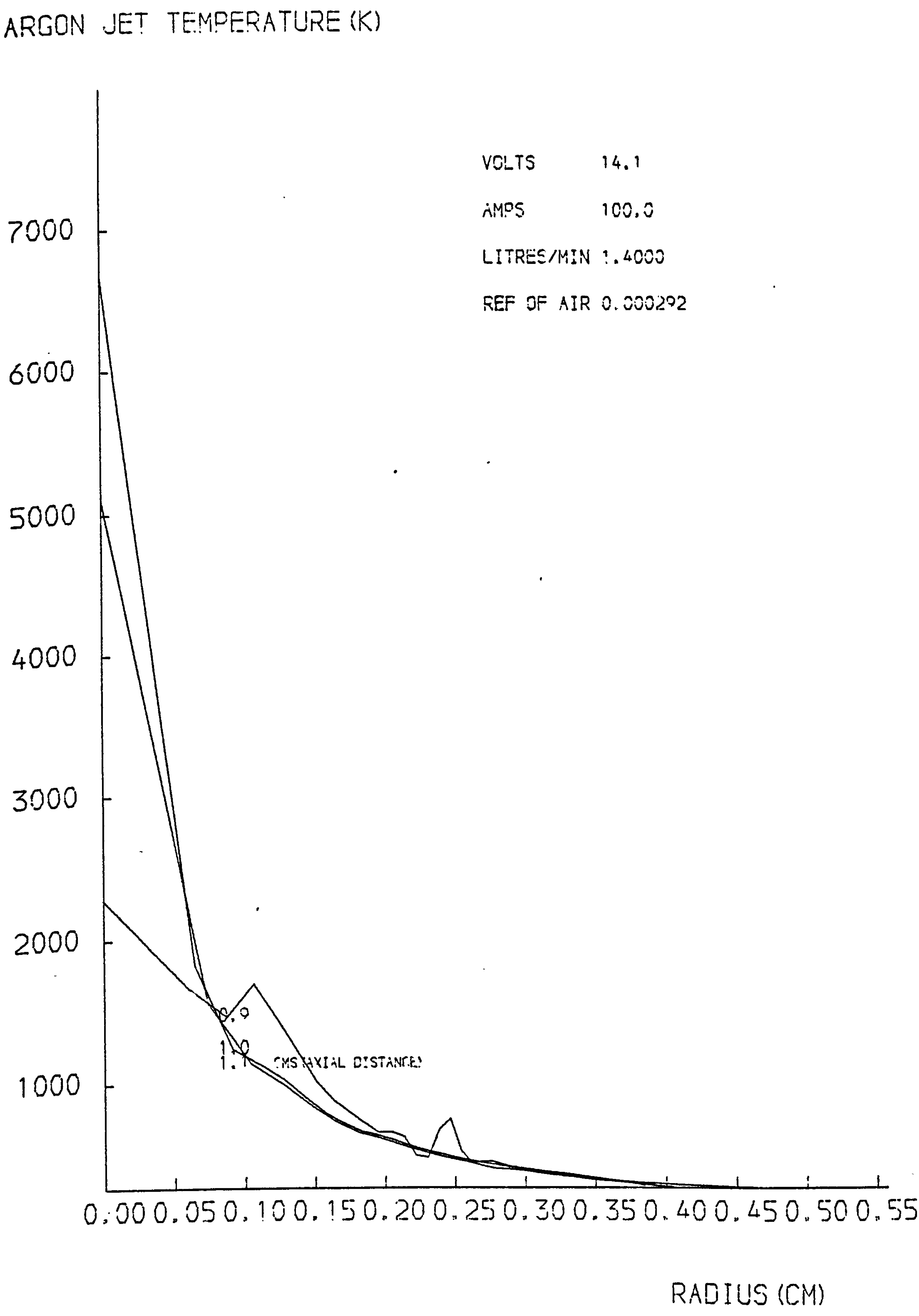
ARGON JET TEMPERATURE (K)
VOLTS 14.1
AMPS 100.0
LITRES/MIN 1.4000
REF OF AIR 0.000292
7000
6000
5000
4000
3000
2000
1000
0.9
1.0
1.1
CMS (AXIAL DISTANCE)
0.00 0.05 0.10 0.15 0.20 0.25 0.30 0.35 0.40 0.45 0.50 0.55
RADIUS (CM)

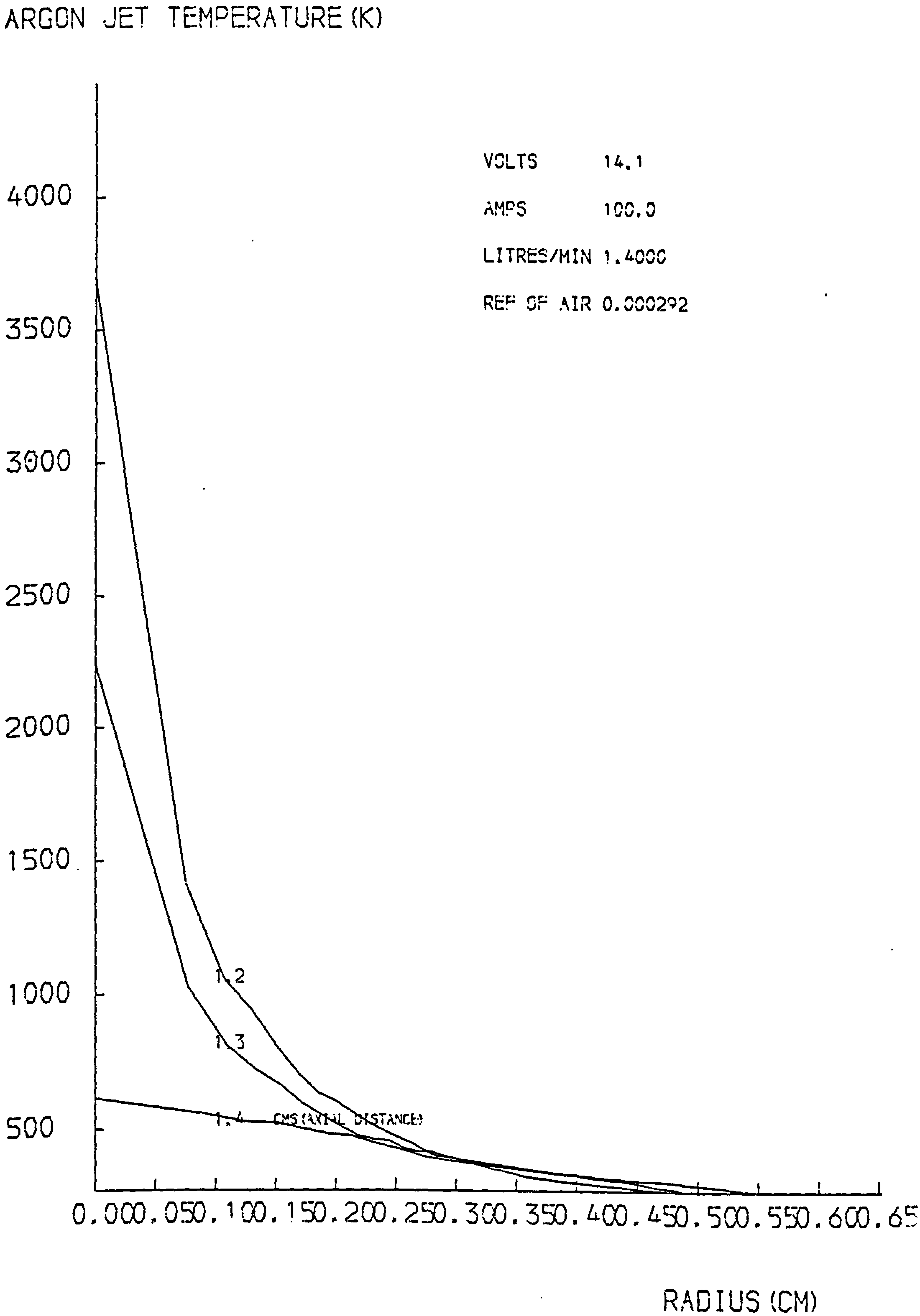
ARGON JET TEMPERATURE (K)
VOLTS 14.1
AMPS 100.0
LITRES/MIN 1.4000
REF OF AIR 0.000292
4000
3500
3000
2500
2000
1500
1000
500
1.2
1.3
1.4 CMS (AXIAL DISTANCE)
0.000.050.100.150.200.250.300.350.400.450.500.550.600.65
RADIUS (CM)

ARGON JET TEMPERATURE (K)

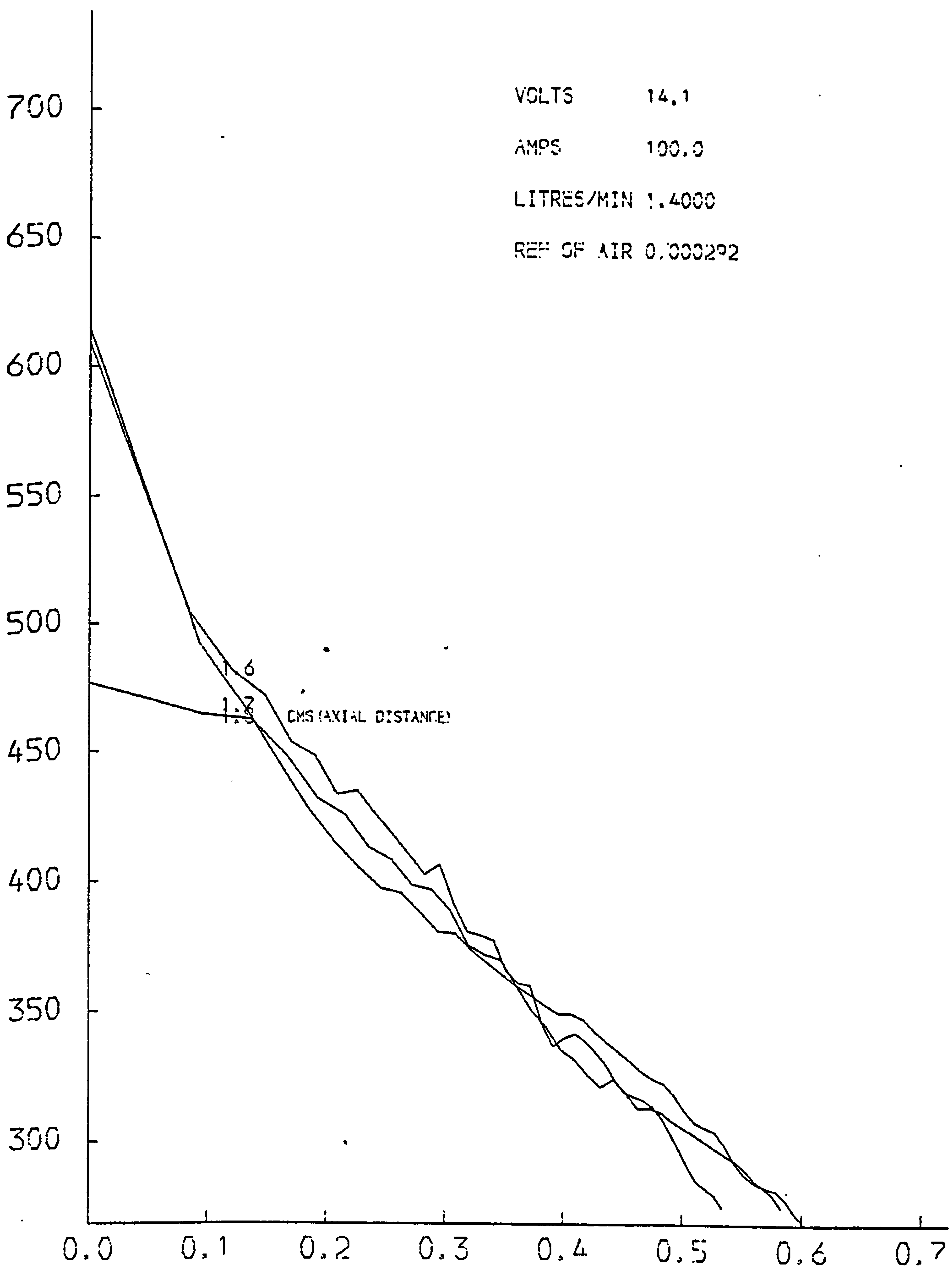

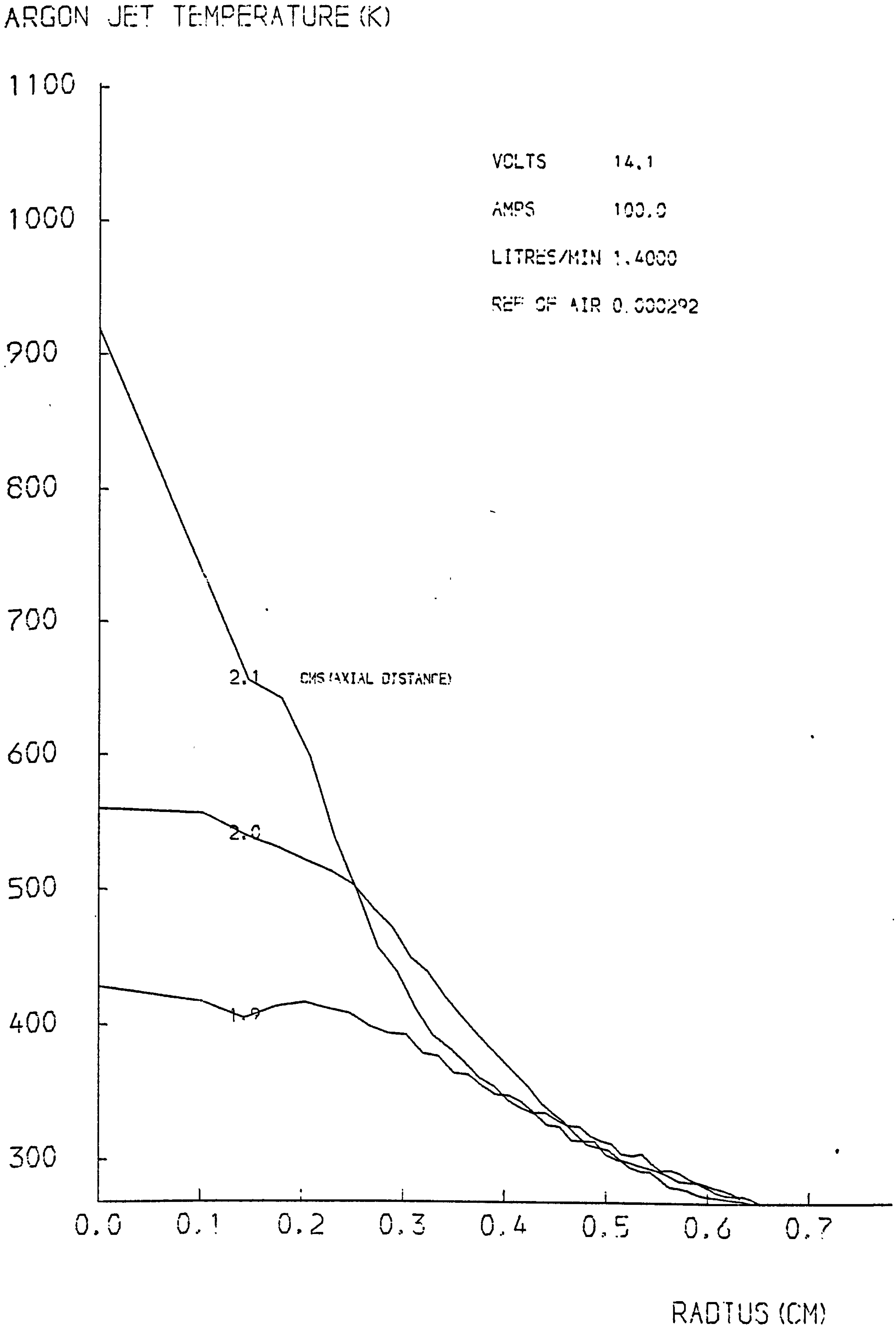

ARGON JET TEMPERATURE (K)
1100
1000
900
800
700
600
500
400
300
VOLTS 14.1
AMPS 100.0
LITRES/MIN 1.4000
REF OF AIR 0.000292
2.1 CMS (AXIAL DISTANCE)
2.0
1.9
0.0
0.1
0.2
0.3
0.4
0.5
0.6
0.7
RADIUS (CM)

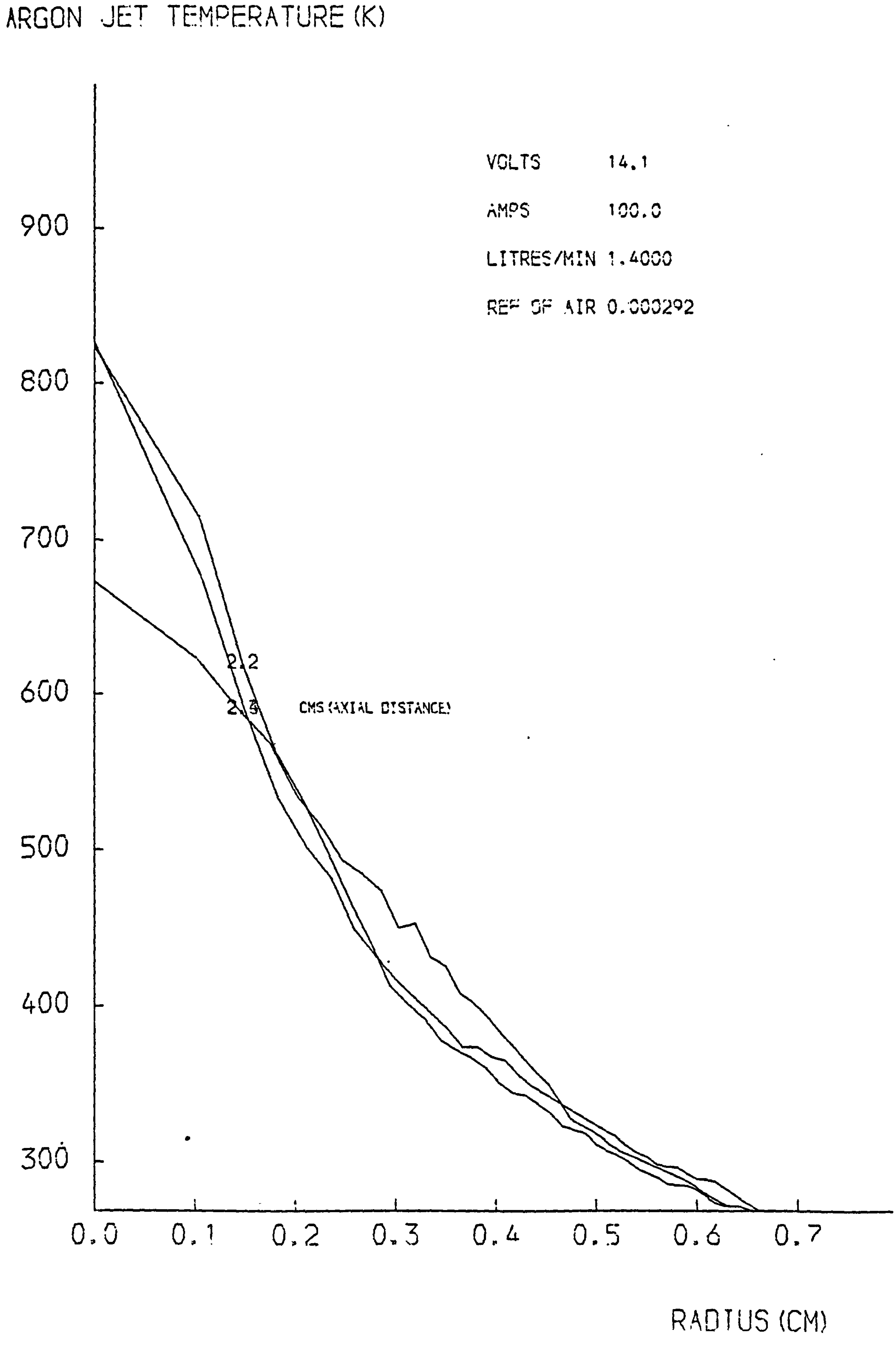

ARGON JET TEMPERATURE (K)
VOLTS 14.1
AMPS 100.0
LITRES/MIN 1.4000
REF OF AIR 0.000292
900
800
700
600
500
400
300
2.2
2.3
CMS (AXIAL DISTANCE)
0.0
0.1
0.2
0.3
0.4
0.5
0.6
0.7
RADIUS (CM)

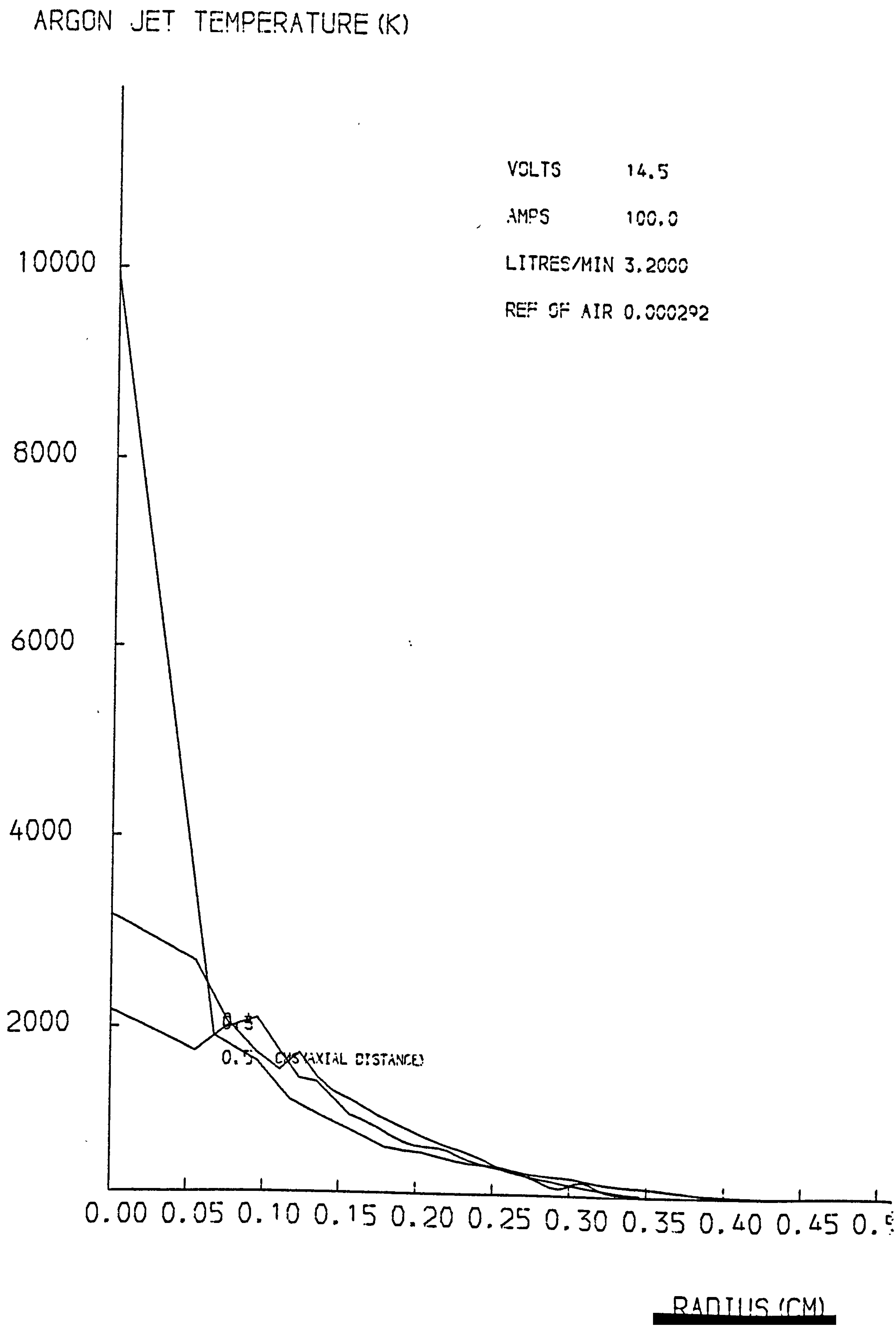
ARGON JET TEMPERATURE (K)
VOLTS 14.5
AMPS 100.0
LITRES/MIN 3.2000
REF OF AIR 0.000292
10000
8000
6000
4000
2000
0.5 CMS (AXIAL DISTANCE)
0.00 0.05 0.10 0.15 0.20 0.25 0.30 0.35 0.40 0.45
RADIUS (CM)

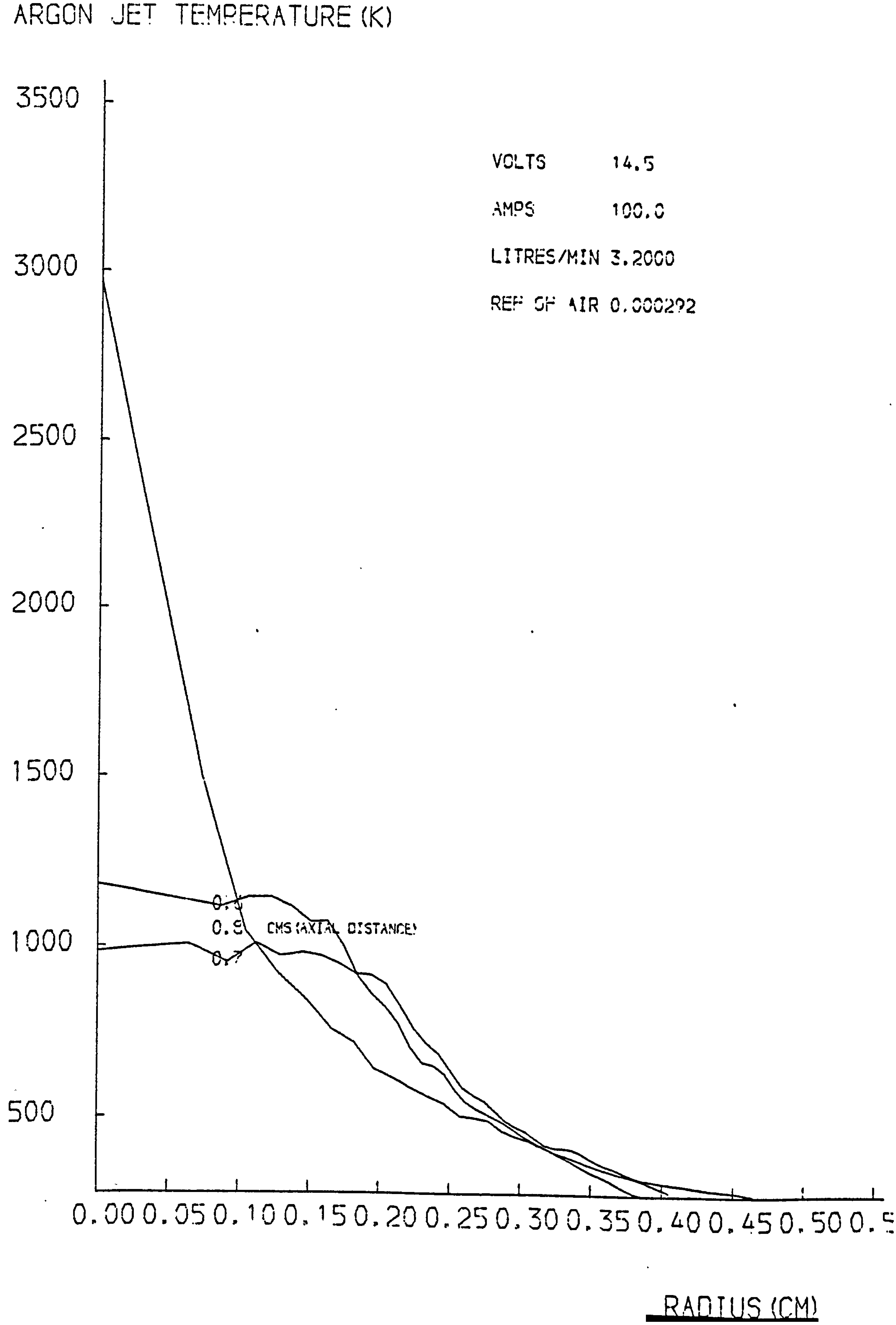
ARGON JET TEMPERATURE (K)
3500
3000
2500
2000
1500
1000
500
VOLTS 14.5
AMPS 100.0
LITRES/MIN 3.2000
0.9 CMS (AXIAL DISTANCE)
0.00 0.05 0.10 0.15 0.20 0.25 0.30 0.35 0.40 0.45 0.50
RADIUS (CM)

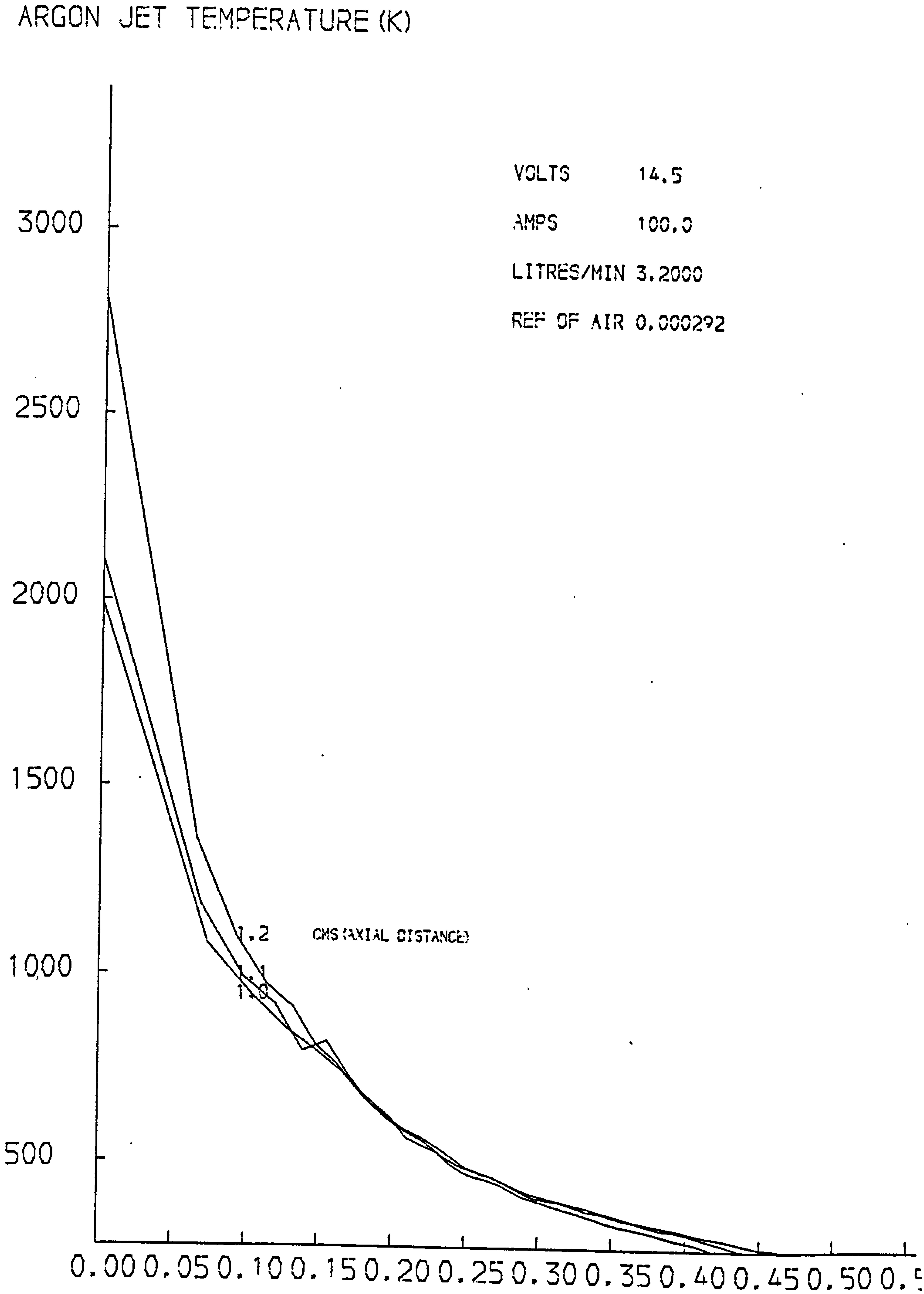
ARGON JET TEMPERATURE (K)
VOLTS 14.5
AMPS 100.0
LITRES/MIN 3.2000
REF OF AIR 0.000292
3000
2500
2000
1500
1000
500
1.2
1.1
1.0
CMS (AXIAL DISTANCE)
0.00 0.05 0.10 0.15 0.20 0.25 0.30 0.35 0.40 0.45 0.50

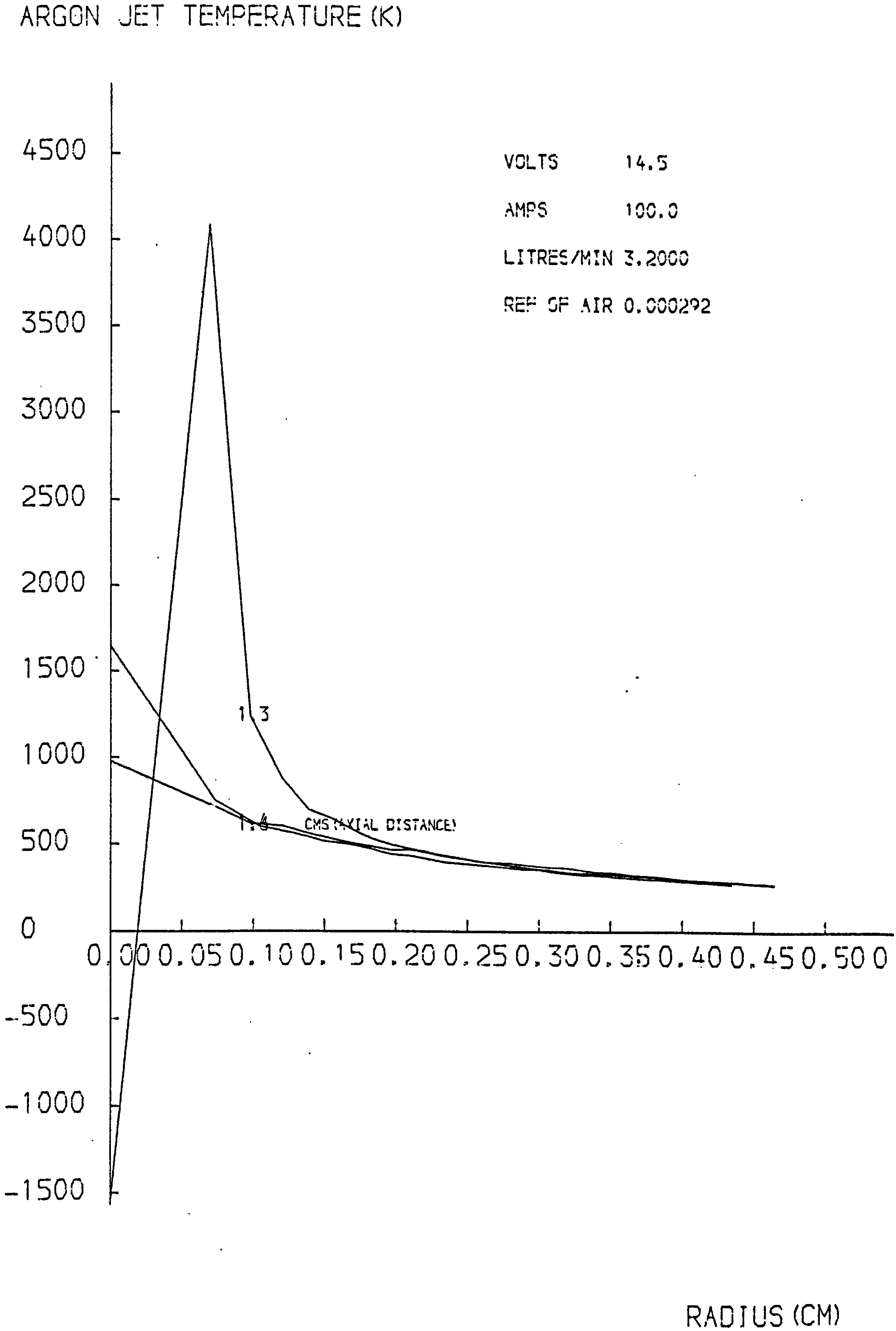

PROGRAMME 710

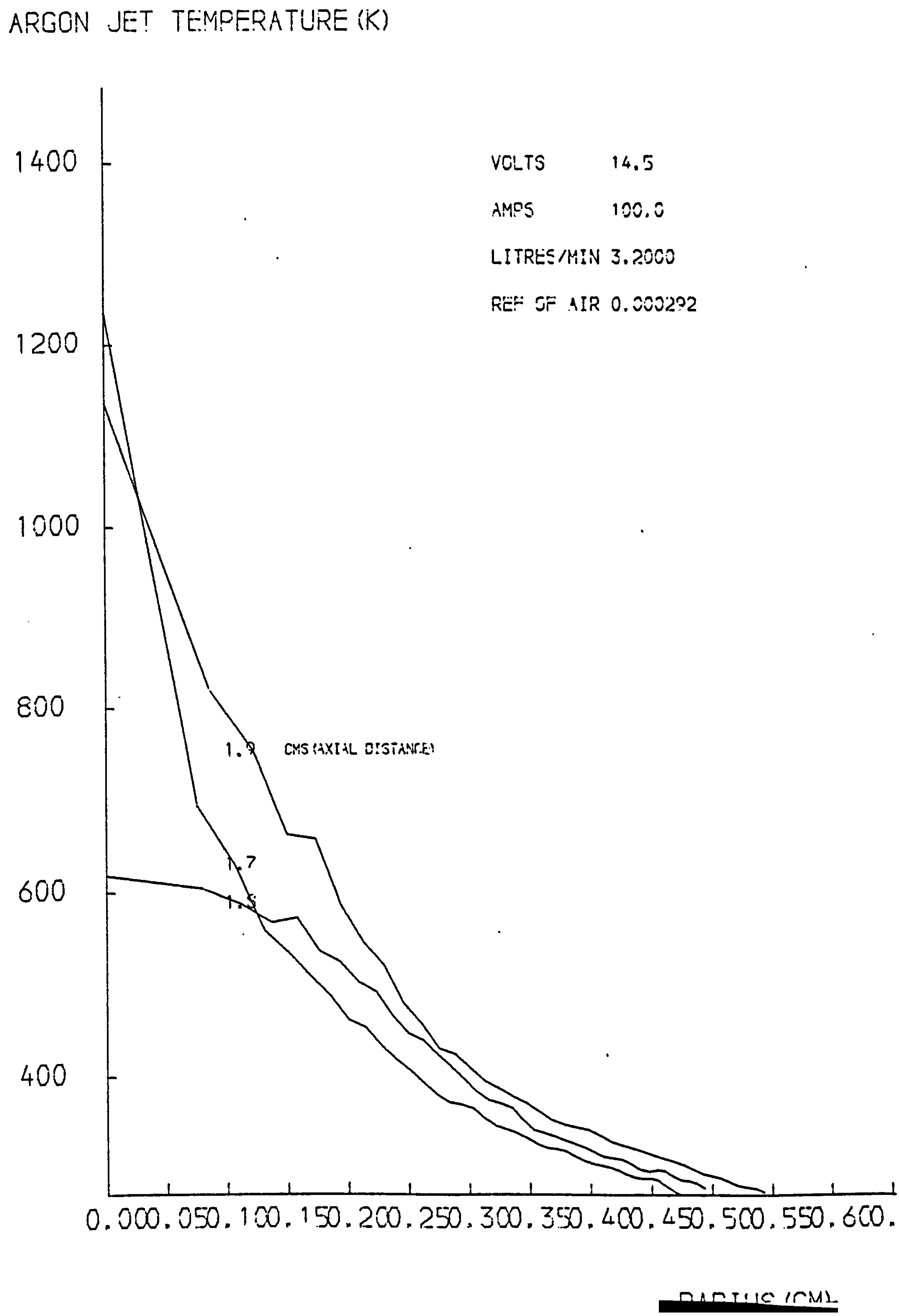

ARGON JET TEMPERATURE (K)
1400
1200
1000
800
600
400
VOLTS 14.5
AMPS 100.0
LITRES/MIN 3.2000
REF OF AIR 0.000292
1.9 CMS (AXIAL DISTANCE)
1.7
1.5
0.00
0.05
0.10
0.15
0.20
0.25
0.30
0.35
0.40
0.45
0.50
0.55
0.60

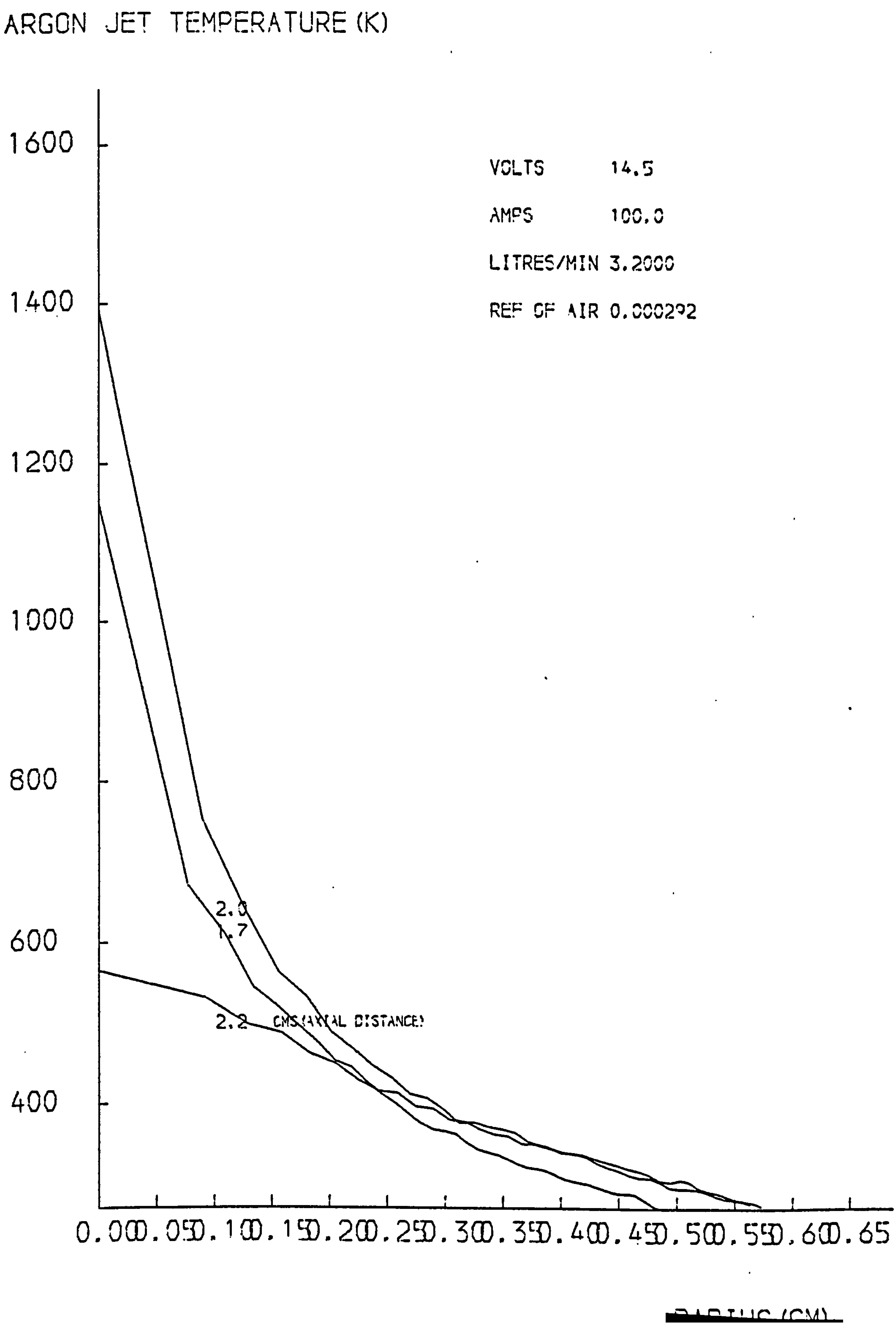
ARGON JET TEMPERATURE (K)
1600
1400
1200
1000
800
600
400
VOLTS 14.5
AMPS 100.0
LITRES/MIN 3.2000
REF OF AIR 0.000292
2.0
1.7
2.2 CMS (AXIAL DISTANCE)
0.00 0.05 0.10 0.15 0.20 0.25 0.30 0.35 0.40 0.45 0.50 0.55 0.60 0.65

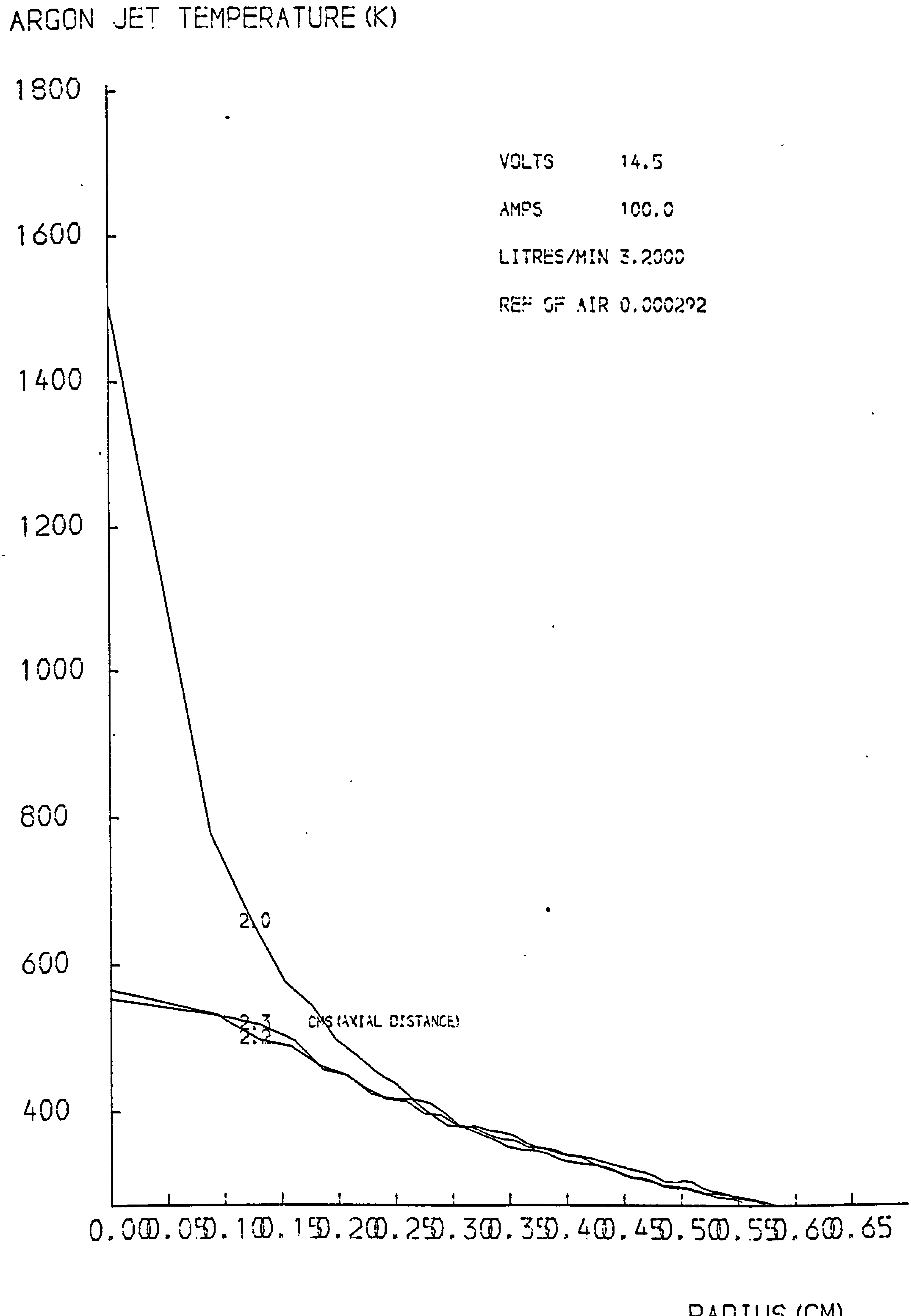
ARGON JET TEMPERATURE (K)
1800
1600
1400
1200
1000
800
600
400
VOLTS 14.5
AMPS 100.0
LITRES/MIN 3.2000
REF OF AIR 0.000292
2.0
2.3
2.2
CMS (AXIAL DISTANCE)
0.00
0.05
0.10
0.15
0.20
0.25
0.30
0.35
0.40
0.45
0.50
0.55
0.60
0.65
RADIUS (CM)

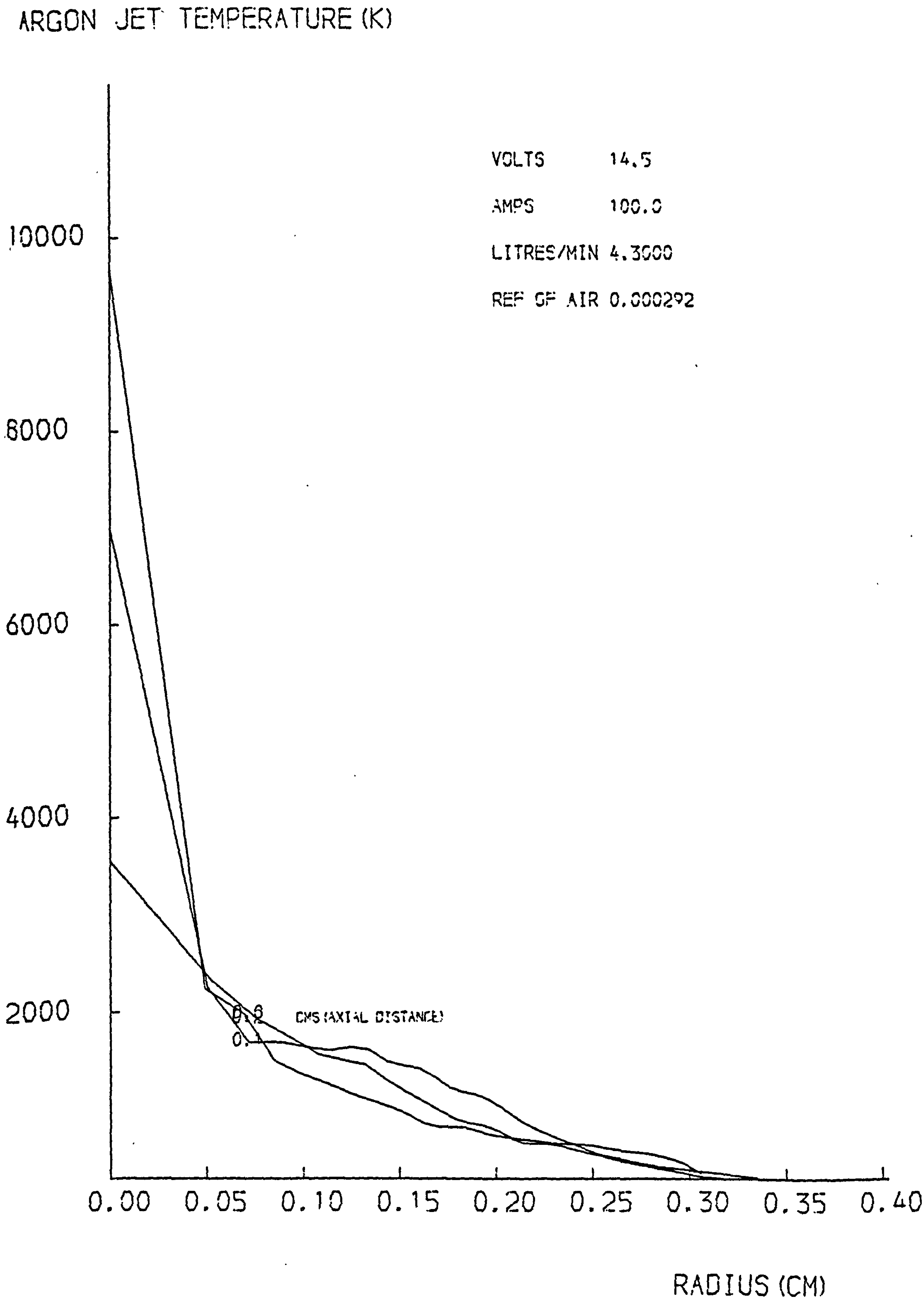
ARGON JET TEMPERATURE (K)
VOLTS 14.5
AMPS 100.0
LITRES/MIN 4.3000
REF OF AIR 0.000292
10000
8000
6000
4000
2000
CMS (AXIAL DISTANCE)
0.00
0.05
0.10
0.15
0.20
0.25
0.30
0.35
0.40
RADIUS (CM)

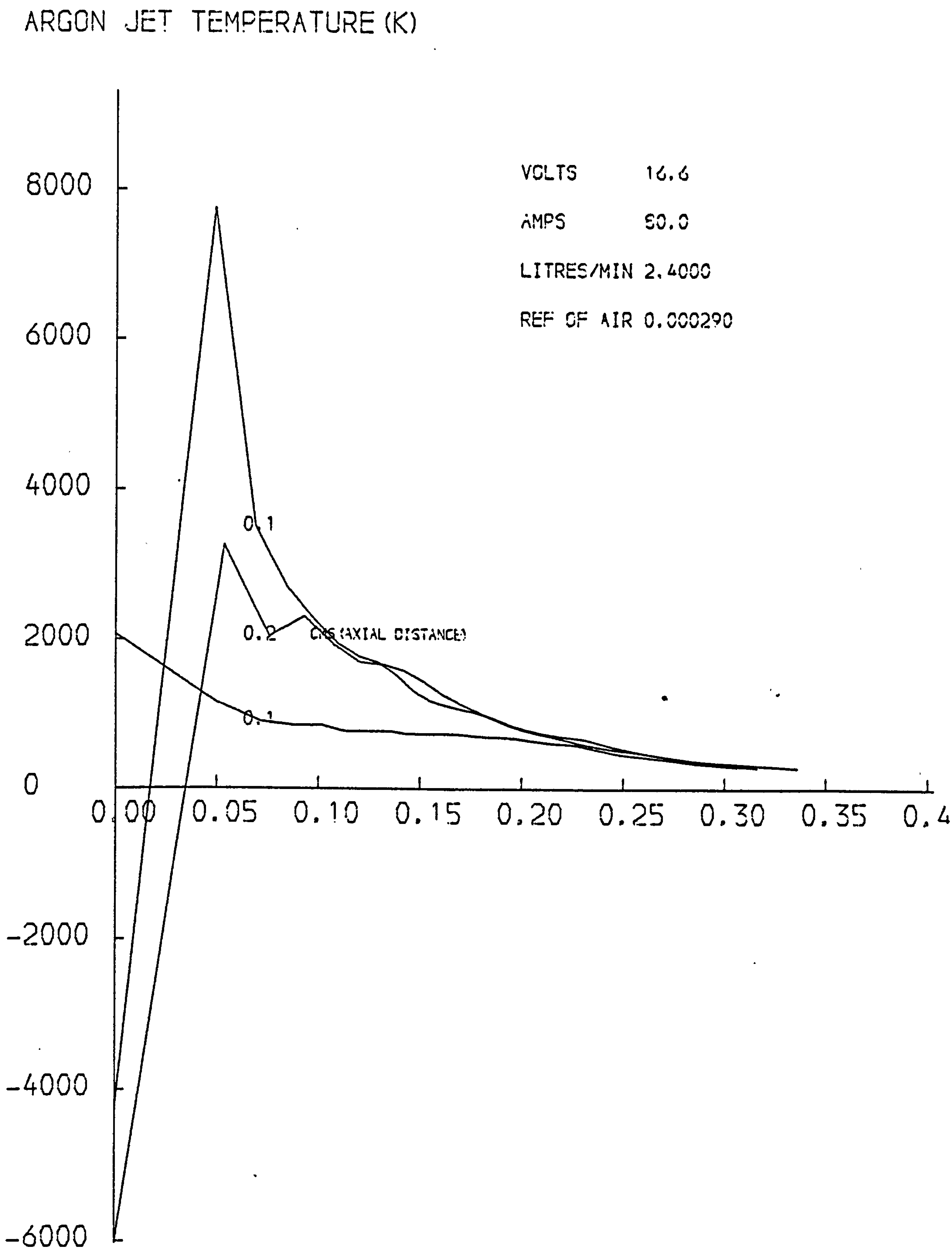
ARGON JET TEMPERATURE (K)
VOLTS 16.6
AMPS 50.0
LITRES/MIN 2.4000
REF OF AIR 0.000290
0.1
0.2
CMS (AXIAL DISTANCE)
0.1
8000
6000
4000
2000
0
-2000
-4000
-6000
0.00 0.05 0.10 0.15 0.20 0.25 0.30 0.35 0.4

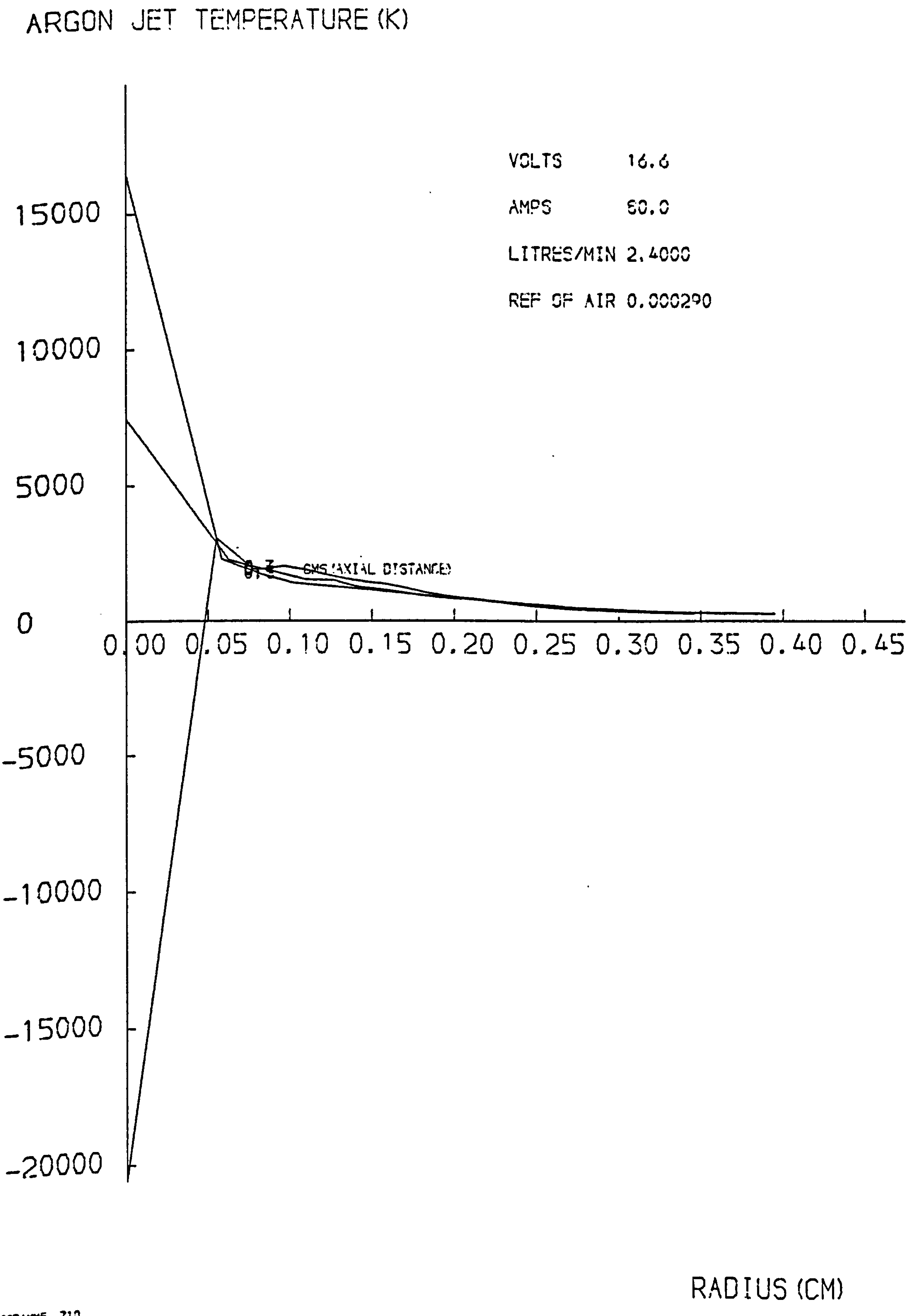
ARGON JET TEMPERATURE (K)
VOLTS 16.6
AMPS 60.0
LITRES/MIN 2.4000
REF OF AIR 0.000290
CMS (AXIAL DISTANCE)
15000
10000
5000
0
-5000
-10000
-15000
-20000
0.00 0.05 0.10 0.15 0.20 0.25 0.30 0.35 0.40 0.45
RADIUS (CM)

[redacted]

TEXT BOUND INTO

THE SPINE

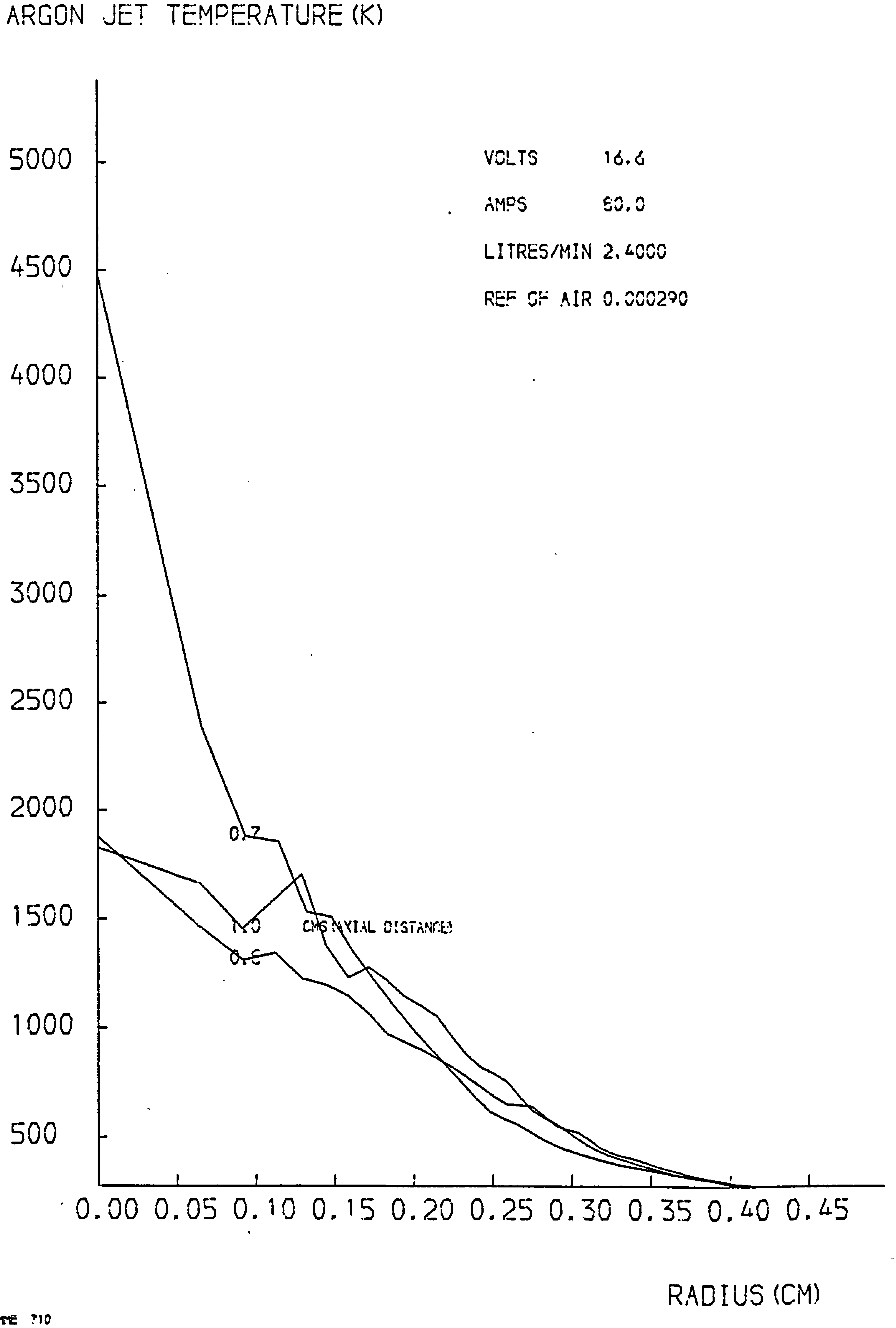

PROGRAMME 710

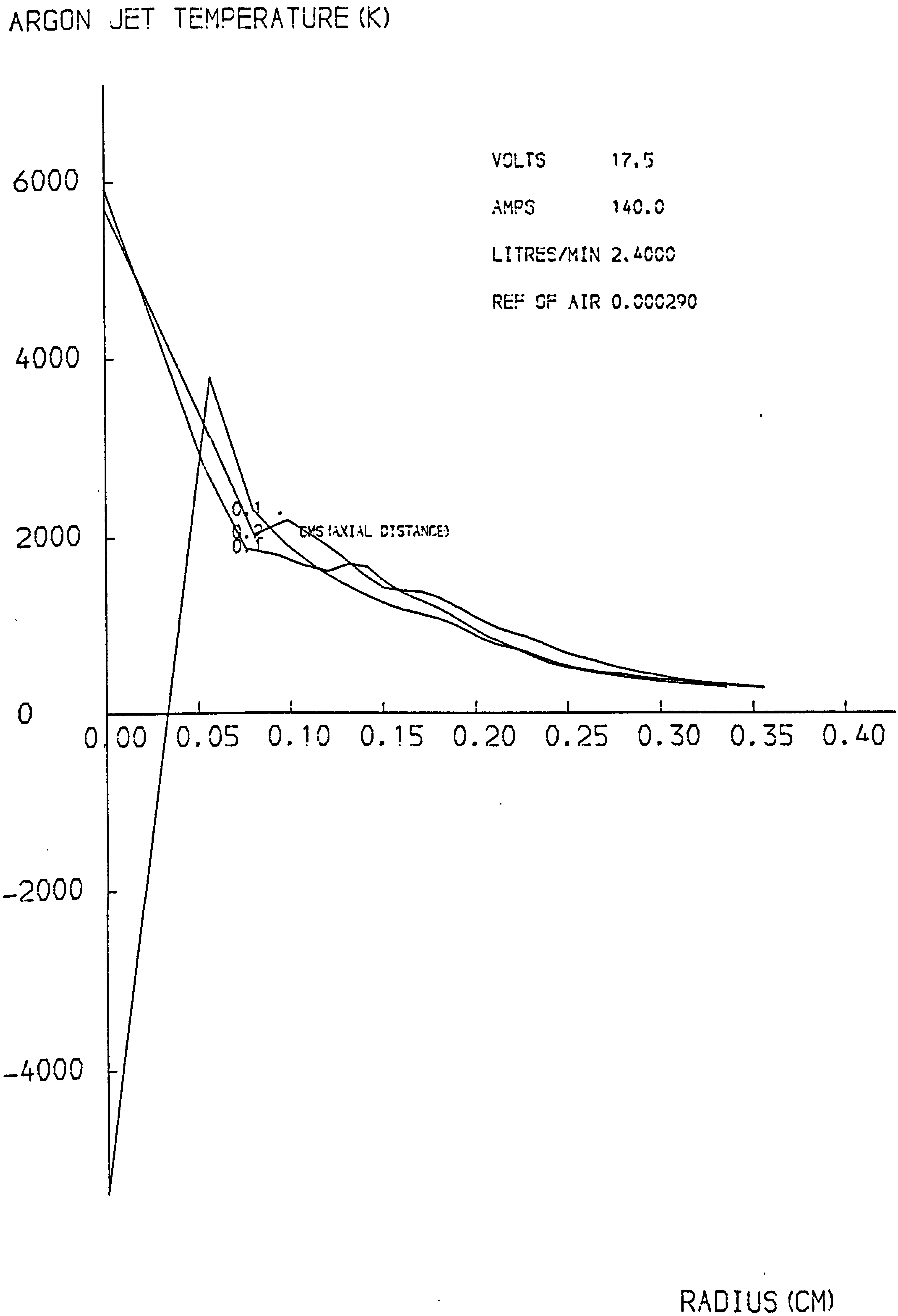
ARGON JET TEMPERATURE (K)
VOLTS 17.5
AMPS 140.0
LITRES/MIN 2.4000
REF OF AIR 0.000290
6000
4000
2000
0
-2000
-4000
0.1
0.2
0.1
CMS (AXIAL DISTANCE)
0.00
0.05
0.10
0.15
0.20
0.25
0.30
0.35
0.40
RADIUS (CM)

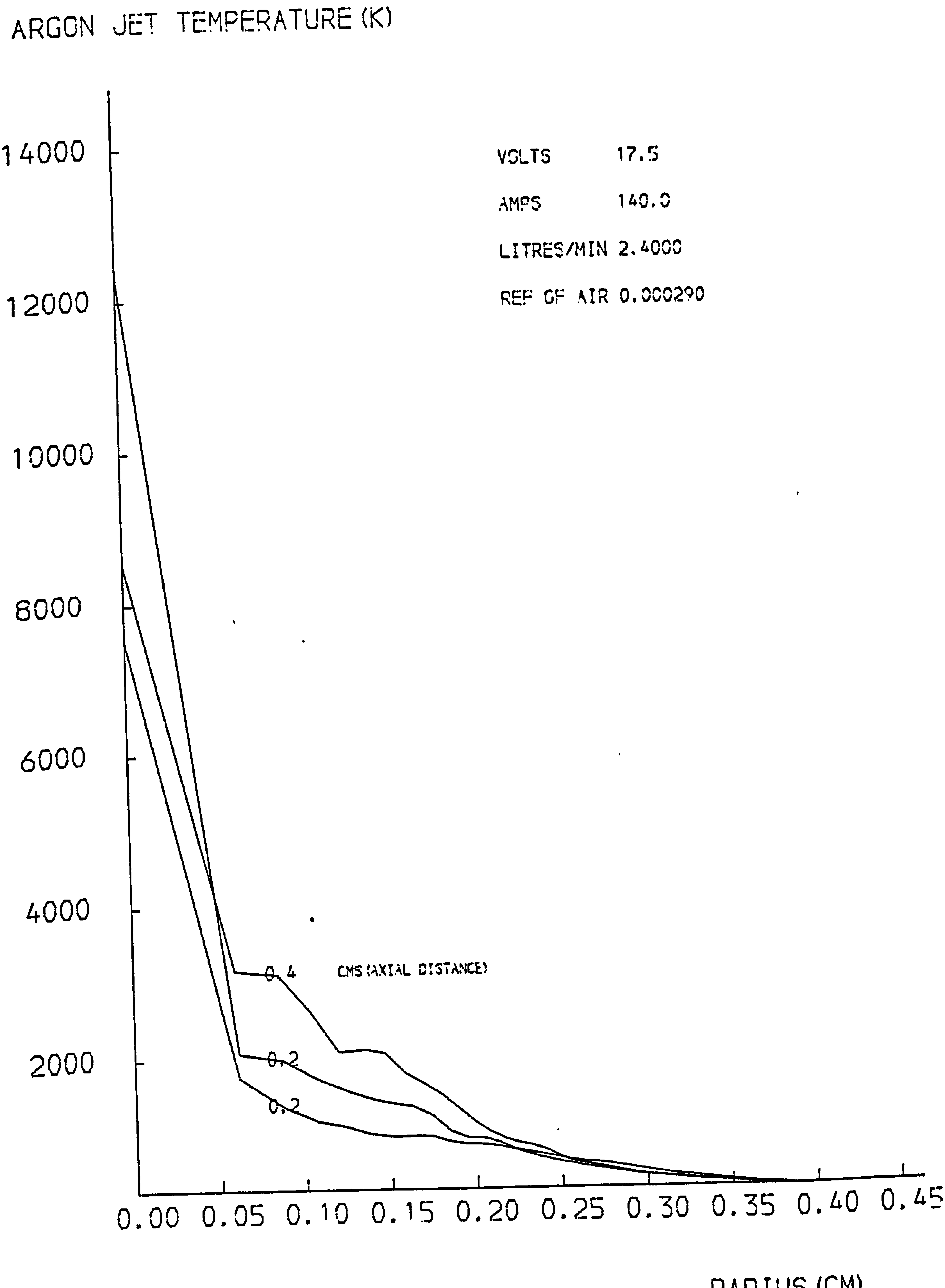
ARGON JET TEMPERATURE (K)
14000
12000
10000
8000
6000
4000
2000
VOLTS 17.5
AMPS 140.0
LITRES/MIN 2.4000
REF OF AIR 0.000290
0.4
CMS (AXIAL DISTANCE)
0.2
0.2
0.00
0.05
0.10
0.15
0.20
0.25
0.30
0.35
0.40
0.45
RADIUS (CM)

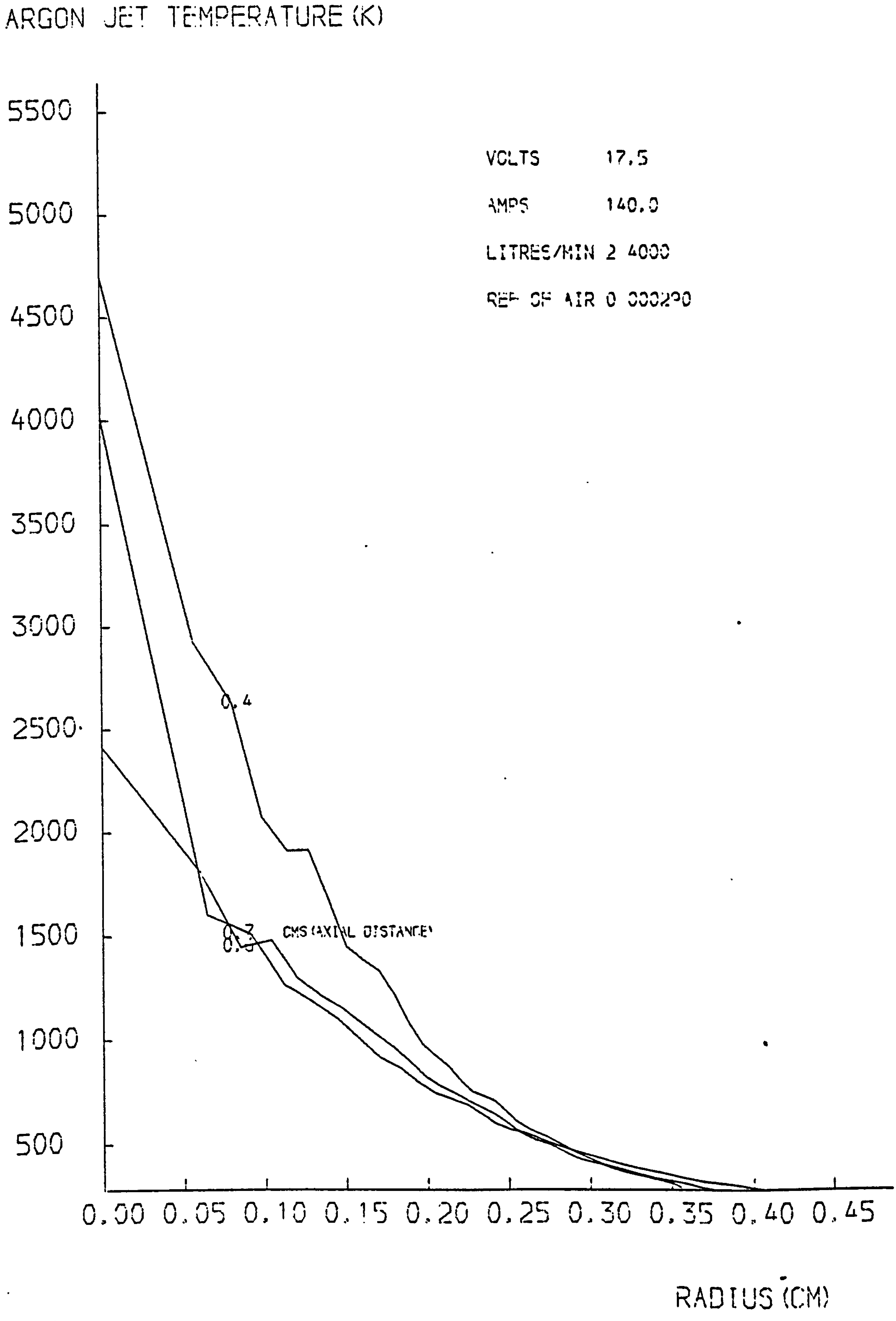

PROGRAMME 210

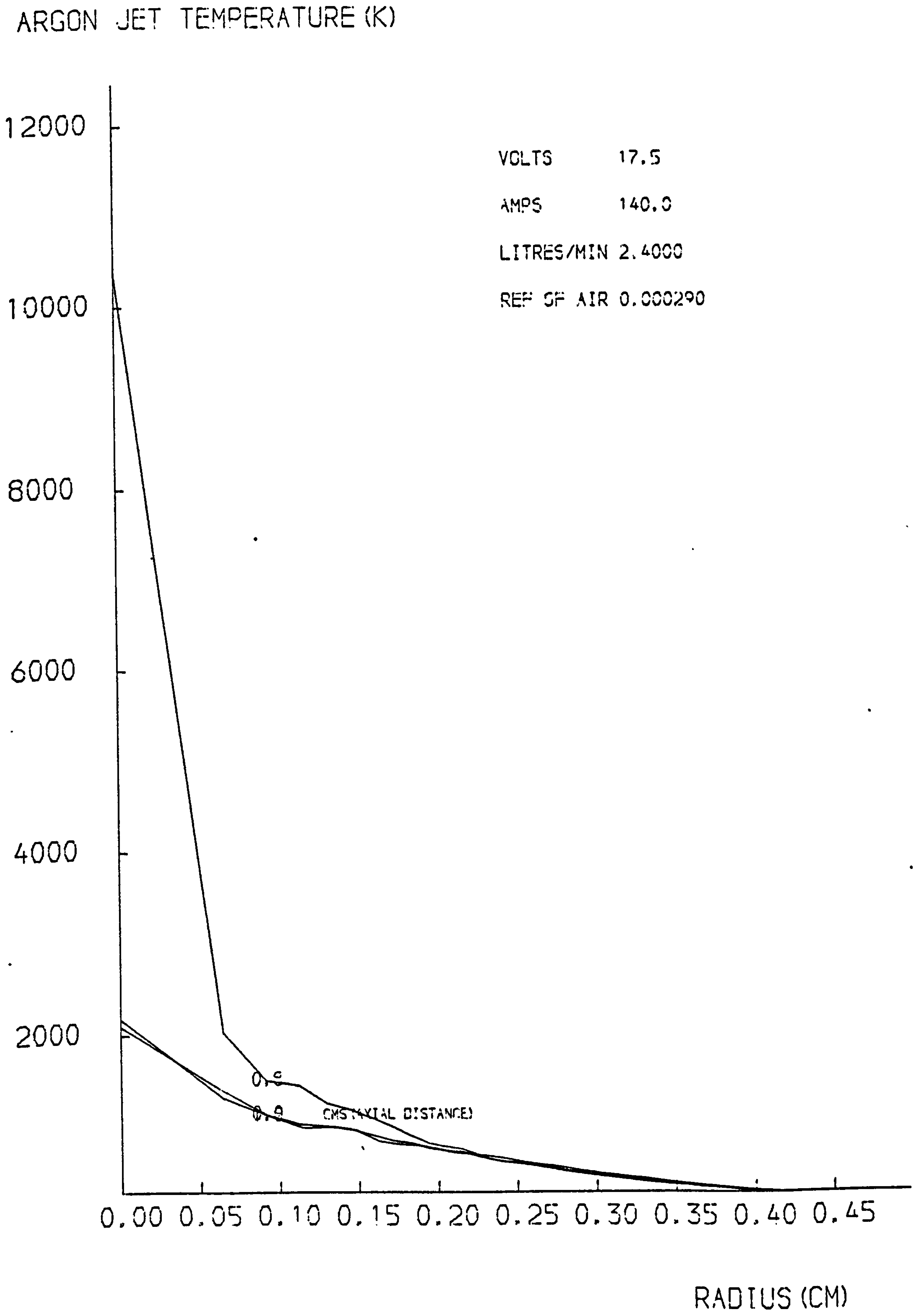
ARGON JET TEMPERATURE (K)
12000
10000
8000
6000
4000
2000
VOLTS 17.5
AMPS 140.0
LITRES/MIN 2.4000
REF OF AIR 0.000290
0.5
0.9
CMS (AXIAL DISTANCE)
0.00 0.05 0.10 0.15 0.20 0.25 0.30 0.35 0.40 0.45
RADIUS (CM)

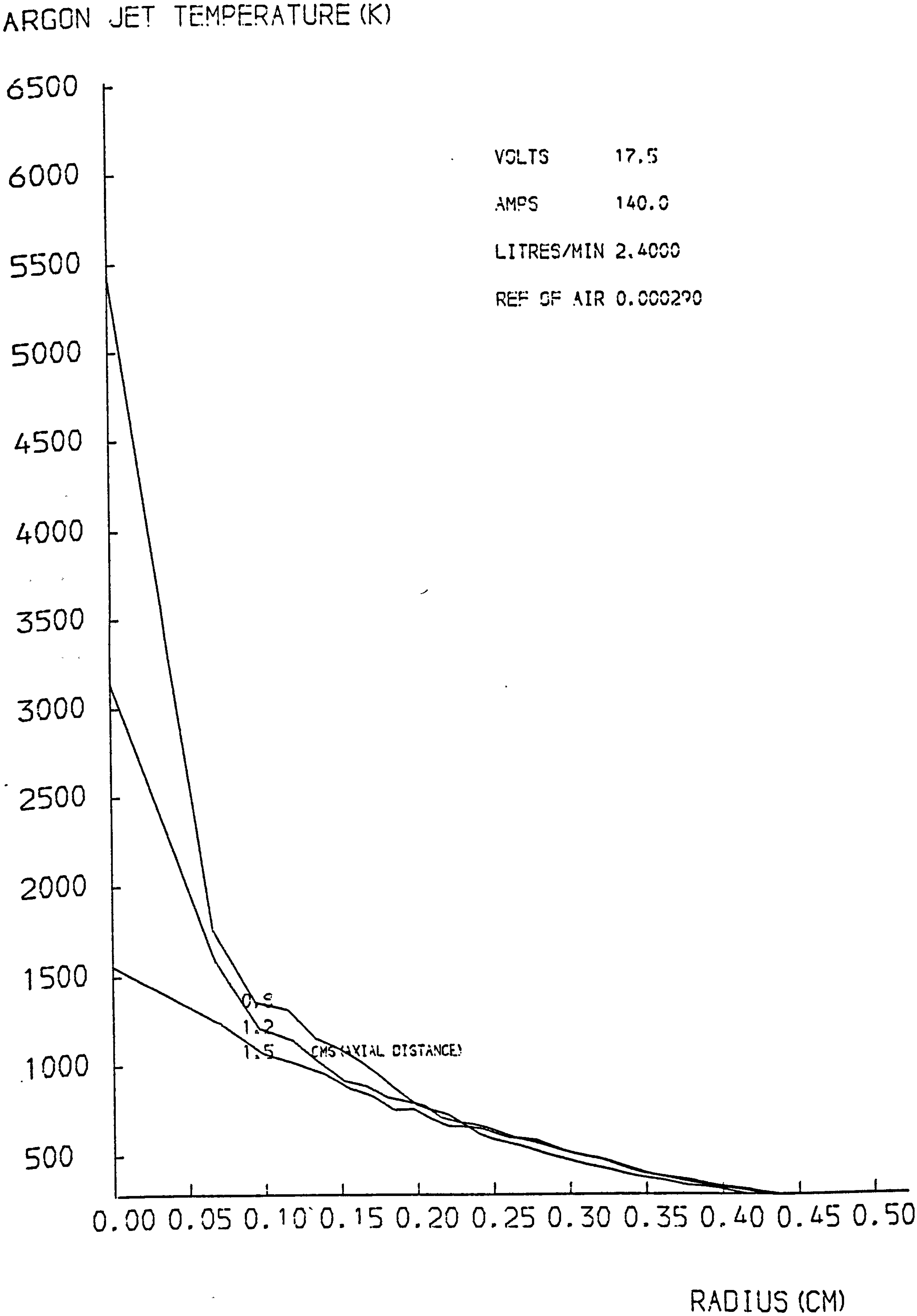

PROGRAMME 710

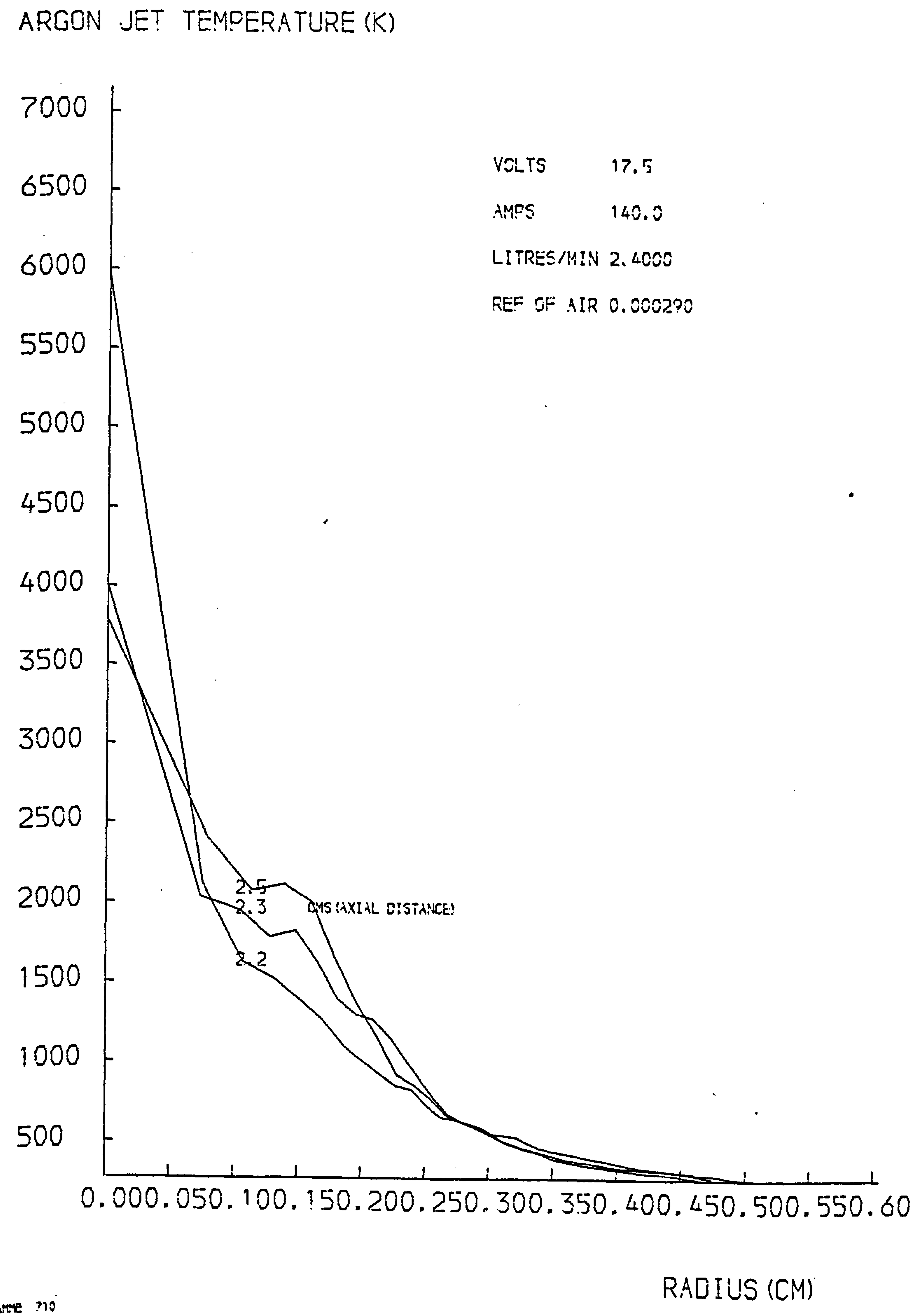

PROGRAMME 710

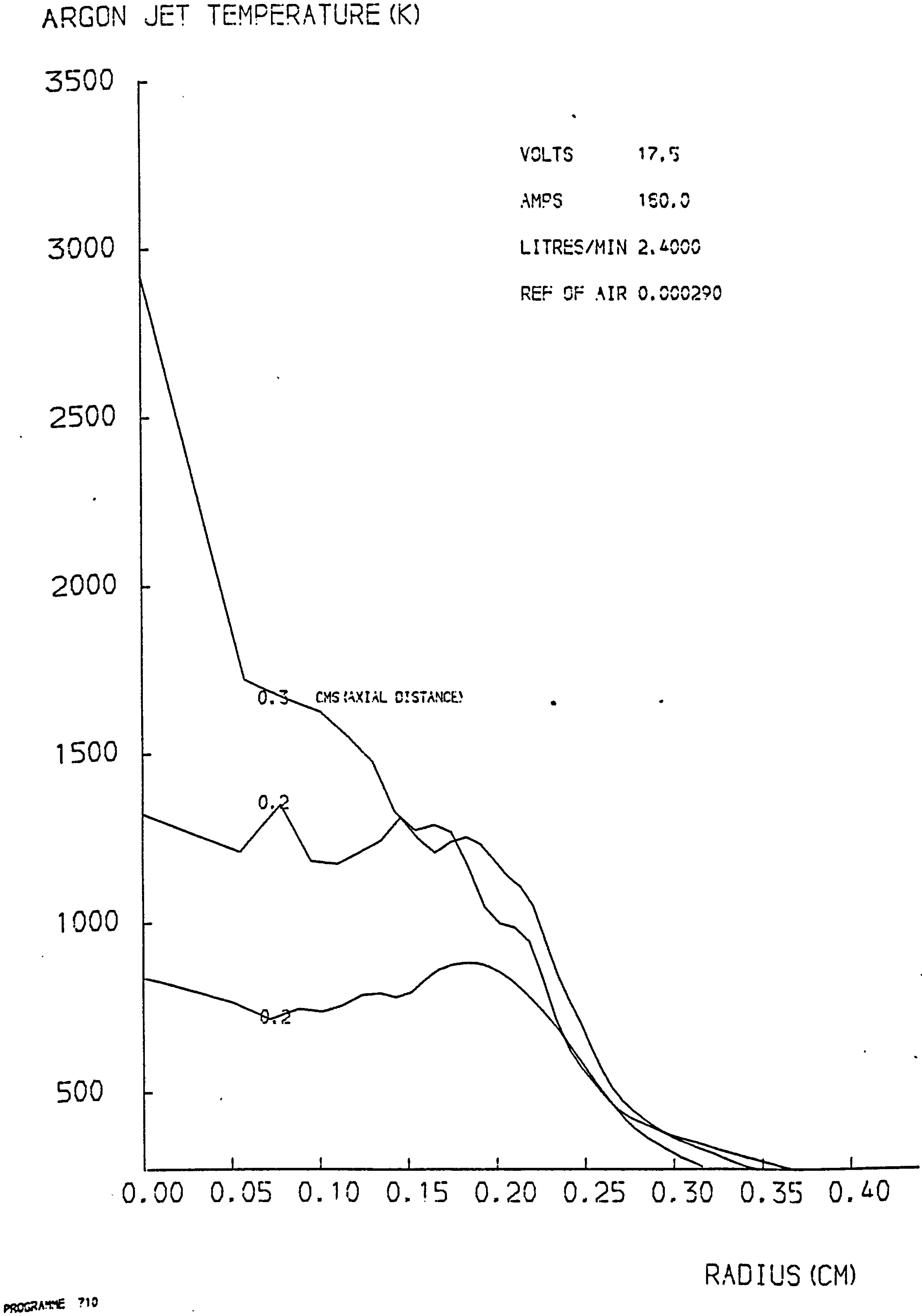
ARGON JET TEMPERATURE (K)
3500
3000
2500
2000
1500
1000
500
VOLTS 17.5
AMPS 160.0
LITRES/MIN 2.4000
REF OF AIR 0.000290
0.3 CMS (AXIAL DISTANCE)
0.2
0.2
0.00 0.05 0.10 0.15 0.20 0.25 0.30 0.35 0.40
RADIUS (CM)
PROGRAMME 710

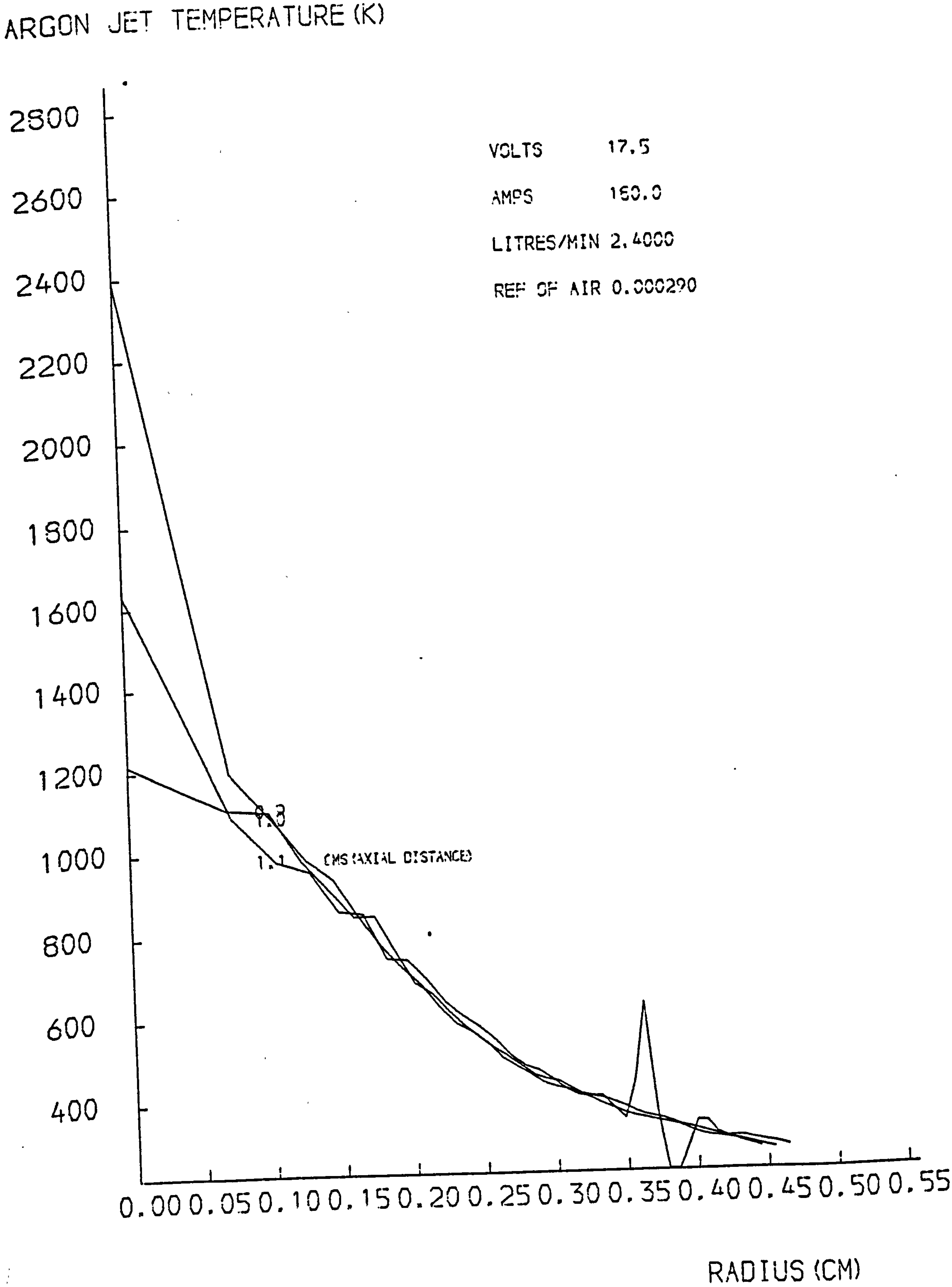

PROGRAMME 710

REFERENCES

1. Hug, W.F., Evans, D., Tankin, R.S. & Cambel, A.B.
   Phys. Rev., 162, 117, 1967.

2. Dobbs, D.
   Transport Properties in High Temperature Gases.
   Ph.D. Thesis, University of Leicester, 1973.

3. Ruddy, M.
   Temperature Measurements in an Argon Plasma Jet.
   Ph.D. Thesis, University of Leicester, 1975.

4. Ascoli-Bartoli, U.
   in Physics of Hot Plasmas.
   Ed. Rye and Taylor (Oliver and Boyd), 1970.

5. Ladenburg, R.W. (ed)
   Physical Measurements in Gas Dynamics and Combustion.
   Part 1 (Oxford), 1955.

6. Martellucci, S.
   Supplemento Al Nuovo Cimento.
   5, 642, 1967.

7. Ladenburg, R., Winkler, J. & Van Voorhis, C.C.
   Phys. Rev., 73, 1359, 1948.

8. Schottky, W.
   Z. f. Phys., 31, 163, 1925.

9. Czernichowski, A.
   Interferometric Determination of Temperature in a Laminar Jet of Neon or Argon Plasma.
   Acta Physica Polonica, A40, 283, 1971.

10. Harker, K.J.
    Use of Scanning Slits for obtaining the Current Distribution in Electron Beams.
    J. App. Phys., 28, 1354, 1958.

11. Longhurst, R.S.
    Geometrical and Physical Optics.
    (Longmans) 1967.

12. Radtke, R., Gunther, K., Ulbricht, R.
    Interferometric Determination of Electron Density in High Pressure Hydrogen Arc. 1. Calculation of Refractive Index.
    J. Phys. D., 13, 1-7, 1980.

13. Sturrock, J.
    The Estimation of Temperature Profiles in an Argon Plasma Jet.
    Unpublished M.Phil. Thesis, University of Leicester.

14. Lederman, S., Celentaw, A., Glaser, J.
Temperature, Concentration and Velocity in Jets, Flames and Shock Tubes.
Phys. Fluids (USA), 22, 1065-72, 1979.

15. Metzger, D.E., Grochowsky, L.P.
Heat Transfer of Impinging Jet on Rotating Disc.
Trans. ASME Ser. C (USA), 99, 663, 1977.

16. Merskirch, W.
Current Problems of Optical Interferometer used in Experimental Gas Dynamics.
AGARD Conference Proceedings, No. 193 on Applications of Non-Intrusive Instrumentation in Fluid Flow Research p.24, 1976.

17. Ditchborn, R.W.
Light (Academic) 1976.

18. C.R.C. Handbook of Chemistry and Physics.
Ed. R.C. Weast (C.R.C. Press) 1977.

19. Mitchner, M. & Kruger, C.H.
Partially Ionised Gases.
(Wiley) 1973.

20. Barnett, M.E.
The Physical Theory of Image Formation, with Applications.
Proceedings of Imperial College Applied Optics Summer Course, 1976.

21. Zehnder, L.
Zeitschr.f.Instrkde, 11, 275, 1891.

22. Mach, L.
Zeitschr.f.Instrkde, 12, 86, 1892.

23. Maxwell, R.W. & Ruddy, M.J.
Volt-Ampere Characteristics of a Plasma Torch.
University of Leicester, Engineering Dept., Internal Report No. 70-9, 1970.

24. Bennet, F.D. & Kahl, G.D.
J. Opt. Am., 43, 71, 1953.

25. Lipson, S.G. & Lipson, H.
Optical Physics (Cambridge) 1969.

26. Griem, H.R.
Plasma Spectroscopy (McGraw-Hill) 1964.

27. Dowd, A. & Maxwell, R.W.
Temperature in an Impinging Argon Jet.
Proc. 5th International Conference on Gas Discharges, p.67, 1978.

28. Tourin, R.H.
Spectroscopic Gas Temperature Measurements.
(Elsevoir) 1966.

29. Pearce, W.J.
Optical Spectrometric Measurements of High Temperatures.
(Chicago Press) 1961.

30. Dowson, M., Maxwell, R.W. & Ruddy, M.
An Abel Transformation.
Leicester University, Engineering Dept., Internal Report, 1971.

31. Sonntag, R. & Von Wylen, G.
Statistical Thermodynamics.
(Wiley) 1966.

32. Denbeigh, K.G.
Principles of Chemical Equilibrium.
(Cambridge) 1963.

33. Buckingham, A.D.
The laws and applications of Thermodynamics.
(Pergamon Press) 1964.

TEMPERATURE IN AN IMPINGING ARGON JET

Amanda Dowd* and R.W. Maxwell

University of Leicester, UK

INTRODUCTION

To elucidate the mechanism of mass and energy transfer in high energy processes - such as electric arcs and plasma jets - measurements of temperature profiles are necessary. In the present work an argon plasma jet impinged on a cooled metal surface in an air environment. At high power inputs (15 kW) and in hot regions (> 5000 K) of the gas near to the jet orifice, temperatures may be estimated by spectroscopic techniques (ref.4). Nearer to the cooled surface when spectral line intensities are low interferometric techniques (ref.5) may be used to estimate the temperature of the hot gas; in the present work flow rates and power inputs were chosen to give fringe displacements - amenable to measurement with available apparatus - which could be used to estimate temperature gradients (and convective heat transfer coefficient) near to the cool surface.

APPARATUS

The plasma torch and cool surface, shown in Fig.2, were placed in one limb of a Mach-Zehnder interferometer with an optical arrangement shown in Fig.1. The plasma torch was a modified Gerdien arc (ref.3), orifice diameter 0.5 and the surface on which the jet impinged was a water cooled copper cylinder, radius 4 cm, rotating up to 33 rpm , mounted 3 cms from the orifice of the torch. The torch head was positioned on the minor axis of the elliptical field of view of the interferometer.

The apparatus was illuminated by a 5mW He-Ne laser and the mirrors and splitters of the interferometer were adjusted to give horizontal fringes (Fig.3) which were recorded on Kodak 2475 film in a Pentak 35 mm camera. The camera had no lens and an external shutter was fitted and situated at the focal point of a collimating lens which collected radiation from the interferometer. An exposure time of 1/500 sec was used and the aperature of the shutter was adjusted to give suitable contrast. Bench marks were placed in one limb of the interferometer to allow scaling of the measurements taken from the photographs. At high power inputs the intensity of the arc caused fogging on the photographic plate and to reduce this a (15 A° bandpass) filter was placed in front of the shutter.

RESULTS

Photographs were taken of the fringe shifts (shown in Fig.4) at various power inputs to,

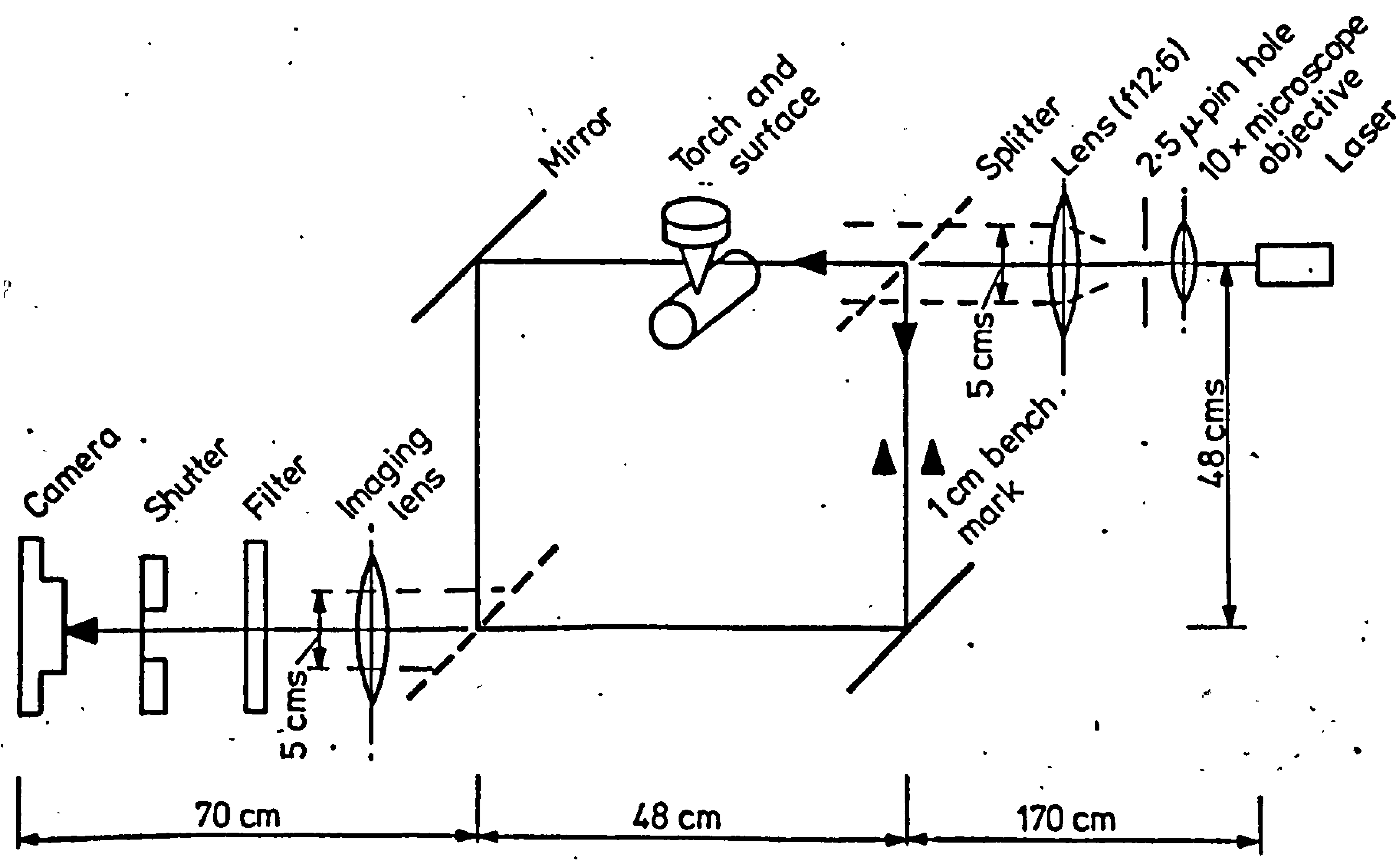

Fig. 1 Diagram of experimental rig

* now at Rank Taylor Hobson, Leicester.

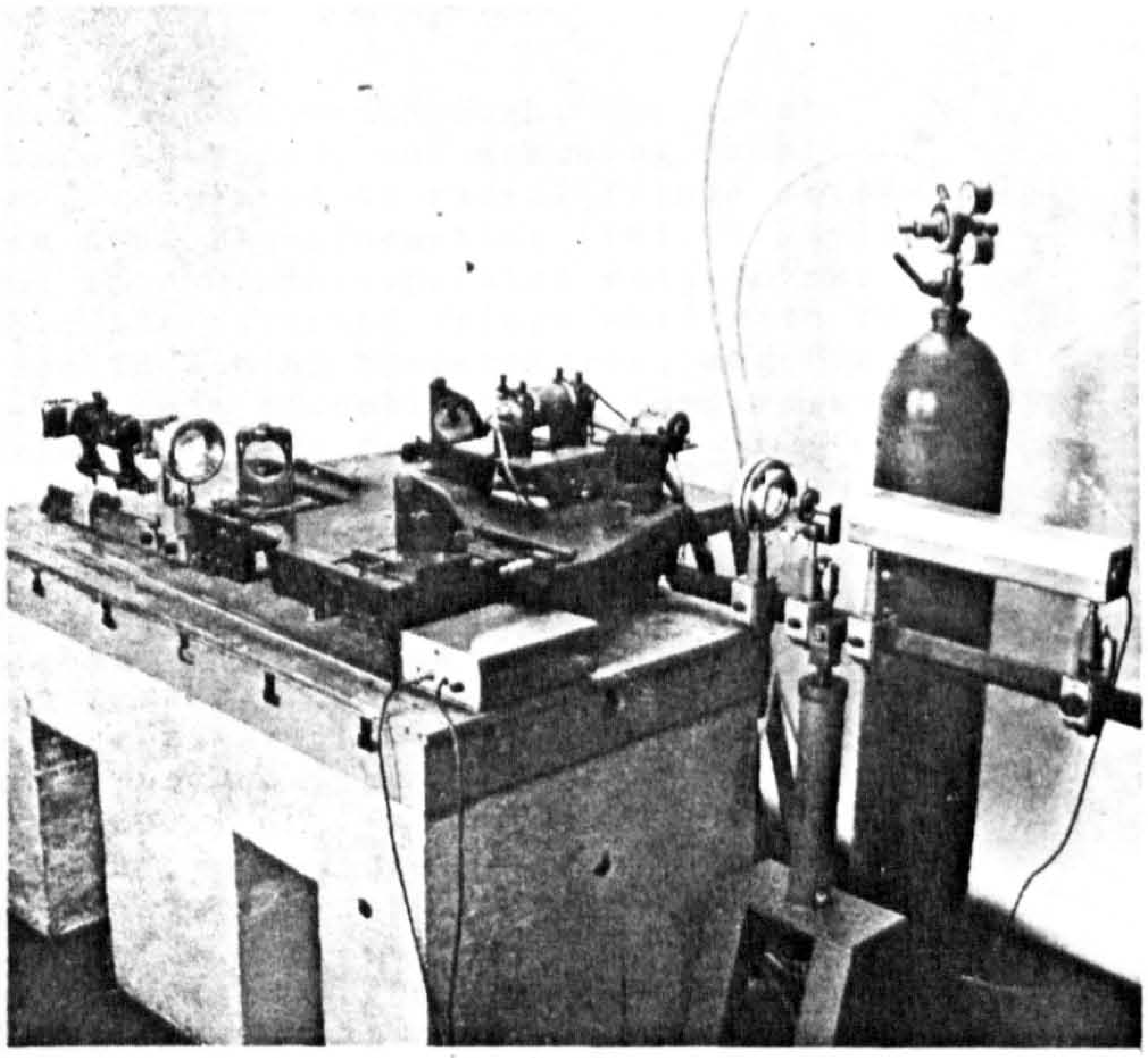

FIG. 2 ARRANGEMENT OF APPARATUS

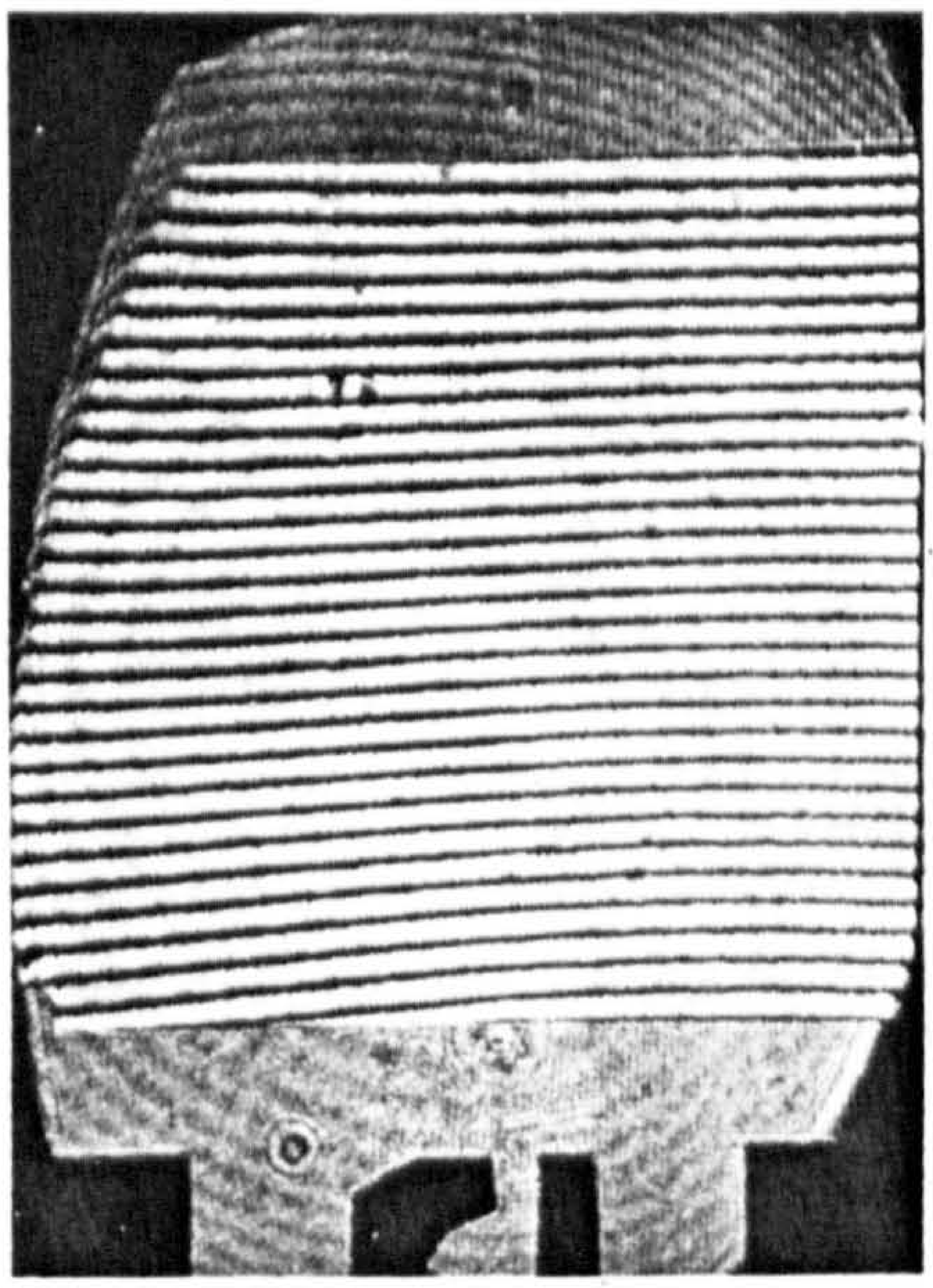

FIG. 3 UNDISTURBED FRINGES

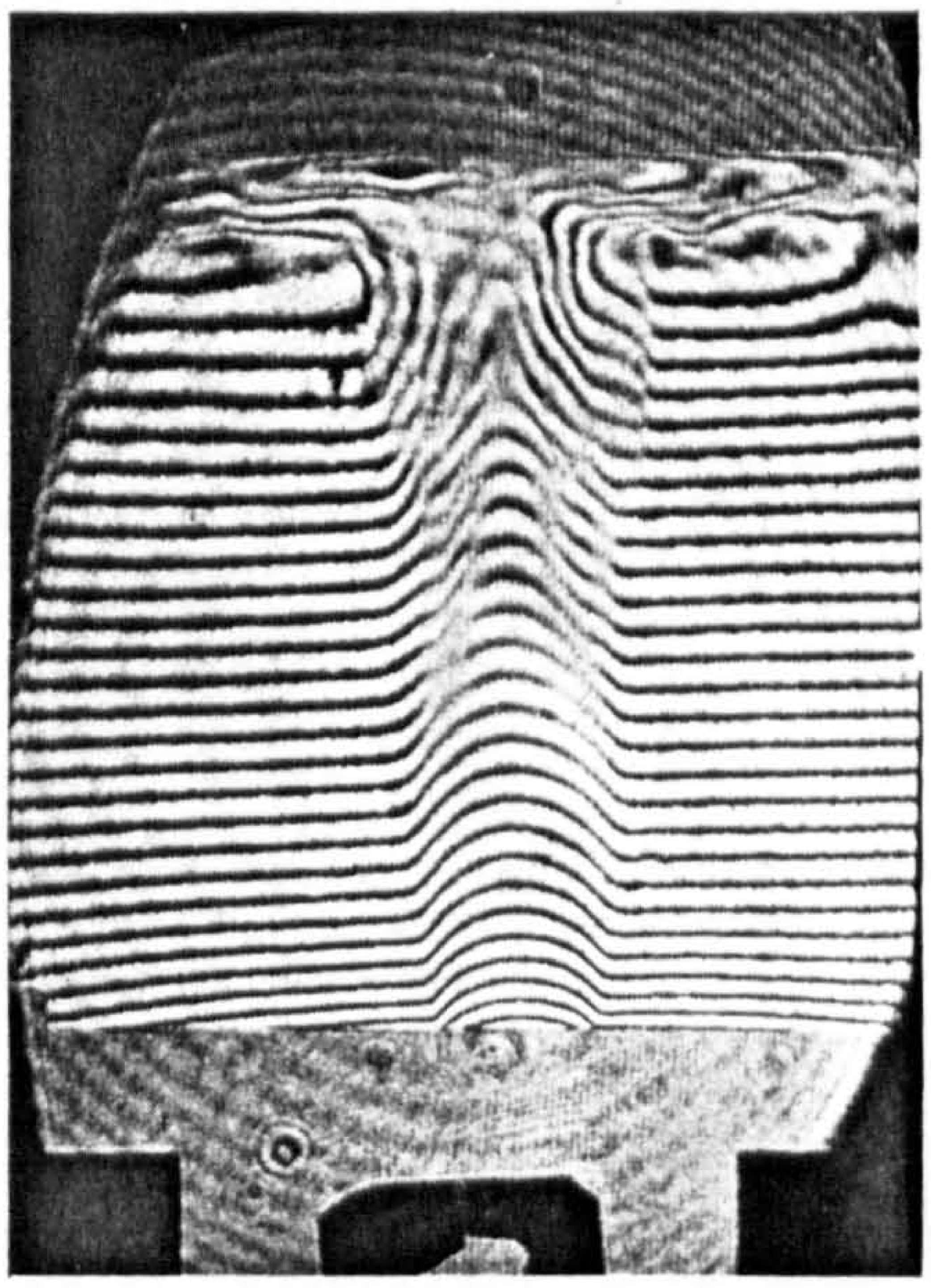

FIG. 4 FRINGE SHIFTS (RESULTS IN FIG. 5)

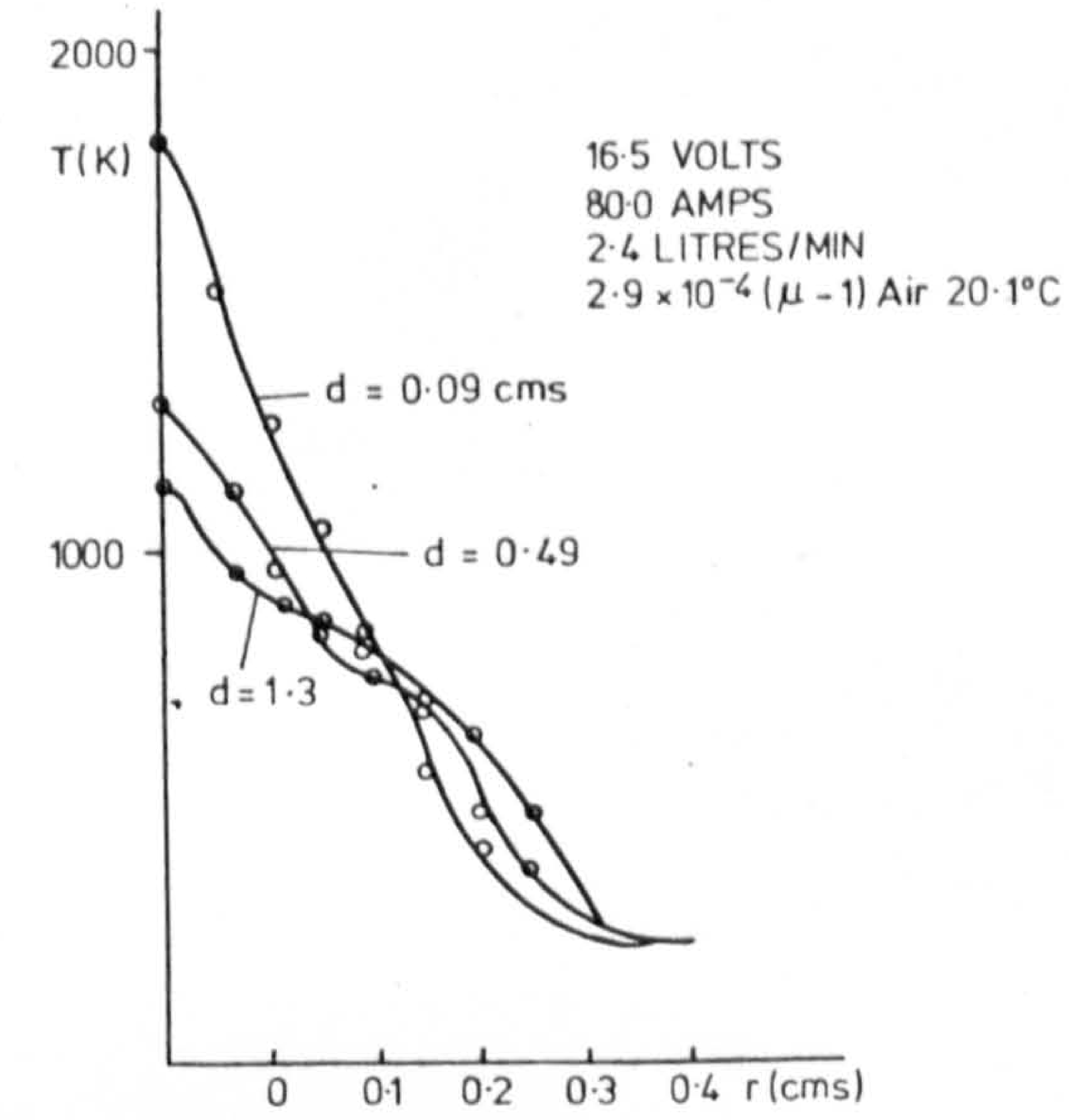

FIG. 5 RADIAL TEMPERATURE DISTRIBUTIONS

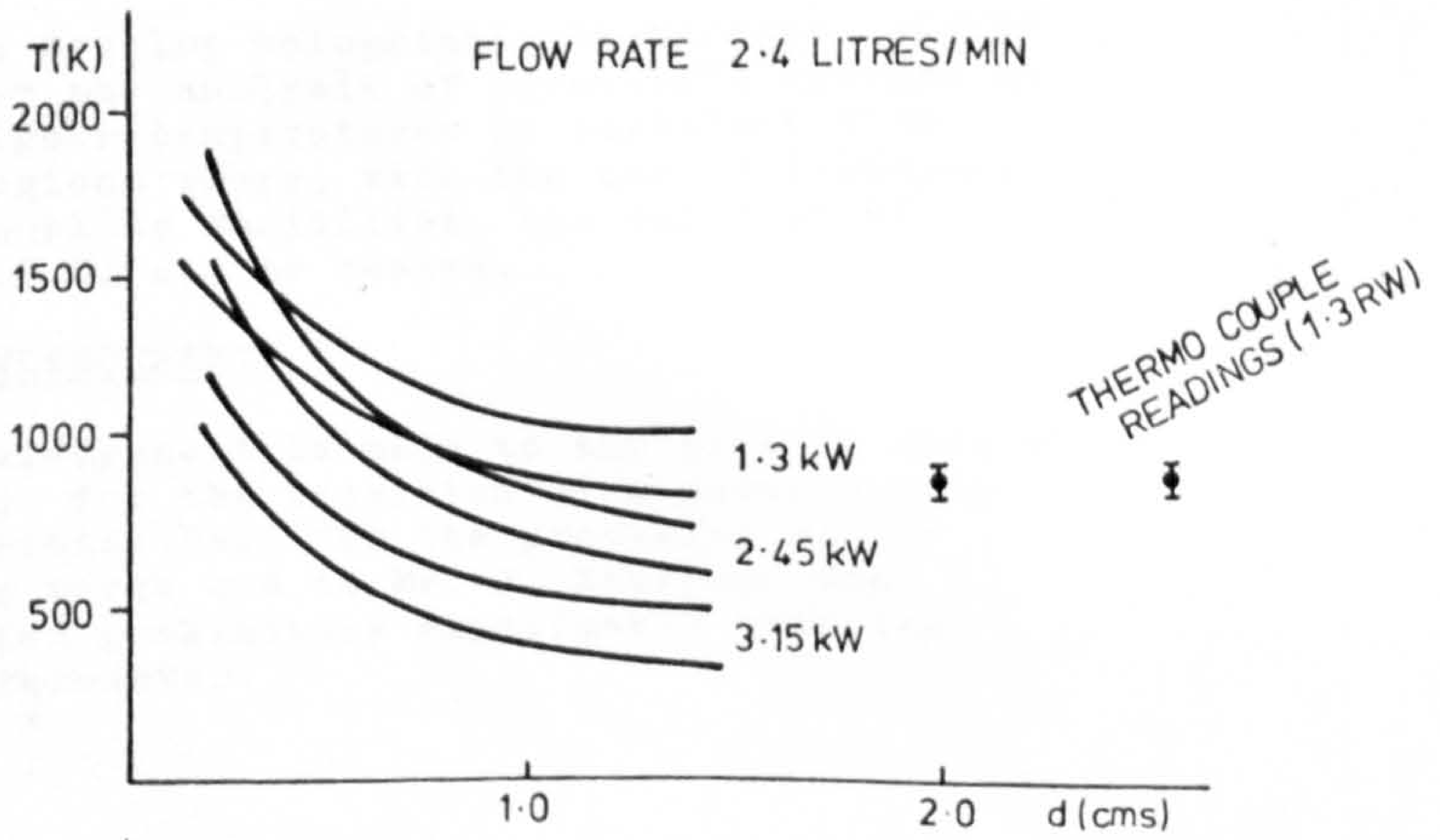

FIG. 6 AXIAL TEMPERATURE DISTRIBUTIONS

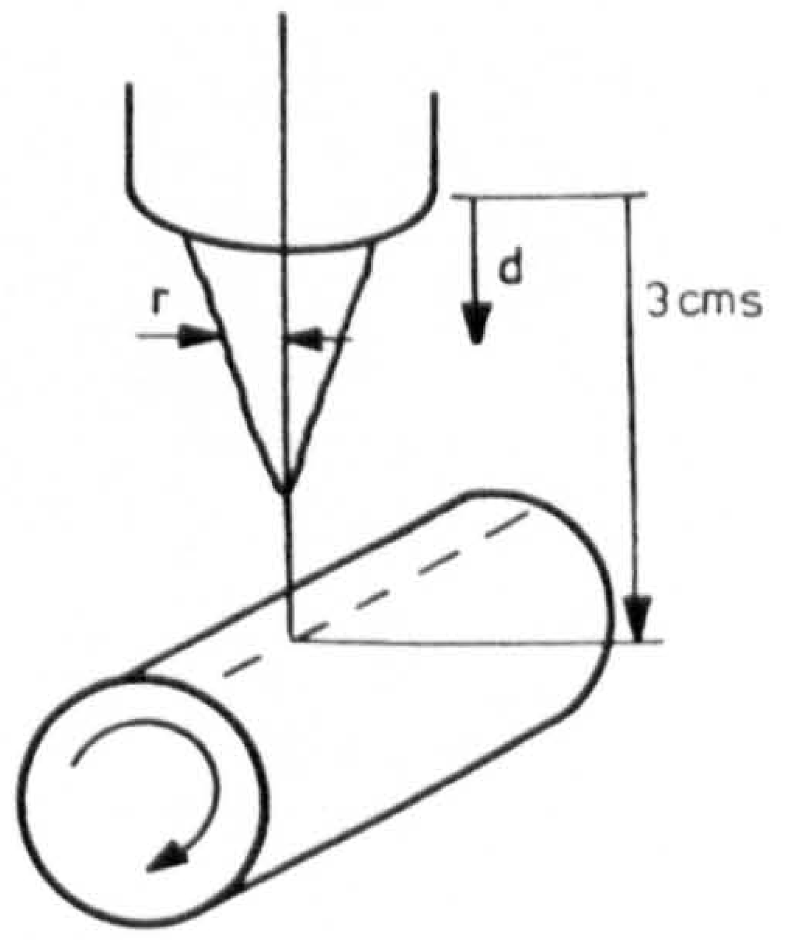

FIG. 7 DIAGRAM OF JET AND SURFACE

and argon flow rates through, the torch. These were measured, and assuming axial symmetry, converted to radial fringe shifts using an Abel transformation (ref.1) having an input of 40 interpolated data points. To enable the inverted fringe shifts to be converted to radial temperatures, measurements were made of ambient air temperatures and humidity. The relationship

$$(n-1)_{15^\circ C} = 27.97\ 10^{-5} + \frac{1.56\ 10^{-14}}{\lambda\,(\mathrm{cms})}$$

for the refractivity of argon (ref.4) was adequate for the present project and the Saha equation to evaluate species densities and electron contribution was not invoked in this series of experiments.

Some radial temperature profiles (calculated from measurements of Fig.4) are shown in Fig.5. Axial temperatures - over a range of low power inputs - from such radial profiles are within bounds shown in Fig.6 - which contain the scatter due to 5% errors in estimates of ambient room temperature, relative humidity and geometrical measurements. These compare with thermocouple measurements in cooler regions of the jet near to the surface of impingement.

The flattening of the radial temperature profiles (Fig.5) adjacent to the cool surface is expected from preliminary solutions to the conservation laws for an argon (in argon) impinging jet but the drop in axial temperature with increasing power (Fig.6) was not predicted. Measurements of nitrogen, oxygen and argon concentration profiles have been made (ref.6), using a mass spectrometer, in the radial wall jet region of an argon plasma jet in air. These indicate the importance of incorporating diffusion coefficients into the fluid flow equations to estimate entrainment rates which may give rise to this anomalous phenomena.

CONCLUSION

The technique is an acceptable method of plasma jet temperature measurement in regions of axial symmetry at temperatures less than 5000 K and the results are consistent with thermocouple measurements. Further work is proposed:

1. to use the present method at higher flow rates and power inputs to compare with available data using spectroscopic techniques, and

2. to develop holographic techniques (ref.2) for the analysis of asymmetric systems at higher temperatures in turbulent flow regions where, with the use of frequency doubling facilities, the validity of L.T.E. can be tested.

ACKNOWLEDGEMENTS

Acknowledgement is made to the British Oxygen Co.Ltd. for the provision of a power supply, the British Rail for the provision of the plasma torch and to Mr. J. Sturrock who executed preliminary experiments with the interferometer.

REFERENCES

1. K.J. Harker, Journal of Applied Physics, V 28 . November 1957.

2. R.W. Maxwell, J.P. Nicholas, Holograms of electric arcs. LUED 77-9, August 1977.

3. R.W. Maxwell, M.J. Ruddy, Volt amp characteristics of a plasma torch. LUED 70-9, April 1970.

4. R.W. Maxwell, M.J. Ruddy, Temperature and noise profiles in argon plasma jet. Gas Discharge Conference, London 1974.

5. B.J. Rye, J.C. Taylor, Physics of hot plasma. Scottish University Summer School, 1968.

6. R. Waters, R.W. Maxwell, Heat and mass transfer in a turbulent radial wall jet. LUED 74-23, December 1974.